Synthetic antiferromagnets for spintronics

By

Shaktiranjan Mohanty

Enrolment No. PHYS11201804009

National Institute of Science Education and Research, Bhubaneswar

A thesis submitted to the

Board of Studies in Physical Sciences

In partial fulfilment of requirements

for the Degree of

DOCTOR OF PHILOSOPHY

of

HOMI BHABHA NATIONAL INSTITUTE

August 2024

Homi Bhabha National Institute[1]

Recommendations of the Viva Voce Committee

As members of the Viva Voce Committee, we certify that we have read the dissertation prepared by **Shaktiranjan Mohanty** entitled **"Synthetic antiferromagnets for spintronics"** and recommend that it may be accepted as fulfilling the thesis requirement for the award of Degree of Doctor of Philosophy.

Chairman - Prof. Bedangadas Mohanty	14/08/2024
Guide / Convener - Prof. Subhankar Bedanta	14/08/2024
Co-guide - Name & Signature with date (if any)	
Examiner - Prof. Saurav Giri	14/08/2024
Member 1- Dr. Kartikeswar Senapati	14/08/2024
Member 2- Dr. Ashis Kumar Nandy	14/08/2024
Member 3- Dr. Debakanta Samal	14/08/24.

Final approval and acceptance of this thesis is contingent upon the candidate's submission of the final copies of the thesis to HBNI.

I/We hereby certify that I/we have read this thesis prepared under my/our direction and recommend that it may be accepted as fulfilling the thesis requirement.

Date: 14/08/2024

Place: Jaipur

Signature
Co-guide (if any)

Signature
Guide Prof. S. Bedanta

[1] This page is to be included only for final submission after successful completion of viva voce.

STATEMENT BY AUTHOR

This dissertation has been submitted in partial fulfilment of requirements for an advanced degree at Homi Bhabha National Institute (HBNI) and is deposited in the library to be made available to borrowers under rules of the HBNI.

Brief quotations from this dissertation are allowable without special permission, provided that accurate acknowledgement of source is made. Requests for permission for extended quotation from or reproduction of this manuscript in whole or in part may be granted by the Competent Authority of HBNI when in his or her judgment the proposed use of the material is in the interests of scholarship. In all other instances, however, permission must be obtained from the author.

Shaktiranjan Mohanty

DECLARATION

I, hereby declare that the investigation presented in the thesis has been carried out by me. The work is original and has not been submitted earlier as a whole or in part for a degree / diploma at this or any other Institution / University.

Shaktiranjan Mohanty

CERTIFICATION ON ACADEMIC INTEGRITY

Undertaking by the Student:

1. I, **Shaktiranjan Mohanty**, HBNI Enrolment No. **PHYS11201804009** hereby undertake that the Thesis, titled "**Synthetic antiferromagnets for spintronics**" is prepared by me and is the original work undertaken by me.
2. I also hereby undertake that this document has been duly checked through a plagiarism detection tool and the document is found to be plagiarism free as per the guidelines of the Institute/UGC.
3. I am aware and undertake that if plagiarism is detected in my thesis at any stage in the future, suitable penalty will be imposed as applicable as per the guidelines of the Institute/UGC.

Shaktiranjan Mohanty
14/08/2024
Signature of the Student with date

Endorsed by the Thesis Supervisor:

I certify that the thesis written by the Researcher is plagiarism free as mentioned above by the student.

S Bedanta
14/08/2024
Signature of the Thesis Supervisor with date

Name: Prof. Subhankar Bedanta

Designation: Professor

Department/Centre: Physical Sciences

Name of the CI/OCC: National Institute of Science Education and Research (NISER), Bhubaneswar

List of Publications arising from the thesis

Journal

1. [#] "*Magnetization Reversal and Domain Structures in Perpendicular Synthetic Antiferromagnets Prepared on Rigid and Flexible Substrates*", **S. Mohanty**, M. Sharma, A. K. Moharana, B. Ojha, E. Pandey, B. B. Singh, and S. Bedanta, The Journal of The Minerals, Metals & Materials Society **(2022)** 74, 2319-2327.

2. [#] "*Observation of topological Hall effect and skyrmions in Pt/Co/Ir/Co/Pt system*" **S. Mohanty,** B. Ojha, M. Sharma and S. Bedanta, Materials Research Express **(2024)**, 11, 046406.

Manuscript in preparation

1. [#] "*Effect of RKKY and dipolar interaction on the nucleation of high-density skyrmions in Pt/Co multilayer system with Ir as spacer layer*", **S. Mohanty** and S. Bedanta *et al.*

2. [#] "*Spin dynamics in an in-plane magnetized CoFeB/Ir/CoFeB system with FM and AFM coupling*", **S. Mohanty** and S. Bedanta *et al.*

3. [#] "*Study of antiferromagnetic interlayer exchange coupling via Ru spacer in a perpendicularly magnetized Pt/Co system*", **S. Mohanty** and S. Bedanta *et al.*

[#]Publications related to the thesis

Others

1. "*Spin pumping and inverse spin Hall effect in CoFeB/IrMn heterostructures*", K. Roy, A. Mishra, P. Gupta, **S. Mohanty**, B. B. Singh, and S. Bedanta, Journal of Physics D: Applied Physics **(2021)**, 54, 42, 425001.

2. "*Spinterface-Induced Modification in Magnetic Properties in $Co_{40}Fe_{40}B_{20}$/Fullerene Bilayers*", P. Sharangi, E. Pandey, **S. Mohanty**, S. Nayak, and S. Bedanta, The Journal of Physical Chemistry C **(2021)**, 125, 45, 25350–25355.

3. "*Magnetoelastic anisotropy in Heusler-type $Mn_{2-\delta}CoGa_{1+\delta}$ films*", T. Kubota, D. Takano, Y. Kota, **S. Mohanty**, K. Ito, M. Matsuki, M. Hayashida, M. Sun, Y. Takeda, Y. Saitoh, S. Bedanta, A. Kimura, and K. Takanashi, Physical Review Materials **(2022)**, 6, 044405**.**

4. "*Magnetic properties in soft(CoFeB)/hard (Co) bilayers deposited under different Ar gas pressure*", 5. S. Nayak, **S. Mohanty**, B. B. Singh, and S. Bedanta, Journal of Physics: Condensed Matter **(2022)**, 34, 385801**.**

5. "*Anisotropy and Domain Structure in Nanoscale-Thick MoS_2/CoFeB Heterostructures: Implications for Transition Metal DichalcogenideBased Thin Films*", V. Thiruvengadam, A. Mishra, **S. Mohanty**, and S. Bedanta, ACS Applied Nano Materials **(2022)**, 5, 8, 10645–10651.

6. "*Device geometry dependent deterministic skyrmion generation from a skyrmionium*", A. Dash, B. Ojha, **S. Mohanty**, A. K. Moharana, and S. Bedanta, Nanotechnology **(2023)** 34, 185001.

7. "*Enhancement of physical properties of $Zn_{1-x}Ni_xO$ pellets synthesized by novel TVA technique for device applications*", N. Kar, S. K. Kamilla, V. R. R. Medicherla, S. Bedanta, **S. Mohanty**, V. Sathe, P. Mallick, Journal of Magnetism and Magnetic Materials **(2023)** 573, 170694**.**

8. "*Study of domain wall dynamics in Pt/Co/Pt ultrathin films*", M. Sharma, B. Ojha, **S. Mohanty**, S Pu¨tter and S. Bedanta, Indian Journal of Physics **(2024)**.

Shaktiranjan Mohanty

Shaktiranjan Mohanty

Dedicated to all my teachers

ACKNOWLEDGEMENTS

I would like to express my deepest gratitude to my supervisor Prof. Subhankar Bedanta for his exceptional guidance, unwavering support, and invaluable mentorship throughout the completion of this thesis work. His expertise in the field of spintronics and magnetism has been instrumental in shaping the direction and quality of this research. I remember the preliminary interaction with him when he assigned me the topic of "synthetic antiferromagnets" as my Ph. D research and the way he explained the topic in a captivating way, sparked my interest to work in this area. His feedback, analysis and discussion on the topic, constructive criticism, approach to research problems and results, excellent presentation skill, made me learn a lot of things and enhanced my ability to do good work in this field. Be it the way of searching for a paper in the internet or publishing an article as a first author, the journey would not be possible without his guidance and invaluable suggestions at the grassroots level which I will always carry forward with me. I am proud to have him as my Ph. D supervisor and at the same time, I am grateful to him for considering me as a student in his group. Apart from this academic journey, there are many non-academic events that made this journey a lot more enjoyable and inspiring. My association with him during the last few years was remarkable which I will cherish forever. I pray before lord Jagannath for his good health and happiness forever.

I also extend my heartfelt appreciation to the chairman of my doctoral committee (DC) members, Prof. Bedangadas Mohanty, and other DC members, Dr. Kartikeswar Senapati, Dr. Ashis Kumar Nandy and Dr. Debakanta Samal, for their invaluable feedback, timely evaluation and insightful comments to improve my research work. I am grateful for their time and effort to evaluate my work.

I would like to thank all my lab members who greatly contributed to my research career at LNMM. Along with other lab members, Dr. Brindaban Ojha and Dr. Esita Pandey have helped me a lot in terms of experiments as well as concepts related to my research topic and motivated me during my initial days and throughout my tenure here, for which I am grateful. I also thank Ms. Bhuvneswari Sharma, Ms. Swayang Priya Mahanta and Ms. Rupali Priyadarsini Chhatoi for their help during experimental measurements and several lab activities whenever I needed. I really appreciate the efforts and help of Dr. Anupama Swain and Mr. Kshitij Singh Rathore in studying the spin dynamics in synthetic antiferromagnets. I thank Mr. Abhisek Mishra for having a lot of insightful discussions in magnetism as well as regarding our research and for his cooperation in smoothly conducting various events related to lab. I also thank Dr. Mitali Swain, Dr. Antarjami Sahoo for their valuable suggestions related to my research topics. I also

thank my younger colleagues Mr. Subhransu Sekhar Sahoo and Mr. Soubhagya Dash for their help and cooperation during various lab activities.

Further, I would also like to thank my former lab members and collaborators Dr. Thiruvengadam Vijayabaskaran, Dr. Sagarika Nayak, Dr. Purbasha Sharangi, Dr. Braj Bhusan Singh, Dr. Minaxi Sharma, Dr. Koustuv Roy and Dr. Pushpendra Gupta, Ms. Mona Bhukta, Mr. Ashish Moharana for their valuable contribution in experiments, scientific discussions for carrying out my research work, help in learning scientific equipment, as well as getting me involved in their work. Also, I thank Dr. Sougata Mallick, Dr. Srijani Mallik, Dr. Palash Kumar Manna, Dr. Bibhuti Bhushan Jena, Mr. Mohammed Azharudheen N for their immense help in pursuing my research work. I also thank Dr. Ashutosh Rath from IMMT, Bhubaneswar for his help in TEM measurements.

I would also like to thank Subhashree, Utkalika, Bidyadhar, Dushmanta, Soumya, Rakesh and a few other friends at NISER for their support in many aspects and many unforgettable memories we shared. I also express my gratitude to my M.Sc friend Subhasmita for her encouragement all the way through and Sangram Bhai for his brotherly support throughout.

I am grateful and fortunate enough for the unconditional support I have from my wife Swati who is always there for me in every aspect of my life. We cherish this achievement together with our newborn baby Sambhav Mohanty. Also, I thank the almighty for blessing me with a supportive brother Mr. Kirtiranjan Mohanty and my caring parents and parents-in-law. I am indebted to my uncle late Satchidananda Mohanty and his family for their support and guidance during my early years that laid the foundations for my academic journey. I am also grateful to my other family members, friends and relatives for their unwavering help and support during my ups and downs.

I am much obliged to my teacher Mr. R. Nageswar Rao for his impactful guidance in clearing the national level exams to get into the Ph. D programme and my M. Sc teacher Prof. Sukanta Kumar Tripathy for his help, motivation and guidance in pursuing my career in scientific research. I am also grateful to all my teachers who have directly or indirectly contributed to my career and helped me throughout this journey.

I sincerely acknowledge SPS-NISER, and CIS-NISER for providing the experimental facilities for carrying out the research work. I thank DAE, Govt. of India, for providing me the fellowship during my Ph. D. I also thank the Indo-French collaborative project (supported by CEFIPRA), DST-Nanomission, DST-SERB for research funding to carry the experimental work presented in my thesis.

Finally, I offer my deepest reverence to Lord Jagannath for everything.

CONTENTS

Summary

Synthetic antiferromagnet (SAF) is a unique class of magnetic structure engineered to exhibit antiferromagnetic (AFM) coupling between adjacent magnetic layers through non-magnetic spacer. In the case of a metallic spacer, the interaction between the two FM layers happens through the spin-polarized conduction electrons present in the NM spacer layer. The interlayer exchange coupling (IEC) here is of an oscillatory decaying nature, which can be described through the Ruderman–Kittel–Kasuya–Yosida (RKKY) interaction. These systems show properties such as high thermal stability, low susceptibility to external magnetic fields, easy characterization through conventional techniques used for FMs, etc., which make them suitable for applications in magnetic sensors, magnetic tunnel junctions (MTJ), and other spintronic devices. Apart from this, there are other aspects for which SAFs are in focus nowadays for spintronic research. One such aspect is it can host chiral magnetic textures like skyrmions. While driving in a track of a single ferromagnetic layer, these skyrmions move towards the edge of the track due to topological Magnus force, known as the skyrmion Hall effect (SkHE). This problem can be addressed by driving the skyrmions in a track of SAF where the opposite topological Magnus force experienced by the skyrmions of both the FM layers will be cancelled and the skyrmions will move in a straight-line path along the direction of the current flow thereby minimising the skyrmion Hall effect. Another aspect of SAF is that it can be a good material system to host magnon-magnon coupling among the AFM-coupled FM layers through antiferromagnetic interlayer exchange interaction. Magnons in spintronics hold the unique advantage of low energy consumption, non-volatility, high-speed operation, etc. Taking advantage of the coupling phenomena in these SAF systems, we have broadly explored the two aspects of it in our work. One aspect is, that we have studied the magnetization reversal, domain structures, and skyrmions in perpendicular magnetic anisotropic (PMA) SAF system. The other one is, that we have studied the spin dynamics in such SAF systems with in-plane magnetization

easy axis. Further, we have explored the possibility of having magnon-magnon coupling in this in-plane magnetized SAF system.

The results are summarized into five sections depending on the spacer layer used as well as the purpose of studying the particular system with variation of IEC through the spacer layer. We have prepared SAF samples with PMA by considering Ru as a spacer layer between the two Co layers. Samples with lower Co thickness i.e. 0.8 nm shows a larger antiferromagnetic coupling plateau than the samples with Co thickness 1.0 nm. Further, by changing the spacer layer to Ir with the Co being 0.8 nm, we have observed three different types of magnetization reversal. With Ir 1.0 nm, the coupling becomes FM whereas, with Ir 1.5 nm, the coupling becomes AFM. By changing the Ir thickness to 2.0 nm, it shows a canted magnetization reversal. The domain images are smaller in AFM-coupled samples as compared to the FM-coupled samples. Further, the presence of chiral spin textures in the samples with Ir thickness 2.0 nm has been confirmed by the topological Hall effect (THE) measurement and Nucleation of skyrmions has been observed by performing MFM measurements on these samples. Further, we have considered the sample structure as Si/SiO2/Ta(3)/Pt(2.5)/[Pt(1)/Co(t_{Co})]$_3$/Ir(1.3)/[Co(t_{Co})/Pt(1)]$_2$/Pt(2.5). The Simultaneous contribution of dipolar coupling and RKKY interaction in Pt/Co multilayer with Ir spacer gives rise to the nucleation of isolated and high-density skyrmions in these systems. The skyrmion size and density increase with the increase in Co thickness in the multilayers. We have also stabilized in-plane SAF with CoFeB as FM and Ir as the spacer layer and explored the possibility of magnon-magnon coupling in this system. However, we could not observe any avoided crossing area between the acoustic and optical mode of magnons extracted from the FMR data which indicates the absence of magnon-magnon coupling in our system.

List of Figures

1.10: Skyrmions observed in the system of Ir/Fe/Co/Pt multilayers at 5K. The plot (a) in the middle shows the topological Hall effect (THE) signal arising due to the presence of skyrmions. This image is adapted with permission from the paper M. Rjau *et. al.,* Nat. Commun. 10, 696 (2019). Copyright 2019, Springer Nature Limited.

1.11: Skyrmions observed in the system of Ir/Fe/Co/Pt multilayers at 5K. The plot (a) in the middle shows the topological Hall effect (THE) signal arising due to the presence of skyrmions. This image is adapted from the paper M. Rjau *et. al.,* Nat. Commun. 10, 696 (2019) [69].

1.12: Illustration of the efficient electrical manipulation of magnetic skyrmions via spin orbit torque (SOT) as a result of the spin Hall effect in the heavy metal layer. This figure is adapted from W. Jiang et. al., physics reports, 704, 1-49 (2017). Copyright 2017, Elsevier.

1.13: (a) Illustration of skyrmion Hall effect during the motion of skyrmion by the application of electrical current, (b) reduction of skyrmion Hall effect by using an SAF track. This image is adapted with permission from T. Dohi et. al., Nat. Commun. 10, 5153(2019). Copyright 2019, Springer Nature Limited.

1.14: Precision of magnetization around the effective magnetic field (a) in the absence and (b) presence of damping in the system, respectively.

1.15: Representation of spin waves due to the collective excitation of precessing spins with a certain amplitude and wavelength. The figure is taken with permission from S. K. Kim *et. al.,* J. Phys. D: Appl. Phys. 43, 264004 (2010). Copyright 2010, IOP publishing.

2.1: Schematic showing the thin film deposition inside a vacuum chamber by sputtering process. A few major components of a sputtering deposition system has also been shown.

2.2: Multi deposition system manufactured by MANTIS Deposition Ltd., UK available in our lab at SPS, NISER.

2.3: (a) Schematic representation of X-ray diffraction from crystallographic planes with interplanar spacing *d*, (b) multipurpose SmartLab X-ray diffractometer by Rigaku available at SPS,

NISER. The inset shows the image of incident optics, receiving optics and the sample stage mounted inside the diffractometer.

2.4: (a) A typical XRR spectrum of a thin film sample. The reflected beam's intensity has been plotted as a function of 2θ (b) schematic representation of the incident (k_i), reflected (k_r) and transmitted (k_t) wave vectors in specular reflection geometry.

2.5: (a) Picture of the JEOL JEM-F200 TEM available at CIS, NISER, (b) Schematics of various major components of a TEM. This schematic is taken with permission from B. J. Inkson, Materials Characterization Using Nondestructive Evaluation (NDE) Methods 17–43. Copyright 2016, Elsevier.

2.6: Schematic representation of various process to prepare a cross-sectional TEM sample for observing the microstructures in TEM.

2.7: (a) Schematic representation of interaction of polarized light with a magnetized sample in longitudional configuration. The Lorentz motion ($\boldsymbol{v_{LOR}}$) of the electrons arising from the interaction of the magnetization of the sample and the electric field of the incident light gives rise to the Kerr amplitude ($\boldsymbol{K}$), (b) shows the orientation of the analyser and polarizer with respect to the Kerr amplitude ($\boldsymbol{K}$) and the normally reflected amplitude ($\boldsymbol{N}$). The schematics are taken with permission from the book Handbook of Magnetism and Advanced Magnetic Materials, (Copyright 2007, John Wiley & Sons, Ltd.).

2.8: Different configurations of the MOKE geometry, (a) L-MOKE, (b) T-MOKE, (c) P-MOKE depending on the direction of the magnetization and the plane of incidence.

2.9: (a) MOKE based microscopy available in our lab at NISER, (b) Schematic representation of the MOKE-based microscopy equipment used to produce the domain image.

2.10: (a) A schematic of the detection coil. The plot indicates the voltage vs sample position during the centering process, (b) MPMS3 SQUID-VSM available in our lab at LNMM, NISER.

2.11: Schematic showing the principle of MFM measurement.

4.7: Hysteresis loops and domain images of the SAF samples S-2-2.0-1 and S-1-2.0-1, measured via MOKE microscopy.

5.1: (a) Schematic of sample structure where n is 1 and 2 for samples Ir-1-1 and Ir-2-1, respectively, (b) XRR fitting of the sample Ir-1-1 performed by GenX.

5.2: Out-of-plane magnetic hysteresis loops of sample (a) Ir-1-1 and (b) Ir-2-1 measured by SQUID-VSM.

5.3: (a)-(d) are the MFM images of the sample Ir-1-1 at different external applied field of 0 mT, 10 mT, 12 mT and 14 mT, respectively. (e)-(h) are the MFM images of the sample Ir-2-1 at applied field 0 mT, 10 mT, 15 mT and 20 mT, respectively. The scale bar of 1 μm is shown (a) and (e).

5.4: (a) Schematic of the measurement geometry for magneto transport measurement of the sample Ir-1-1 in the Van der Pauw geometry. (b) Saturation part of the resistivity measurement data (blue circles). The red line is the linear fit to this data.

5.5: Topological Hall effect (THE) measurement of the sample Ir-1-1. (a) Total resistivity of the sample after removing the ordinary Hall effect component (blue circles) and the AHE fitting to the total Hall resistivity (red line), (b) ρ_{THE} extracted from the resistivity vs magnetic field measurement data after subtracting the OHE and AHE part.

6.1: (a) Schematic of the sample structure for sample S1 and S2, (b) Cross-sectional TEM imaging for the sample S1.

6.2: Magnetization reversal at room temperature for the sample (a) R1-FM and (b) R2-SAF. The measurement has been performed in the presence of an out-of-plane applied magnetic field.

6.3: Out-of-plane hysteresis loop for the sample (a) S1 and (b) S2, measured by SQUID-VSM.

6.4: Hard axis hysteresis loop measured in presence of an in-plane magnetic field for the samples (a) R2-SAF, (b) S1 and (c) S2. The red line in each plot starting from the y-axis and parallel to the x-axis, indicates the saturation magnetization (M_S) of the samples.

6.5: MFM images of the sample S1 at different out-of-plane applied magnetic field. The field values have been mentioned in the inset of each image.

6.6: MFM images of the sample S2 at different out-of-plane applied magnetic field. The field values have been mentioned in the inset of each image.

6.7: Scaling of the contribution from AHE and THE (blue circle) with the AHE (red line) for (a) S1 and (b) S2. (c) and (d) represents the subtracted topological Hall resistivity for the sample S1 and S2, respectively.

6.8: The average skyrmion size analysis for the skyrmions observed in the sample (a) S1 and (b) S2. The red line in the both the plots depicts the lognormal fitting to the measured data to calculate the average skyrmion size.

7.1: (a) Schematic of sample structure, (b) Cross-sectional TEM image of sample M1.

7.2: Kerr microscopy hysteresis loops at angle, 0, 30, 60 and 90 degrees for the samples (a) R1, (b) M1, and (c) M2.

7.3: Magnetic domain images captured by Kerr microscopy for the samples R1, M1 and M2. (a1) and (a4) are the domain images at +ve and –ve saturation, respectively, for the sample R1. (a2) and (a3) shows the domains during the reversal. Similarly, (b1)-(b4) are the domain images for M1 and (c1)-(c4) are the domain images for M2.

7.4: Frequency dependent FMR spectra with a varying in-plane magnetic field for the samples (a) R1, (b) M1, and (c) M2. (d) The gyromagnetic ratio (γ) is evaluated by fitting the frequency (f) vs H_{res} plot using the Kittel equation. (e) The damping value (α) is evaluated by the linear fit of ΔH vs f for all the samples.

7.5: Plot of f_{res} vs H for both the AM and OM branches for the samples (a) M1 and (b) M2. (c) FMR curves for a few selected field values in the frequency sweep mode for sample M2.

List of Tables

List of Abbreviations

AFM	Antiferromagnet
AHE	Anomalous Hall effect
AM	Acoustic mode
CPW	Coplanar waveguide
CVD	Chemical vapour deposition
DC	Direct current
DMI	Dzyaloshinskii-Moriya interaction
DW	Domain wall
EA	Easy axis
FM	Ferromagnet
FMR	Ferromagnetic resonance
HA	Hard axis
HDD	Hard disc drives
HM	Heavy metal
IEC	Interlayer exchange coupling
LLG	Landau-Lifshitz-Gilbert
MFM	Magnetic force microscopy
MOKE	Magneto-optic Kerr effect
MRAM	Magnetic random access memory
MTJ	Magnetic tunnel junction
OHE	Ordinary Hall effect
OM	Optical mode
PMA	Perpendicular magnetic anisotropy
PVD	Physical vapour deposition
QCM	Quartz crystal microbalance
RF	Radio frequency
RKKY	Ruderman–Kittel–Kasuya–Yosida
SAED	Selected area electron diffraction
SAF	Synthetic antiferromagnet
SHE	Spin Hall effect
SkHE	Skyrmion Hall effect

SOC	Spin-orbit coupling
SOT	Spin-orbit torque
SQUID	Superconducting Quantum Interference Device
SRT	Spin reorientation transition
TEM	Transmission electron microscopy
THE	Topological Hall effect
TMP	Turbo molecular pump
UHV	Ultra-high vacuum
VSM	Vibrating sample magnetometer
XRD	X-ray diffractometer
XRR	X-ray reflectivity

Chapter 1

Introduction:

In the modern era of information technology, magnetic storage has been a cornerstone of data storage underpinning a myriad of applications ranging from personal computing to cloud infrastructure. The relentless pursuit of higher storage densities, faster access times, and lower energy consumption has driven relentless innovation in magnetic storage technology. Central to this pursuit is the quest for materials and structures capable of harnessing the fundamental properties of magnetism to store and manipulate information efficiently [1].

Magnetic storage devices, such as hard disk drives (HDDs) and magnetic random-access memories (MRAMs), rely on the manipulation of magnetic domains within thin film structures to encode binary information [2,3]. Traditionally, these devices have been based on ferromagnetic materials, where the magnetization of individual domains can be switched by applying an external magnetic field. While ferromagnetic materials have served as the workhorse of magnetic storage technology for decades, they face inherent limitations in terms of stability, scalability, and energy efficiency as the demand for higher storage densities continues to escalate. In this context, synthetic antiferromagnets (SAFs) have emerged as a compelling candidate, offering unprecedented control over magnetic properties and promising breakthroughs in the realm of spintronics. SAFs represent a paradigm shift in magnetic storage technology, offering a novel approach to overcome the limitations of conventional ferromagnetic materials.

1.1 Synthetic antiferromagnets:

SAFs are composed of two ferromagnetic layers coupled antiferromagnetically through non-magnetic spacer layers via interlayer exchange coupling (IEC) [4,5]. The schematics of in-plane and out-of-plane magnetized SAF have been shown in Figure 1.1 (a) and (b),

respectively. The interaction between the magnetic moments of the FM layers occurs through the exchange of spin-polarized electrons across the spacer. The nature of the coupling can be either FM or antiferromagnetic (AFM), depending on the specific materials used and the thickness of the NM layer. FM coupling implies parallel alignment of magnetic moments in the adjacent layers, while AFM coupling implies an antiparallel alignment. This particular configuration, where the spins of the two FM layers are aligned in an antiparallel manner, is known as synthetic antiferromagnet (SAF). SAF is a unique class of magnetic structure engineered to exhibit AFM coupling between adjacent magnetic layers. The IEC here is of oscillatory decaying nature which can be described through the Ruderman–Kittel–Kasuya–Yosida (RKKY) interaction theory [6–8]. Unlike natural antiferromagnets, which occur in certain materials spontaneously, SAFs are artificially created through thin-film deposition techniques. This unique arrangement endows SAFs with a host of advantageous properties, including enhanced thermal stability, reduced susceptibility to external perturbations, and tunable magnetic switching behaviour. Moreover, the interlayer exchange coupling in SAFs enables precise control over the magnetic state of individual layers, paving the way for advanced functionalities and novel device architectures. By leveraging the unique properties of SAFs, researchers aim to develop magnetic storage devices with unprecedented performance, reliability, and energy efficiency. For instance, SAF-based MRAMs hold the promise of non-volatile memory with fast write/read speeds, low power consumption, and robust operation [9,10]. Furthermore, the tunability of SAF allows for the exploration of novel storage concepts such as racetrack memory, where magnetic information is propagated along nanowires using spin currents. In addition to their relevance in magnetic storage technology, SAFs play a crucial role in advancing the broader field of spintronics. The ability to manipulate spin degrees of freedom in SAFs opens up new avenues for spin-based logic, computing, and

communication, offering potential solutions to the challenges posed by conventional semiconductor-based technologies.

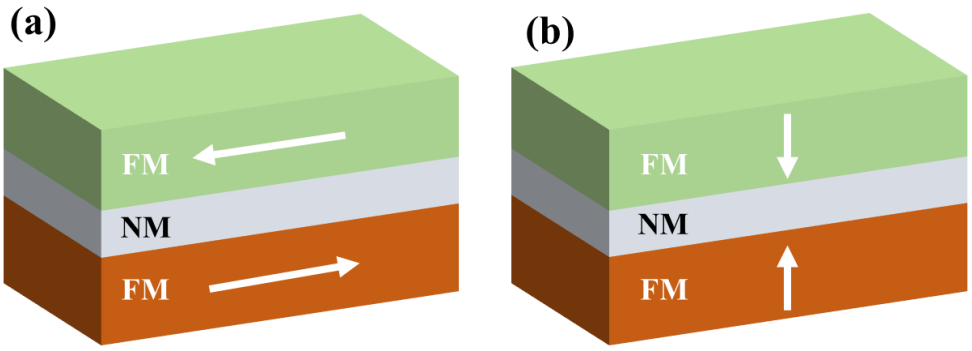

Figure 1.1: Schematics of the synthetic antiferromagnetic (SAF) structure with (a) in-plane and (b) out-of-plane configuration.

Magnetic tunnel junctions (MTJs) play a pivotal role for enhancing the data storage capacity. SAFs are the key part of these MTJ devices for better data retaining and thermal stability due to the absence of stray field [11–13]. Apart from this, there are lot more aspects for which SAFs are in focus now-a-days for spintronic research. One such aspect is that it can host chiral magnetic textures viz. skyrmions which are basically topologically protected, vortex like chiral spin textures [14]. Skyrmions possess advantage of high stability, require low threshold current density and it's nano scale size making it way better for data storage technology [15,16]. It is also less susceptible to the system's pinning. Skyrmions are therefore thought to be highly attractive options for improving the density of next-generation data storage. Similar to domain wall, skyrmion racetrack memory can also be implemented [17–20]. In addition to storage, skyrmions can be potential candidate in achieving neuromorphic computing, logic devices, and transistor-like devices [21–25]. However, while driven in a track of single ferromagnetic layer, instead of moving in a straight line in the applied current direction, it moves towards the edge of the track due to topological Magnus force which is known as the skyrmion Hall effect (SkHE) [26,27]. This may lead to the loss of information which is undesired. This problem can be addressed by driving the skyrmion in a track of SAF. Here two skyrmions with opposite

topological number will be nucleated in both the FM layers below and above the spacer layer which are antiferromagnetically coupled. So, without being affected by the Magnus force, the skyrmions move in a straight-line path along the direction of current flow which can minimize the skyrmion Hall effect [28].

Another aspect of SAF is that it can be a good material system to host magnon-magnon coupling among the AFM coupled FM layers through antiferromagnetic interlayer exchange interaction between them. Magnons in spintronics hold the unique advantage of low energy consumption, non-volatility, high speed operation etc [29,30]. Taking advantage of the coupling phenomena in these systems, we have broadly explored the two aspects of SAF in our work. On the one hand we have studied the magnetization reversal, domain structures and skyrmions in perpendicular magnetic anisotropic (PMA) SAF system. On the other hand we have studied the spin dynamics in such SAF system with in-plane magnetic anisotropy. Further, we have explored the possibility of having magnon-magnon coupling in this in-plane magnetized SAF system.

In light of these considerations, this Ph.D. thesis has been organised into eight chapters. The first chapter discusses few basic concepts required to understand the thesis work. All the experimental techniques used for the research work have been discussed in the second chapter. In the third chapter the study about the stabilization of synthetic antiferromagnetic structure in Pt/Co PMA system with Ru spacer has been shown. By varying the Ru thickness between two Co layers, the variation of coupling strength has been studied. A larger antiferromagnetic coupling plateau has been observed in the series with less Co thickness. The fourth chapter shows the magnetization reversal and domain structures in perpendicularly magnetized Pt/Co system with Ir as a spacer layer. Here, by changing the Ir spacer thickness as well as number of stackings of Pt/Co below and above the spacer, three types of magnetization reversal such as ferromagnetic, antiferromagnetic and canted state of magnetization have been observed. The

fifth chapter discusses the observation of topological Hall effect (THE) signal and skyrmions in Pt/Co/Ir/Co/Pt system with canted magnetization reversal. The presence of chiral spin textures in these samples has been confirmed by the THE measurement and nucleation of skyrmions has been observed further by measuring the samples via magnetic force microscopy (MFM). In the sixth chapter, the simultaneous effect of RKKY and dipolar interaction in Pt/Co multilayer system with Ir as spacer layer has been studied. The Ir spacer thickness is optimized to provide the RKKY interaction between the Co layers. The nucleation of isolated and high density skyrmions have been observed in these systems. The skyrmion size and density are found to increase with the increase in Co thickness in the multilayers. In the seventh chapter, the Spin dynamics in an in-plane magnetized CoFeB/Ir/CoFeB system with FM and AFM coupling has been studied via ferromagnetic resonance spectroscopy. The possible presence of magnon-magnon coupling in these systems has been explored. However, no avoided crossing area in the FMR data has been observed which indicates the absence of magnon-magnon coupling in our system. In the last chapter, we have concluded our thesis work with possible future prospects in this area of research.

1.2 Spin-orbit interaction:

The spin-orbit interaction is a fundamental quantum mechanical phenomenon that arises from the coupling between the spin of an elementary particle, such as an electron, and its orbital motion around a central potential, typically in the presence of an electromagnetic field. This interaction plays a crucial role in various physical phenomena across different fields of science, including condensed matter physics, atomic physics, and quantum computing. In the context of condensed matter physics, the spin-orbit interaction profoundly influences the electronic properties of materials, leading to phenomena such as spin-orbit coupling (SOC), spin Hall effect, etc. The spin-orbit coupling arises from the relativistic correction to the electron's kinetic energy due to its motion in the electric field generated by the atomic nuclei. This plays a crucial

role in determining the magnetic properties of thin films, such as spin relaxation, modifying the anisotropy of the system, especially in achieving perpendicular magnetic anisotropy (PMA), etc. PMA refers to the preference of magnetic moments to align perpendicular to the plane of the film [31] rather than in the plane. This property is essential for various technological applications, including magnetic recording and spintronic devices, as it allows for high-density data storage and efficient manipulation of magnetic states. In thin film systems, especially those composed of heavy metal layers (e.g., Pt, Ta, W), the strong SOI induces an effective magnetic field that interacts with the magnetic moments of adjacent layers. This interaction can lead to the stabilization of perpendicular magnetization orientations, thereby promoting PMA in thin films. The expression for the SOI energy can be written as [32],

$$\langle H_{so} \rangle = \frac{Z^4 e^2 \hbar^2 \langle \boldsymbol{S}.\boldsymbol{L} \rangle}{4\pi\epsilon_0 a_0^3 n^3 l \left(l + \frac{1}{2}\right)(l+1)} \quad \ldots\ldots (1.1)$$

Where, n and l are the principal and orbital quantum number of electrons. Z is the atomic number of the element. $\boldsymbol{S}$ is the spin angular momentum and $\boldsymbol{L}$ is the orbital angular momentum. As the SO coupling energy is proportional to the Z^4, the heavy metal with higher atomic number can have high SO coupling. The least energy state is favourable when $\boldsymbol{S}$ and $\boldsymbol{L}$ are parallel, while energy is maximum when $\boldsymbol{S}$ is perpendicular to $\boldsymbol{L}$.

1.3 Magnetic anisotropy:

Anisotropy refers to the property of a material exhibiting different physical characteristics or properties when measured along different axes. In other words, anisotropy indicates a directional dependence of the properties of a material. Magnetic materials can exhibit different magnetic properties along different directions. For instance, ferromagnetic materials may have preferred directions of magnetization alignment, known as easy axes, due to factors like shape, crystal structure, or external influences. This property plays a crucial role in determining the

stability and behavior of magnetic domains, as well as the response of the material to external magnetic fields. This magnetic anisotropy is crucial for various applications in magnetic recording, spintronics, and magnetic sensors. Based on the origin and underlying physical mechanism, magnetic anisotropy can be further classified into few sub categories i.e., (i) magnetocrystalline anisotropy or crystal anisotropy, (ii) shape anisotropy, (iii) magnetoelastic/stress anisotropy, (iv) surface/interface anisotropy.

1.3.1 Magnetocrystalline anisotropy:

Magnetocrystalline anisotropy is a type of magnetic anisotropy that arises from the dependence of a material's magnetic energy on the orientation of its magnetic moments with respect to the crystallographic axes of its underlying lattice structure. In other words, magnetocrystalline anisotropy describes the directional dependence of a material's magnetization due to its crystal structure and symmetry. The origin of magnetocrystalline anisotropy can be attributed to several factors such as, spin-orbit coupling, crystal structure, exchange interaction, etc. Due to the coupling between the spin and the orbital motion of the electron, in an attempt to reorient the spin of an electron by applying an external magnetic field, the orbit of that electron also tries to be reoriented. However, as the orbit is strongly coupled to the lattice, this twisting of the spin axis is resisted. Hence, in a way, it can be stated that the anisotropy energy is the energy required to rotate the spins away from easy axis. Typically, the exchange energy is greater than the magnetocrystalline anisotropy (MCE) energy strength. However, because exchange energy tries to align the moments parallelly or anti-parallelly regardless of their directions, the direction of magnetization i.e., $m=\boldsymbol{M}/|\boldsymbol{M}|$, is completely dependent on anisotropy energy. In spherical polar co-ordinate, m can be represented with the direction cosines α_i as, $m=(\alpha_1, \alpha_2, \alpha_3)$, where, $\alpha_1=\sin\theta\cos\phi$, $\alpha_2=\sin\theta\sin\phi$, $\alpha_3=\cos\theta$ fulfilling the normalization condition $\alpha_1^2 + \alpha_2^2 + \alpha_3^2 = 1$. Here, θ and ϕ are the angles which the direction of magnetization makes with

the z-axis and the azimuthal angle, respectively. The magnetocrystalline anisotropy energy per unit volume can be expressed as,

$$E_{MCA} = E_0 + \Sigma_i c_i \alpha_i + \Sigma_{ij} c_{ij} \alpha_i \alpha_j + \Sigma_{ijk} c_{ijk} \alpha_i \alpha_j \alpha_k + \Sigma_{ijkl} c_{ijkl} \alpha_i \alpha_j \alpha_k \alpha_l + \Gamma(\alpha^5) \quad \ldots\ldots. (1.2)$$

Here, c is the coefficient of anisotropy. The higher order terms $\Gamma(\alpha^5)$ being very small, are neglected. Hence, in further calculations, considering the energies of oppositely magnetized states having equal amplitude i.e., $E(\alpha_i) = E(-\alpha_i)$, there by cancelling the odd terms, the equation (1.2) can be written as [33,34],

$$E_{MCA} = E_0 + \Sigma_{ij} c_{ij} \alpha_i \alpha_j + \Sigma_{ijkl} c_{ijkl} \alpha_i \alpha_j \alpha_k \alpha_l \quad \ldots\ldots. (1.3)$$

Depending on the alignment of easy axis in different directions in a magnetic material, the magneto crystalline anisotropy can be further divided into various types such as, uniaxial anisotropy, cubic anisotropy, hexagonal anisotropy, etc.

Uniaxial anisotropy arises when a material exhibits a single preferred direction of magnetization alignment. Here, the easy axis of the system aligns itself in a particular direction with an interval of 180^0. Cubic anisotropy arises when a material exhibits two easy axes of magnetization mutually perpendicular to each other over 180^0 interval due to the cubic symmetry of its crystal structure. In cubic materials, there are usually three orthogonal crystallographic axes, and the energy associated with magnetization alignment may vary depending on the alignment along these axes.

1.3.2 Shape anisotropy:

Shape anisotropy, also known as magnetostatic or demagnetization anisotropy, arises from the geometric shape of a magnetic material. It is a type of magnetic anisotropy that occurs in materials with non-uniform shapes or geometries. Shape anisotropy influences the magnetic

behaviour of a material by favouring a particular direction of magnetization alignment, typically along the longest axis or axis of symmetry of the shape. The origin of shape anisotropy can be understood through the minimization of the magnetostatic energy of the material i.e., aligning the magnetic moments in a direction that minimizes the demagnetization energy associated with the material's geometry. When a magnetic material is magnetized, it creates a magnetic field around it. In non-uniformly shaped materials, the distribution of this magnetic field is affected by the shape of the material, resulting in varying energy states for different orientations of magnetization. The stray field energy or the demagnetization energy of a magnetic material can be written as [33],

$$E_{demag} = \frac{1}{2}\int \mu_0 \boldsymbol{M}.\boldsymbol{H}_{demag} dV \qquad \ldots\ldots. (1.4)$$

For an ellipsoid, the demagnetizing field ($\boldsymbol{H}_{demag}$) is expressed as $\boldsymbol{H}_{demag} = N.\boldsymbol{M}$. Here, N, the demagnetizing factor, is a diagonal tensor with trace (N) = 1 and represented as,

$$N = \begin{pmatrix} N_x & 0 & 0 \\ 0 & N_y & 0 \\ 0 & 0 & N_z \end{pmatrix} \qquad \ldots\ldots. (1.5)$$

With this, the equation (1.4) becomes,

$$E_{demag} = \frac{1}{2} V \mu_0 \left(N_x m_x^2 + N_y m_y^2 + N_z m_z^2\right) \qquad \ldots\ldots. (1.6)$$

Along the equatorial axis of an ellipsoid, N_x=N_y. So,

$$E_{demag} = \frac{1}{2} V \mu_0 M_s^2 (N_x sin^2\theta + N_z cos^2\theta) = \frac{1}{2} V \mu_0 M_s^2 cos^2\theta (N_z - N_x) \qquad \ldots\ldots. (1.7)$$

The least stray field energy occurs when θ = 90°, suggesting that the stray field energy is in favor of the magnetization being orientated in the plane of the sample. In order to further limit the stray field, a specimen is separated into distinct spontaneous magnetization known as domains.

1.3.3 Magnetoelastic or stress anisotropy:

Magnetoelastic anisotropy, also known as stress-induced anisotropy or stress anisotropy, refers to the dependence of a material's magnetic properties on mechanical strain or stress. It arises from the coupling between the magnetic moments and the lattice strain or stress in the material, leading to changes in the energy landscape for magnetization alignment. The origin of magnetoelastic anisotropy can be understood through the interaction between the magnetic moments and the crystal lattice structure of the material. When a magnetic material is subjected to mechanical strain or stress, it affects the spacing between atoms and alters the symmetry of the crystal lattice. This, in turn, modifies the exchange interactions between neighbouring magnetic moments and their alignment. In this context, an important phenomenon known as magnetostriction [34,35], plays a pivotal role in explaining the origin of magnetoelastic anisotropy. Magnetostriction is a phenomenon observed in certain magnetic materials whereby the material undergoes a change in shape or dimensions in response to an applied magnetic field. When a magnetic material is subjected to an external magnetic field, the alignment of the magnetic moments within the material changes. This reorientation of magnetic moments leads to the deformation or strain of the material, resulting in a change in its dimensions.

1.3.4 Surface anisotropy:

Surface anisotropy refers to the phenomenon where the magnetic properties of a material are influenced by the characteristics of its surface. It arises due to the asymmetry or broken symmetry at the material's surface, leading to preferential orientations of magnetic moments near the surface. Surface anisotropy plays a significant role in determining the magnetic behaviour of thin films, nanoparticles, and nanostructures, where the surface-to-volume ratio is high and surface effects dominate the overall magnetic properties. In the case of ultrathin magnetic films, the effective anisotropy can be expressed as [33,36],

$$K_{eff} = K_V + \frac{2K_S}{t} \qquad \ldots\ldots (1.8)$$

Where, K_S is the contribution of surface anisotropy and K_V is the contribution volume anisotropy and t is the thickness of the ferromagnetic layer. The factor 2 is due to the two interfaces of the film breaking the inversion symmetry. The equation (1.8) can further be written in the form of equation of a straight line,

$$K_{eff}.t = K_V.t + 2K_S \qquad \ldots\ldots (1.9)$$

Where the slope and intercept of plot between $K_{eff}.t$ and t determines the K_V and K_S, respectively. At higher thickness, the volume contribution to the anisotropy dominates the surface contribution thus favouring an in-plane magnetization in the system. Conversely, at a

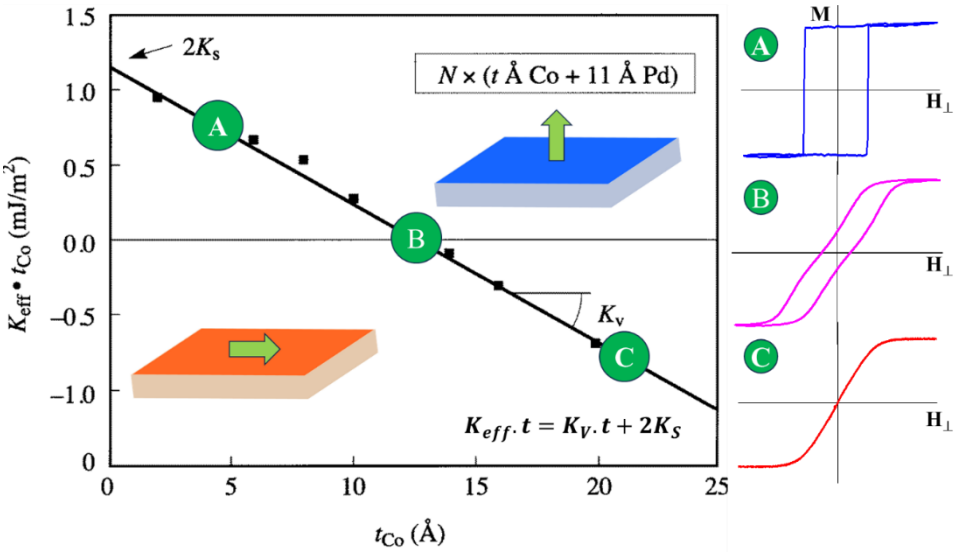

Figure 1.2: Plot of $K_{eff}.t$ vs t (thickness of Co layer) for Co/Pt multilayer sample. (a), (b) and (c) indicates magnetization reversal for the out-of-plane anisotropic, at spin reorientation transition (SRT) and in-plane anisotropic samples. The intercept gives the surface contribution and the slope gives the volume contribution. The concept of this modified figure is taken with permission from the Broeder *et. al.*, JMMM 93, 562-570 (1991) [37]. Copyright 1991, Elsevier.

lower thickness, the surface contribution dominates the volume contribution and the system becomes out-of-plane magnetized. At a critical thickness (t_c) of the FM layer when the surface

and volume contribution are almost equal, spin reorientation transition (SRT) happens. The transition from in-plane to out-of-plane magnetization for Co/Pd multilayer by varying the Co thickness has been shown in Figure 1.2. Next, we discuss about the various types of interactions which may be present in a magnetic system thereby manipulating the magnetic properties.

1.4 Magnetic interactions:

Magnetic interactions refer to the forces and energies involved in the interaction between magnetic moments or magnetic materials. These interactions play a fundamental role in determining the magnetic properties and behaviour of materials, influencing phenomena such as magnetization, magnetic ordering, and domain formation. Many of these interactions, which largely affects the magnetic properties of a system, are discussed below.

1.4.1 Exchange interactions:

The exchange interaction is a fundamental quantum mechanical phenomenon that describes the coupling between the magnetic moments (spins) of electrons in a material. It is responsible for the alignment of spins and plays a crucial role in determining the magnetic properties of materials. The exchange interaction energy depends on the relative orientation of the spins of the interacting electrons. When the spins are parallel, the exchange interaction energy is lower than when the spins are antiparallel. Considering the nearest neighbour atomic spins $\boldsymbol{S_i}$ and $\boldsymbol{S_j}$, the exchange energy for the system is written as [32,33],

$$E_{exch} = -\Sigma_{ij} J_{ij} \boldsymbol{S_i}.\boldsymbol{S_j} \qquad \ldots\ldots. (1.10)$$

Here, J_{ij} is the exchange coupling constant. In ferromagnetic materials, where neighbouring spins are aligned parallel to each other, the exchange interaction leads to a net magnetic moment and the formation of magnetic domains. In this case, J_{ij}>0. In antiferromagnetic materials, J_{ij}<0 where, neighbouring spins are aligned antiparallel. The exchange interaction results in cancellation of magnetic moments, leading to zero net magnetization. The direct

exchange mechanism depends on the overlap of electron wave functions between neighbouring atoms or ions. Hence, the magnetic ordering of all the materials cannot be explained using this. There are some other types of exchange interactions which are discussed below.

1.4.1.1 Double exchange:

Double exchange is a mechanism that describes the interaction between itinerant electrons and localized magnetic moments in certain materials, particularly in transition metal oxides [32]. This mechanism was first proposed to explain the unusual magnetic properties observed in materials like manganites. Itinerant electrons can move between neighboring sites in the crystal lattice. This movement is facilitated by the overlap of electron wavefunctions between adjacent sites. During the process, it aligns its spin with the local magnetic moment at the destination site. This alignment lowers the energy associated with the hopping process, as a consequence, the neighbouring magnetic moments tend to align parallel to each other.

1.4.1.2 Superexchange interaction:

Superexchange interaction is a mechanism of indirect exchange coupling between magnetic moments mediated by intervening non-magnetic atoms or ions [33,34]. This can explain the magnetic interactions in insulating materials where direct exchange interactions between neighboring spins are forbidden due to the presence of non-magnetic ions in between. This interactions often lead to antiferromagnetic ordering in materials, where neighboring spins align antiparallel to each other.

1.4.2 Dzyaloshinskii-Moriya interaction:

The Dzyaloshinskii-Moriya interaction (DMI) was first proposed independently by T. Dzyaloshinskii in 1958 and T. Moriya in 1960 [38,39]. It is a type of antisymmetric exchange interaction that arises in systems lacking inversion symmetry. It The DMI plays a crucial role in stabilizing chiral magnetic structures and can lead to various exotic magnetic phenomena,

such as skyrmions and chiral domain walls. The Dzyaloshinskii-Moriya interaction can be described mathematically by the following Hamiltonian term [40],

$$H_{DMI} = -\Sigma_{ij} \boldsymbol{D_{ij}} . (\boldsymbol{S_i} \times \boldsymbol{S_j}) \quad \ldots\ldots (1.11)$$

Where, $\boldsymbol{D_{ij}}$ is the Dzyaloshinskii-Moriya vector that characterizes the strength and direction of the interaction between spins $\boldsymbol{S_i}$ and $\boldsymbol{S_j}$. The schematic of the DM interaction in an HM/FM system have been shown in Figure 1.3. The DMI term introduces an additional interaction energy that depends on the cross product of neighbouring spins, leading to a coupling between spin directions and the Dzyaloshinskii-Moriya vector. Unlike the conventional exchange interaction, which favours parallel or antiparallel alignment of spins, the DMI prefers a non-collinear arrangement of spins perpendicular to the vector $\boldsymbol{D_{ij}}$.

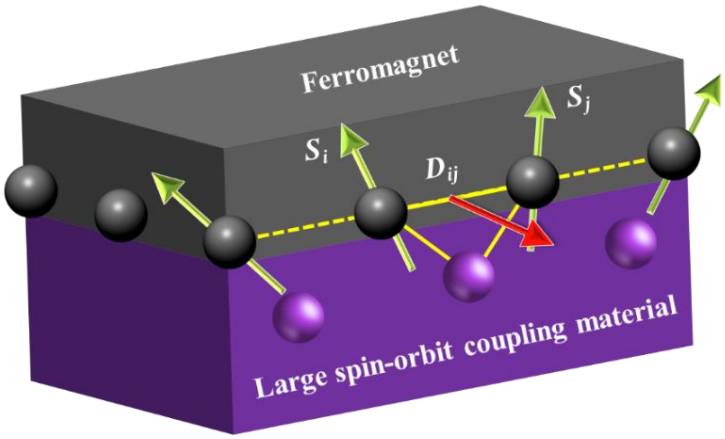

Figure 1.3: Representation of the iDMI vector (D_{ij}) at the heavy metal-ferromagnet interface.

1.4.3 RKKY interaction:

The Ruderman-Kittel-Kasuya-Yosida (RKKY) interaction describes the indirect exchange coupling between magnetic impurities in a non-magnetic host material. It arises from the interaction between the localized magnetic moments of the impurities mediated by the conduction electrons in the host material [6–8]. When a ferromagnetic impurity is present in bulk non-magnetic metals, the nearby sea of conduction electrons becomes spin polarized. Rather than being equal in the region of the impurity, the densities of all the spin down and

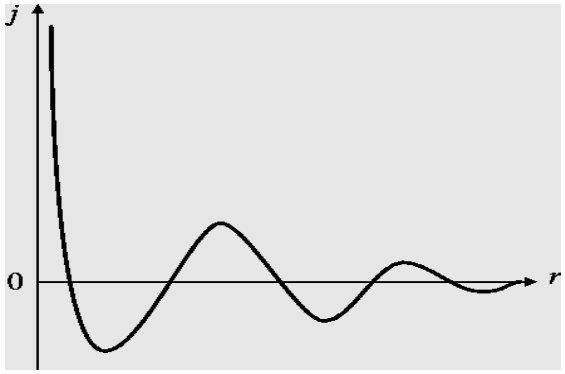

Figure 1.4: Oscillatory decaying variation of RKKY interaction with respect to the distance (r) between two ferromagnetic spins.

spin up electrons become slightly different. The resulting spin polarization attenuates as $1/r^3$, with r being the distance from the impurity, and oscillates with a wave vector of $2k_F$. Here, k_F is the Fermi wave vector. An indirect coupling between the spins of the two impurities results from the presence of a second magnetic impurity located at some distance from the first. The coupling between them can be either ferromagnetic or antiferromagnetic based on their distance from one another. The Hamiltonian describing the interaction between the impurity spins S_i and S_j can be written as,

$$H_{RKKY} = \boldsymbol{J_{ij}\, S_i \,.\, S_j} \qquad \ldots\ldots. (1.12)$$

Where, J_{ij} is the RKKY exchange coupling constant between the impurity spins separated by a distance r. Further, this RKKY exchange coupling constant (J_{ij}) can be expressed as [41],

$$J_{RKKY} = \frac{m^* k_F^4}{\hbar^2} F(2k_F r) \qquad \ldots\ldots. (1.13)$$

Where, m^* is the effective mass and,

$$F(x) = \frac{x\cos x - \sin x}{x^4} \qquad \ldots\ldots. (1.14)$$

This shows the oscillatory decaying nature of RKKY interaction between two magnetic impurities [42]. The schematic of this oscillatory decaying behaviour has been depicted in Figure 1.4. This oscillatory behaviour gives rise to long-range interactions between the

impurity spins and can lead to interesting magnetic phenomena in layered magnetic thin films. As discussed earlier, this RKKY interaction plays a crucial role in explaining the antiferromagnetic alignment between two ferromagnetic layers separated by a spacer layer, known as synthetic antiferromagnets.

1.4.4 Dipolar interaction:

Dipolar interaction in magnetism refers to the magnetic interaction between magnetic moments due to their inherent magnetic fields. It arises from the electrostatic interaction between magnetic dipoles and is a fundamental aspect of magnetic materials. Dipolar interactions can have significant effects on the magnetic properties of materials, influencing phenomena such as domain formation, magnetic ordering, etc. The dipolar interaction energy between two magnetic moments depends on the specific geometry of the system. For a pair of magnetic moments separated by a distance *r*, the dipolar interaction energy E_{dip} can be described by the following formula [32,33]:

$$E_{dip} = \frac{\mu_0}{4\pi}\frac{m_1.m_2 - 3(m_1.r)(m_2.r)}{r^3} \qquad \ldots\ldots (1.15)$$

m_1 and m_2 are the magnetic moments of the two dipoles. The dipolar interaction is long-range and decreases with distance as $1/r^3$, which means it can have significant effects even at relatively large distances compared to the atomic scale. The significance of dipolar interaction lies in its role in determining the magnetic properties and behaviour of materials, including the formation of magnetic domains, the stability of magnetic structures, and the behaviour of magnetic nanoparticles. Understanding and controlling dipolar interactions is essential for various applications in magnetism, including data storage, magnetic recording, and magnetic materials engineering.

1.4.5 Zeeman interaction:

The Zeeman interaction is a fundamental interaction in quantum mechanics and solid-state physics that describes the interaction between a magnetic field and the magnetic moment associated with a quantum mechanical system, such as an electron's spin or the magnetic moment of an atomic nucleus. It is named after the Dutch physicist Pieter Zeeman, who observed the splitting of spectral lines in the presence of a magnetic field. For a magnetic dipole with moment μ, present in an external magnetic field B, the Zeeman interaction energy can be written as [34],

$$E_{Zeeman} = -\mu.B \qquad \ldots\ldots. (1.16)$$

The interaction leads to the splitting of energy levels in the presence of a magnetic field. This splitting occurs because the energy levels depend on the orientation of the electron's spin relative to the magnetic field direction. The energy of the system gets minimized due to the applied magnetic field which always tries to align the moments along its direction.

1.5 Magnetization reversal:

Magnetization reversal refers to the process by which the direction of magnetization in a magnetic material, changes from one orientation to another. This process is fundamental in various magnetic devices and materials, including magnetic memories, sensors, and recording media. The reversal process hinges on the initial arrangement of magnetization within the sample, often referred to as its hysteresis [32–34]. This occurs because the magnetization of ferromagnetic materials does not change linearly with variations in the applied field, leading to the characteristic hysteresis loop. Hysteresis, representing a non-linear, non-equilibrium, and intricate first-order phase transition, arises from this phenomenon, where, upon the application of a sufficiently strong external magnetic field, all spins within the system align themselves in the direction of the applied field. This state is known as the saturation magnetization (M_s). In

this state, the magnetization of the system reaches its maximum value and the applied field in this condition is termed as the saturation field (H_S). From this saturated state, when the applied field is reduced to zero, the system retains a residual magnetization, referred to as the remanent state (M_R). The coercive field (H_c) denotes the reverse magnetic field required to diminish the system's magnetization back to zero. Figure 1.5 displays the locations of M_R, M_S, H_C and H_S for a typical hysteresis loop during the magnetization reversal. Magnetization reversal can occur through different mechanisms, depending on the material and the applied external conditions. There are two primary mechanisms through which magnetization reversal can occur: domain wall motion and coherent rotation.

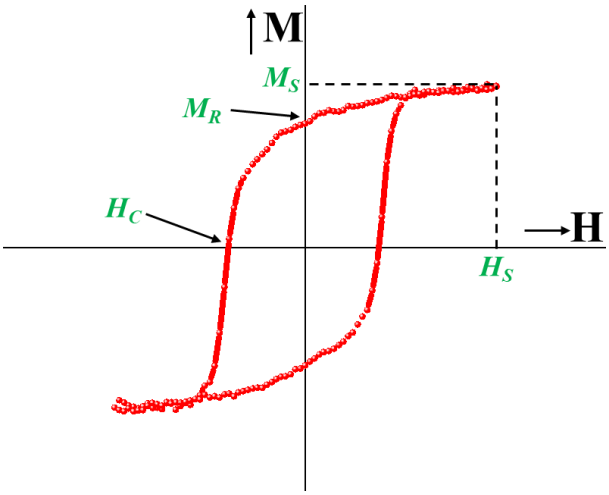

Figure 1.5: A typical magnetic hysteresis loop indicating the points M_R, M_S, H_C and H_S in the magnetization reversal process.

1.5.1 Domain wall motion:

In a magnetic material, the magnetic moments (spins) of atoms or ions tend to align in regions called magnetic domains. Each domain has a uniform magnetization direction. When an external magnetic field is applied, it can influence the orientation of these domains. Magnetization reversal via domain wall motion involves the movement of the boundaries (domain walls) between adjacent domains. There are different types of domain walls, such as Bloch walls and Néel walls, depending on the magnetization texture of the material. Domain

wall motion can occur through various mechanisms, such as pinning and depinning of domain walls, nucleation and propagation of new domains, and annihilation of existing domains [43,44]. Figure 1.6 (a) depicts the process of magnetization reversal via domain wall motion. The movement of domain walls can lead to a global change in the magnetization direction of the material. Further, we will discuss about the domains and domain walls elaborately.

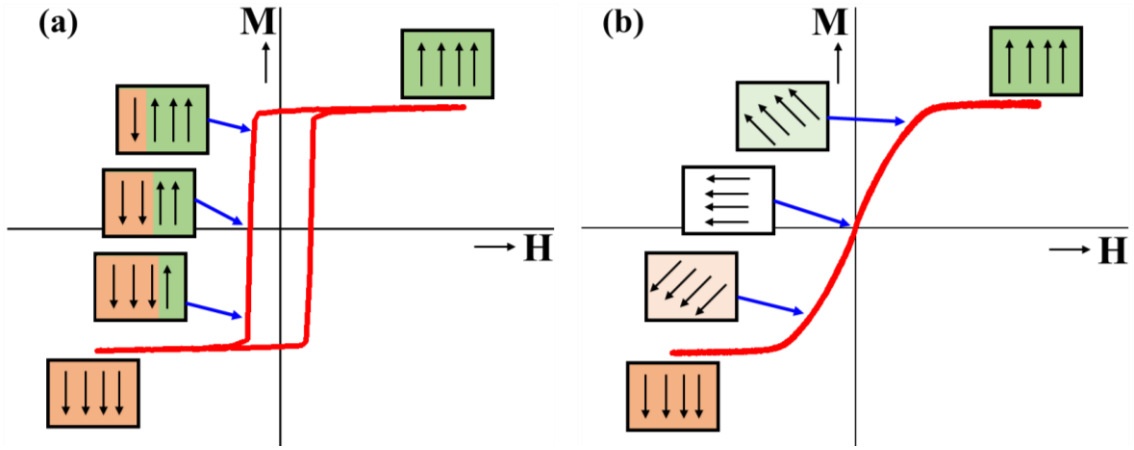

Figure 1.6: Schematic illustration of the magnetization reversal via (a) domain wall motion and (b) coherent rotation.

1.5.2 Coherent rotation:

Coherent rotation involves the simultaneous rotation of all magnetic moments in the material. This mechanism is predominant in single-domain nanoparticles or thin films with strong shape anisotropy. When an external magnetic field is applied, it exerts a torque on the magnetic moments, causing them to rotate collectively. When the magnetization M of a single domain is away from the easy axis, coherent rotation occurs [43,44]. Figure 1.6 (b) depicts the process of magnetization reversal via domain wall motion. The sample's magnetic moment rotates against the force associated with particular anisotropies, such as shape, stress, crystal anisotropy, or a combination of these. Coherent rotation is characterized by a smooth, continuous change in magnetization without the formation or movement of domain walls. It is often observed in

systems with high magnetic anisotropy energy, where the magnetization prefers to align along a specific direction determined by the material's crystal structure or shape.

1.6 Domains and domain walls:

In magnetic material, a domain is an area where all of the magnetic moments are parallel to one another. This concept was first introduced by Pierre Weiss in 1907 [45]. A magnetic material with finite exchange and anisotropy energy should ideally exist in a single domain state with all of the spins aligned in one direction. However, the stray field energy increases significantly in such situations. A single domain state is split up into several domains in order to lower this energy, and each domain's spontaneous magnetization can be directed in any direction. A domain wall (DW), or wall with a finite width, divides two domains with distinct magnetization orientations. Magnetic moments constantly rotate within the DW, shifting their orientation from one easy direction to another. A substantial exchange energy comes from the antiparallel alignment of magnetization of two adjacent domains. This is because the exchange energy favours the parallel orientation of spins. To reduce the exchange energy, it tries to create a broad DW in which the neighbouring spin moments rotate at a relatively tiny angle. However, because many spins are aligned along a direction away from easy axis, crystalline anisotropy does not favour such a small rotation. Consequently, anisotropy energy attempts to minimize wall width. A finite width of the DW ultimately results from the balancing of these two energies [46]. With this process, a finite amount of energy is acquired by the spin moment known as DW formation energy (σ_{DW}). A continuum model approach is considered to calculate the width and energy of the DW [34]. The energy associated with the formation of a domain wall (DW) in a magnetic material can be calculated by considering the interplay between exchange energy and anisotropy energy. The rate at which the direction of the magnetization

change with respect to the position is denoted as $\frac{d\varphi}{dx}$ and using this, the exchange energy of the system is written as [34],

$$E_{exch} = -2Acos\frac{d\varphi}{dx} \quad \text{……. (1.17)}$$

Considering n number of atoms per unit cell with the lattice parameter a, the exchange stiffness constant A is denoted as $A = \frac{nJS^2}{a}$. As φ is very small, so the higher order terms in the expansion of $cos\frac{d\varphi}{dx}$ in equation 1.17 can be neglected. Thus,

$$E_{exch} = -2A + A\left(\frac{d\varphi}{dx}\right)^2 \quad \text{……. (1.18)}$$

The 1st and 2nd term in the above expression represents a constant term and the exchange energy, respectively. Further, by considering φ as the angle between the direction of magnetization and the direction of easy axis, the anisotropy energy is written as,

$$E_{ani} = g(\varphi) \quad \text{……. (1.19)}$$

Further, by differentiating the energy terms with respect to φ, the torque associated with the two energies can be calculated. In principle, for a finite DW width, both the torque should balance each other giving rise to zero net torque. With all these above considerations, at equilibrium, we get,

$$2A\frac{\partial^2\varphi}{\partial x^2} + \frac{\partial g(\varphi)}{\partial \varphi} = 0 \quad \text{……. (1.20)}$$

From the above equation, by multiplying with $\frac{\partial\varphi}{\partial x}$ and integrating over x, we get,

$$A\left(\frac{\partial\varphi}{\partial x}\right)^2 = g(\varphi) \quad \text{……. (1.21)}$$

The DW formation energy, σ_{DW} can be evaluated as,

$$\sigma_{DW} = \sigma_{exch} + \sigma_k = \int_{-\infty}^{\infty} \left[A \left(\frac{\partial \varphi}{\partial x} \right)^2 + g(\varphi) \right] dx \quad \ldots\ldots (1.22)$$

$$\Rightarrow \sigma_{DW} = \int_{-\infty}^{\infty} 2g(\varphi)\, dx \quad \ldots\ldots (1.23)$$

For $g(\varphi) = K_U sin^2 \theta$,

$$\sigma_{DW} = 2\sqrt{AK_U} \int_0^{\pi} Sin\varphi\, d\varphi = 4\sqrt{AK_U} \quad \ldots\ldots (1.24)$$

Here, A and K_U represent the exchange and uniaxial anisotropy constants, respectively. Further, by evaluating the value of $\frac{d\varphi}{dx}$ at the center of the wall, the DW width can be written as,

$$\delta_{DW} = \pi \sqrt{\frac{A}{K_U}} \quad \ldots\ldots (1.25)$$

In fact, the balance between the DW formation energy and the stary field energy gives rise to the formation of multiple domains at the ground state. The flux closure as a result of the minimization of stary field energy is depicted in Figure 1.7 [47].

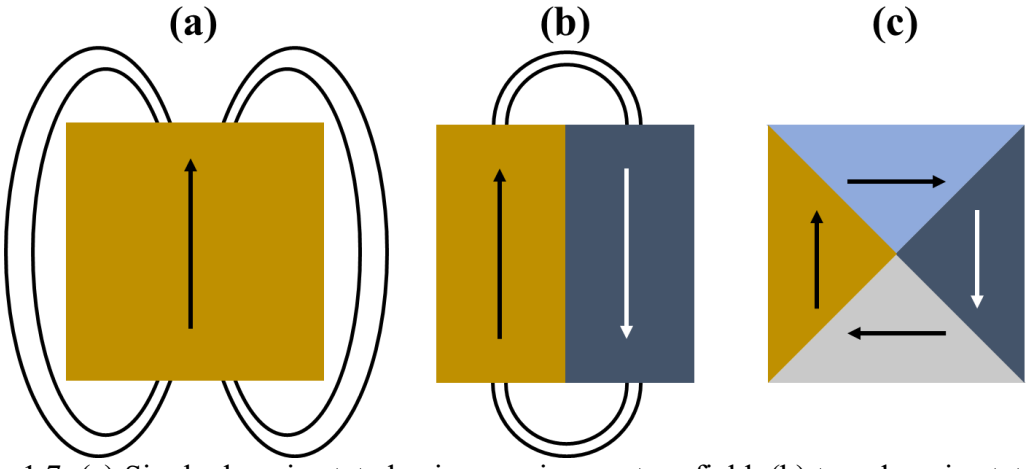

Figure 1.7: (a) Single domain state having maximum stray field, (b) two domain state with reduced stray field, (c) multi domain state with zero stray field. This happens due to the flux closure property of magnetic domains.

In a magnetic material, usually, two types of DW are encountered i.e., Neel wall [48] and Bloch wall [46]. It depends on the rotation of magnetization inside the DW. The orientation of spins in the region separating the two domains have been shown in Figure 1.8.

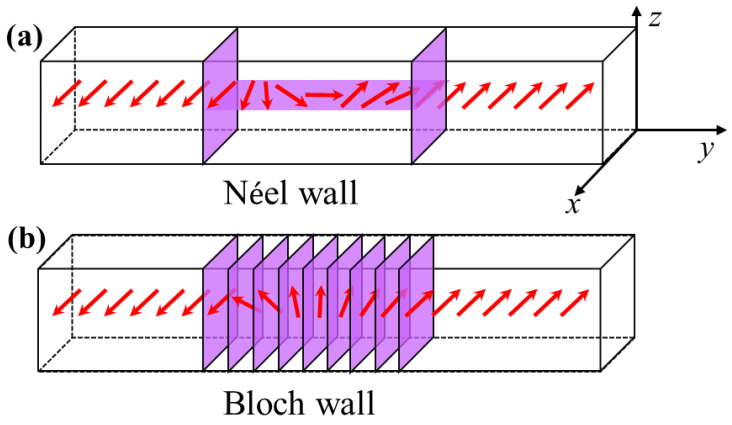

Figure 1.8: Schematic representation of (a) Neel wall and (b) Bloch wall. The red arrows show the direction of magnetization.

The magnetization for the Neel wall rotates in a plane perpendicular to the DW plane, whereas for the Bloch wall, it rotates in a plane parallel to the DW plane. Usually, Neel walls form in materials with in-plane magnetic anisotropy, where the magnetic moments prefer to align parallel or antiparallel to the plane of the material. The energy associated with maintaining the magnetization in the plane is minimized in this case. On the contrary, Bloch walls form in materials with perpendicular magnetic anisotropy, where the magnetic moments prefer to align perpendicular to the plane of the material. Therefore, it becomes easy for the moments to be aligned in perpendicular direction, thereby minimizing the energy. However, in presence of iDMI in a PMA system, the interaction of DMI, anisotropy, and exchange energy determines the lowest energy domain wall configuration. The DW formation energy with the introduction of a homochiral Neel wall induced by DMI in this case is modified as [34,49],

$$\sigma_{DW} = 4\sqrt{AK_U} \pm \pi D \qquad \ldots\ldots (1.26)$$

Here, *D* id the iDMI constant. The chirality of the DW is decided by the sign of the iDMI vector. Understanding these concepts are very crucial in understanding the field of skyrmions which are going to be discussed in the next section.

1.7 Skyrmions:

Skyrmions are fascinating magnetic structures that have gained significant attention in the field of condensed matter physics and materials science. They were first proposed by Tony Skyrme in the context of particle physics in 1961 [50]. Further, they were experimentally observed in condensed matter systems, particularly in magnetic materials. The history of magnetic skyrmions can be traced back to the theoretical work of Bogdanov and Yablonskii in 1989 [51], who predicted the existence of a new type of magnetic structure in chiral magnets. This prediction laid the foundation for the subsequent experimental discovery of skyrmions in various magnetic materials, such as thin films, multilayers, and bulk crystals. It was first discovered experimentally in a B20 type bulk MnSi material in 2009 [52]. These are basically topologically stable spin textures that can form in certain magnetic materials. They are characterized by a swirling arrangement of magnetic moments, creating a localized vortex-like structure. The formation of magnetic skyrmions is often facilitated by the presence of chiral interactions in the material, such as the Dzyaloshinskii-Moriya interaction (DMI) [38,39], which arises from the lack of inversion symmetry at the atomic level. This chiral interaction gives rise to a preference for certain spin configurations, leading to the stabilization of skyrmions.

Depending on the orientation of spins from the skyrmion core to the periphery, these spin textures are categorised into two types, i.e., Neel skyrmion and Bloch skyrmion [53,54]. In Néel skyrmions, the spins rotate in the plane parallel to the skyrmion core. This means that by moving from the center of the skyrmion core to its periphery, the direction of the spins rotates

around the core. These are typically stabilized in materials with strong perpendicular magnetic anisotropy (PMA) and interfacial Dzyaloshinskii-Moriya interaction (DMI) arising from the interface of FM/HM layers.

The PMA favours the spins to align perpendicular to the material plane, while the DMI introduces chirality, leading to the formation of Néel-like spin configurations. In Bloch skyrmions, the spins rotate in the plane perpendicular to the skyrmion core. Moving from the centre of the skyrmion core to its periphery, the spins undergo a rotational motion in a plane perpendicular to the core. These skyrmions are usually stabilized in non-centrosymmetric bulk material with bulk DMI. Schematics of both types of skyrmions are shown in Figure 1.9 (a)

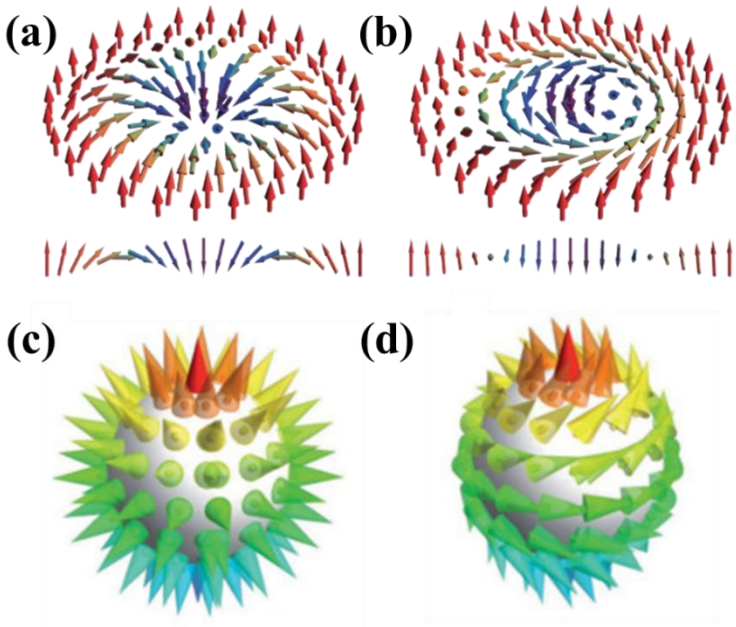

Figure 1.9: Representation of the spin configuration of a (a) Neel skyrmion, (b) Bloch skyrmion. The image is taken with permission from I. Kezsmarki *et. al.,* Nat. mat. 14,1116–1122 (2015) [55]. Copyright 2015, Springer Nature Limited. (c) and (d) represent the stereographic projection of Neel and Bloch skyrmion, respectively, on to a sphere. This figure is taken with permission from C. Pfleiderer *et. al.,* Nat. Phys 7, 673–674 (2011) [56]. Copyright 2011, Springer Nature Limited.

and (b). Both type of skyrmion can be mapped onto a sphere via stereographic projection which is shown in Figure (c) and (d).

1.7.1 Properties of Skyrmions:

While discussing about skyrmions, every time we come across a term “topological protection” or “topological stability” of these quasi particles (skyrmions). Skyrmions are characterized by a nontrivial topological charge, often denoted as Q or N, which quantifies the degree of spin rotation within the skyrmion texture or the number of times the spin configuration wraps the surface of a sphere. Considering the space varying function **m (**x, y**)** as the local orientation of magnetization, the skyrmion number can be expressed mathematically as [57,58],

$$Q_{sk} = \frac{1}{4\pi}\iint m.\left(\frac{\partial m}{\partial x}\times\frac{\partial m}{\partial y}\right)dxdy \qquad \ldots\ldots (1.27)$$

The skyrmion number or the topological number is an integer value and reflects the winding of spins around the skyrmion core. This topological protection ensures the stability of skyrmions against certain perturbations. Skyrmions also exhibit chirality, meaning that the spin configuration within the skyrmion texture is non-collinear and possesses a preferred rotational sense. The chirality of skyrmions arises from the Dzyaloshinskii-Moriya interaction (DMI), which introduces asymmetric exchange interactions favouring specific spin configurations. Due to their nontrivial topological charge and chirality, skyrmions are topologically stable. This stability implies that small perturbations or defects in the material do not easily destroy the skyrmion texture. As discussed earlier, skyrmions can be differentiated two types i.e., Neel and Bloch, by the change of direction of spins from their core towards the periphery. However, for both of these skyrmion types, this rotation can happen in both right- and left-handed directions which results the magnetization structure to point clockwise or anticlockwise manner for both type of skyrmions. Hence, the structure of the skyrmions can be characterized based on three factors such as, topological charge or skyrmion number, their helicity and their vorticity. By parametric equation, a point in the x-y plane can be written as, $x=r\cos\varphi$ *and* $y=r\sin\varphi$. It defines the position of individual magnetization in 2D. Further, in order to represent the spin texture of

skyrmions in 3D considering its relative orientation from core to the periphery, we need to express the magnetization in spherical polar coordinate as,

$$\boldsymbol{m}\,(\theta,\phi) = (sin\theta cos\phi, sin\theta sin\phi, cos\theta) \qquad \ldots\ldots (1.28)$$

For simplicity, considering ϕ to be constant w.r.t. r, equation 1.28 can be written as [54,58,59],

$$Q_{sk} = \frac{1}{4\pi}\int_{r=0}^{\infty}\int_{\varphi=0}^{2\pi}\frac{d\theta}{dr}sin\theta\,\frac{d\phi}{d\varphi} = \frac{1}{4\pi}[-cos\theta(r)]_{r=0}^{r=\infty}[\phi(\varphi)]_{\varphi=0}^{2\pi} = P.V \qquad \ldots\ldots (1.29)$$

Here, P and V represents the polarity and vorticity of skyrmions. Further, by considering the helicity degree of freedom, it can be written as,

$$\phi = V\varphi + \gamma \qquad \ldots\ldots (1.30)$$

Here, γ represents the helicity. In other words, it indicates the tilting of magnetization w.r.t. the radial axis. We can now obtain several forms of skyrmions with varied chirality depending on P and φ.

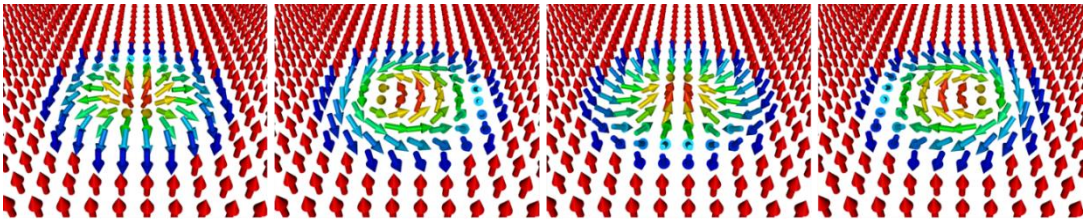

Figure 1.10: Representation of magnetic skyrmions having topological charge (Q_{sk}) =1, vorticity (V) = 1 and helicity (φ) = 0, π/2, π and 3π/2. These skyrmion images are simulated by using the Spirit software [61].

The Néel skyrmions are defined by the radial axis along which the magnetization spins cycloidally i.e., for φ= 0 or π the skyrmions are Neel skyrmions with right and left-handed chirality, respectively. Likewise, right and left-handed Bloch skyrmions are associated with φ= π/2 or 3π/2, respectively, which favours helicoidal configurations. The vorticity, V can be +1

or -1 for skyrmion or anti-skyrmion, respectively [40,60]. Depending on these parameters, various types of skyrmions have been shown in Figure 1.10. The direction of the skyrmion core is corelated with the sign of the skyrmion number Q_{sk}. For ex, for Q_{sk}=+1, the product of V and Q_{sk} becomes +1 for skyrmions. This indicates the skyrmion core points in up direction.

1.7.2 Stabilization, nucleation and detection of skyrmions:

In magnetic systems, skyrmions can be stabilized by a variety of mechanisms, many of which contribute simultaneously. The leading interactions which impact the stabilization of these chiral spin textures are exchange interaction, anisotropy [62,63], Dzyaloshinskii-Moriya interaction (DMI) [58], frustrated exchange interaction [64], dipolar interaction [65], four-spin exchange interactions [66], etc. In ferromagnetic materials, the Heisenberg exchange interaction prefers the parallel alignment of spins and DMI makes the spin texures aligned in a non-collinear manner. The competition between these two interactions leads to the formation of skyrmions in the systems. In another example of magnetic thin films with out-of-plane anisotropy, skyrmions may be formed due to the dipolar interactions [65]. The dipolar interaction tries to align the spins in the plane. Periodic stripes are produced when the magnetization rotates in a plane perpendicular to the thin film as a result of the balance among this dipolar and other interactions like exchange, DMI, etc. Further, by applying a perpendicular magnetic field, these stripes may turn into magnetic skyrmions.

Having a good control of these interactions experimentally, one can nucleate skyrmions in a magnetic material, which is a crucial step for their practical applications, especially in data storage and spintronics. There are several methods to nucleate skyrmions, and these methods often involve manipulating the material's magnetic properties. Some of the methods for the nucleation of skyrmions are such as appropriate material engineering [67,68], applying external magnetic field [69,70], applying spin polarized current [71–73], localized defects,

ultrafast laser pulses [74,75] etc. The choice of nucleation method depends on the specific requirements of the application and the properties of the magnetic material being used. Researchers continue to explore and develop novel techniques to enhance the control and efficiency of skyrmion nucleation for various technological applications.

The smooth detection of these chiral spin structure for prospective applications in various fields is an important aspect of this investigation. Numerous techniques have been devised by researchers to identify the presence and properties of skyrmions in magnetic materials. A few of them can be mentioned here such as topological Hall effect measurements, Lorentz transmission electron microscopy (LTEM) [71,76], scanning tunnelling microscopy (STM) [77], X-ray photoemission electron microscopy (XPEEM) [75], magnetic force microscopy (MFM) [69], magneto-optic Kerr effect (MOKE) microscopy [28,78], etc. Most of the imaging techniques mentioned here are used for the direct observation of these spin textures. However, indirect measurements such as topological Hall effect (THE) is also very crucial in this regard to confirm the presence as well as chirality of these quasi particles. This phenomenon is observed in magnetic materials hosting topologically nontrivial spin textures, such as skyrmions. It arises due to the Berry curvature associated with the spin textures and can lead to a transverse deflection of charge carriers, resulting in a Hall voltage perpendicular to the applied electric current.

M. Raju *et. al.* have shown the nucleation of high density skyrmions in a multilayer of Ir/Fe/Co/Pt [79]. S. Woo *et. al.* have demonstrated the observation of skyrmions at room temperature in multilayer systems of Pt/Co/Ta and Pt/CoFeB/MgO [80]. They have also studied the current driven dynamics in these systems. C. Moreau-Luchaire et. al. have shown the stabilization of isolated skyrmions in a Pt/Co/Ir multilayer system with additive interfacial chiral interaction [81]. Figure 1.11 shows the skyrmion images observed via MFM in the work by M. Raju *et. al.* mentioned above. The plot in the middle shows the observation of topological

Hall effect in this system due to the presence of skyrmions in it. There are many other reports where the nucleation, detection as well as propagation of these spin textures have been widely investigated. A few of these works can be found in these review papers [15,60,68,82–85].

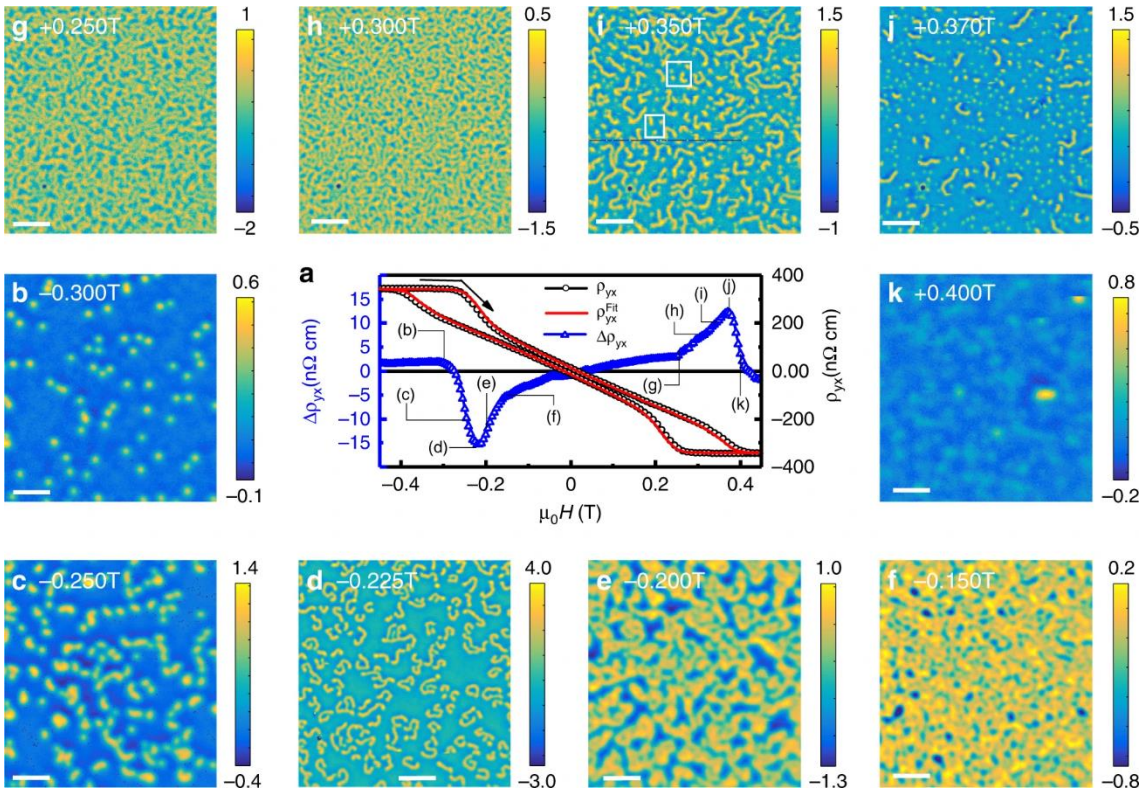

Figure 1.11: Skyrmions observed in the system of Ir/Fe/Co/Pt multilayers at 5K. The plot (a) in the middle shows the topological Hall effect (THE) signal arising due to the presence of skyrmions. This image is adapted with permission from the paper M. Rjau *et. al.,* Nat. Commun. 10, 696 (2019) [79]. Copyright 2019, Springer Nature Limited.

1.7.3 Emergent dynamics of skyrmions:

Moving the skyrmions in a particular direction is the most important as well as very crucial part in this field of research for application purposes. This is referred to as the dynamics of skyrmions which focuses on the study of their movement, interaction and response to the applied external force. Utilizing different physical principles and mechanisms, there are several methods to move a skyrmion along a track such as, current induced motion [73,86,87],

magnetic field gradient [88,89], spin-orbit torques (SOT) [90,91], temperature gradient [92,93], etc. Zhang *et. al.,* have experimentally demonstrated the manipulation of skyrmions by using field gradient, where the spatially varying magnetic field displaces the skyrmions after being nucleated by the field pulse [88]. Recently, in another work by Casiraghi et. al., the movement of skyrmions has also been seen by the stray field arising from the MFM tip [89]. However, in the case of field-induced motion, the use of this method is limited due to the requirement of a significant field gradient in order to obtain high mobility of skyrmions.

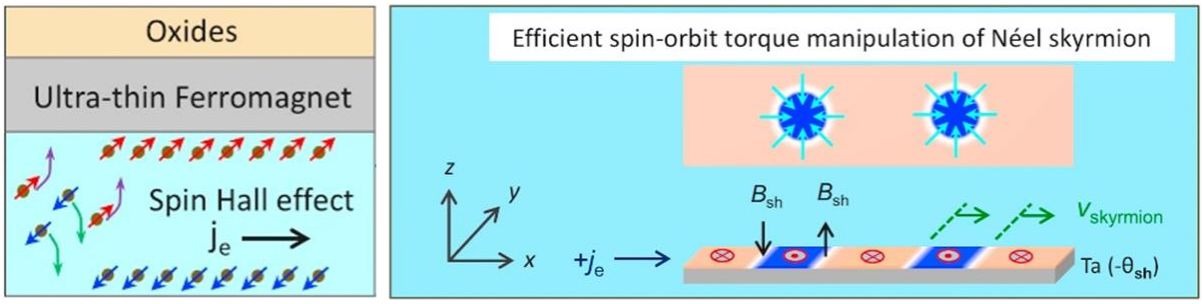

Figure 1.12: Illustration of the efficient electrical manipulation of magnetic skyrmions via spin orbit torque (SOT) as a result of the spin Hall effect in the heavy metal layer. This figure is adapted from W. Jiang *et. al.,* Physics Reports, 704, 1-49 (2017) [68]. Copyright 2017, Elsevier.

The mobility of the skyrmions under the application of a spin-polarized current is also an efficient method to manipulate the magnetization dynamics of these quasi particles for spintronic application. There are two possible scenarios in this regard. One is the spin-transfer torque (STT) induced skyrmion motion, where a spin polarized current passes through the skyrmions and reorients the magnetic moments of these spin textures. Another is spin-orbit torque (SOT) induced motion, where a spin accumulation caused by an electric current in the presence of spin-orbit interaction exerts a torque τ on the skyrmion texture. The strong spin-orbit coupling (SOC) inherent in heavy metals (HMs) plays a pivotal role in facilitating the formation of Néel-type skyrmions within interfacial asymmetric systems. This same robust

SOC also leads to the spin-dependent scattering of incident conduction electrons, causing a notable spin imbalance perpendicular to the direction of motion. This phenomenon, often referred to as the electronic spin Hall effect (SHE), specifically involves the preferential scattering of spin-up and spin-down electrons. In the context of an HM/ferromagnet (FM) bilayer, the build-up of spins at the interface subsequently transfers their spin angular momentum to the nearby ultra-thin FM layer (shown in Figure 1.12). This transfer is pivotal, giving rise to current-induced spin-orbit torques (SOTs) that encompass both a field-like torque and an anti-damping-like torque. This distinct spin torques, in turn, yield an effective means of electrical manipulation of the skyrmions. This torque term can be written as [60],

$$\tau = \frac{\gamma_e \hbar}{2edM_s}\ \theta_{SHE} j[(\boldsymbol{m} \times \boldsymbol{s}) \times \boldsymbol{m}] \qquad \ldots\ldots. (1.31)$$

Where, γ_e is the gyromagnetic ratio of an electron, d is the thickness of the ferromagnetic layer, M_s is the saturation magnetization. The term $\theta_{SHE} j$ represents the spin current with θ_{SHE} being the spin Hall angle. Further, by solving this equation for a FM system having skyrmions, it can be attributed that the applied current moves the skyrmion along the direction of the current. Thus, skyrmions can be driven efficiently by the spin-polarized current. In addition to the motion along the current direction, skyrmions also experience a transverse motion perpendicular to the direction of the applied current or magnetic field and move to the edge of the track. This effect is a result of the "Magnus force" acting on the skyrmions, which arises due to the topological properties of these nontrivial spin texture. As a consequence of this, either they move parallel to the track due to repulsive interaction at the edge or they annihilate. This motion, away from the direction of applied current, is well known as skyrmion Hall effect (SkHE) and is governed by the Thiele's equation [94,95],

$$G \times v - 4\pi\alpha D.v + 4\pi\ \beta.j = 0 \qquad \ldots\ldots. (1.32)$$

Here, G is the gyrocoupling vector i.e., $G=(0, 0, -4\pi Q)$, v consists of the x and y components of the velocity of the skyrmion, α is the Gilbert damping coefficient, β denotes the efficiency of the torque due to spin Hall effect, j is the electrical current density. The symbol D is a tensor quantity known as dissipative force tensor [68]. By solving the equation 1.32, the velocities along the x and y directions are found to be [27,96],

$$v_x = \frac{-\alpha D}{Q^2 + \alpha^2 D^2} B_0 j_x, \qquad v_y = \frac{Q}{Q^2 + \alpha^2 D^2} B_0 j_x \qquad \ldots\ldots (1.33)$$

The constant B_0 can be evaluated from the spin configuration of skyrmion. Then, the ratio of v_y and v_x becomes,

$$\frac{v_y}{v_x} = -\frac{Q}{\alpha D} \; and, \; \Theta_{sk} = \tan^{-1}\frac{v_y}{v_x} \qquad \ldots\ldots (1.34)$$

where, Θ_{sk} is the skyrmion Hall angle defined as the angle of deflection of the skyrmion motion away from the applied current direction. The transverse motion of skyrmion away from the applied current direction, has been depicted in Figure 1.13 (a).

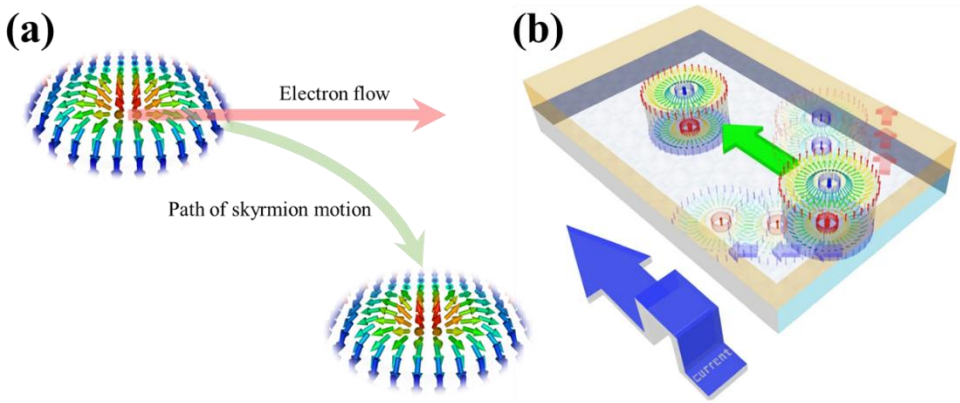

Figure 1.13: (a) Illustration of skyrmion Hall effect during the motion of skyrmion by the application of electrical current, (b) reduction of skyrmion Hall effect by using an SAF track. This image is adapted with permission from T. Dohi *et. al.,* Nat. Commun. 10, 5153(2019). Copyright 2019, Springer Nature Limited.

For practical application purpose, it is ideal to have a zero skyrmion Hall angle. However, in a FM thin film hosting skyrmions, always there exists a finite Θ_{sk} which is not desired for application. In order to overcome this drawback, a system of SAF has been proposed [14,28,71]. Here, two skyrmions with opposite skyrmion number get nucleated in the two FM layers below and above the spacer layer. With the application of current for the motion of these quasi particles, both of them try to move in opposite transverse direction. However, due to the antiferromagnetic coupling, both the skyrmions don't get decoupled and move in a straight-line path along the applied current direction thus, minimizing the SkHE (see Figure 1.13 (b)). There is another system of synthetic ferrimagnets which also helps in reducing the SkHE in the system [80].

1.8 Magnetization dynamics:

The study of how a material's magnetization varies over time in response to external stimuli is referred to as magnetization dynamics. The Landau-Lifshitz-Gilbert (LLG) equation is a fundamental equation in the study of magnetization dynamics.

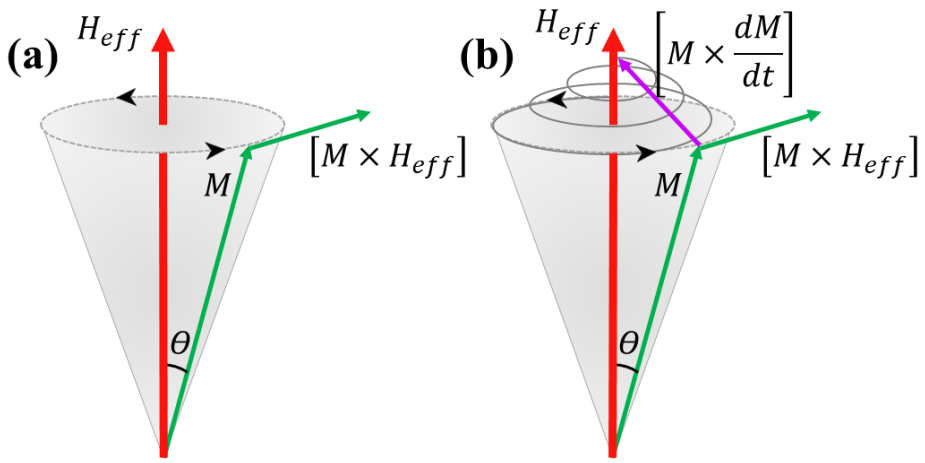

Figure 1.14: Precession of magnetization around the effective magnetic field (a) in the absence and (b) presence of damping in the system, respectively.

It describes the time evolution of the magnetization vector in a magnetic material under the influence of an external magnetic field and damping effects. Primarily the torque equation was developed by Landau and Lifshitz [97] and later the damping term was introduced by Gilbert [98]. The revolution of an electron around the atomic nucleus leads to the generation of magnetic moment which can be expressed as, $\boldsymbol{m} = -\gamma \boldsymbol{l}$, where, $\gamma = \frac{g\mu_B}{\hbar}$ and $\boldsymbol{l}$ is the angular momentum of electron. g and μ_B represent the Lande g factor and Bohr magnetron, respectively. The rate of change of angular momentum i.e., the torque (τ) can be written as [99],

$$\boldsymbol{\tau} = \frac{d\boldsymbol{l}}{dt} = -\frac{1}{\gamma}\frac{d\boldsymbol{m}}{dt} \qquad \ldots\ldots. (1.35)$$

Also, in presence of an applied magnetic field, the magnetic moment experiences a torque to get aligned along the applied field direction. Hence,

$$\boldsymbol{\tau} = m \times H_{ext} \qquad \ldots\ldots. (1.36)$$

Comparing equation 1.35 and 1.36, we can write,

$$\frac{d\boldsymbol{m}}{dt} = -\gamma(m \times H_{ext}) \qquad \ldots\ldots. (1.37)$$

In real scenario, apart from the applied magnetic field acting on the magnetic moment, several other contributions are there combinedly known as the effective magnetic field (H_{eff}). These are the contributions arising due to exchange, anisotropy and demagnetization energy. So, the effective field can be written as,

$$H_{eff} = H_{ext} + H_{exch} + H_{anis} + H_{demag} \qquad \ldots\ldots. (1.38)$$

Further, considering the magnetization M which is the magnetic moments per unit volume, the equation 1.38 can be written as

$$\frac{d\boldsymbol{M}}{dt} = -\gamma(M \times H_{eff}) \qquad \ldots\ldots. (1.39)$$

Equation 1.39 signifies the precessional motion of the magnetization w.r.t. the effective magnetic field making an angle θ as shown in Figure 1.14 (a). The precession does not, however, go on forever in the case of an actual system. Rather, it gradually gets damped out and lines up with the direction of the effective field (shown in Figure 1.14 (b)). Equation 1.39 was thus modified by the addition of a damping term (2nd term in equation 1.40 below) by Landau-Liftshitz (LL), and the resultant equation having both the field like torque and damping like torque is expressed as [99],

$$\frac{d\boldsymbol{M}}{dt} = -\gamma\left(\boldsymbol{M} \times \boldsymbol{H}_{eff}\right) - \frac{\lambda}{M_s^2}\left[\boldsymbol{M} \times \left(\boldsymbol{M} \times \boldsymbol{H}_{eff}\right)\right] \quad \ldots\ldots. (1.40)$$

Here, λ represents the phenomenological damping term. Further, a dimensionless parameter $\alpha = \frac{\lambda}{\gamma M_s}$, was introduced by Gilbert which accounts for the damping in the system. This is also known as Gilbert damping parameter. Hence the equation 1.40 is modified further as,

$$\frac{d\boldsymbol{M}}{dt} = -\gamma\left(\boldsymbol{M} \times \boldsymbol{H}_{eff}\right) + \frac{\alpha}{M_s}\left[\boldsymbol{M} \times \frac{d\boldsymbol{M}}{dt}\right] \quad \ldots\ldots. (1.41)$$

The equation 1.41 is well known as the Landau-Liftshitz-Gilbert (LLG) equation. This describes the dynamics of magnetization including the effects of an external magnetic field, damping, and the interaction between the magnetization vector and its time derivative. Two Important properties of the magnetization shown in Figure 1.14, should be noted here i.e., (i) the length of the $|\boldsymbol{M}|$ is constant and (ii) the direction of the magnetization precession is always anti-clockwise [100].

1.9 Spin waves and magnons:

A spin wave is considered as a collective excitation of spins in a magnetic material. In simple terms, it is a wave-like disturbance in the orientation of magnetic moments (spins) within the

material [101,102]. When one spin deviates from its equilibrium position, it can influence the orientations of neighbouring spins through exchange or dipolar interactions. This collective motion of spins propagates through the material as a spin wave, first introduced by Felix Bloch in 1930 [103]. A schematic of the spin waves is shown in Figure 1.15. Many factors such as, magnetic field, temperature, electromagnetic waves, spin polarized current etc., can act as external perturbation which has the potential to create spin waves by inducing a disturbance in the ferromagnetic spins. In terms of physical properties and behaviour, there are many similarities between spin waves and lattice waves. For instance, the oscillations of the atoms happen with respect to their equilibrium positions in a lattice wave and these oscillations occur through elastic forces. Similarly, in case of spin waves, the precession of spins happen around the equilibrium magnetization, which interact through exchange forces. Spin waves play a crucial role in understanding and manipulating magnetism in materials. They are important in this field of spintronics, where the control and manipulation of spin waves are used for information processing and storage. Additionally, spin waves contribute to phenomena such as magnetic resonance, magnon-mediated spin transport, magnon-magnon coupling, etc.

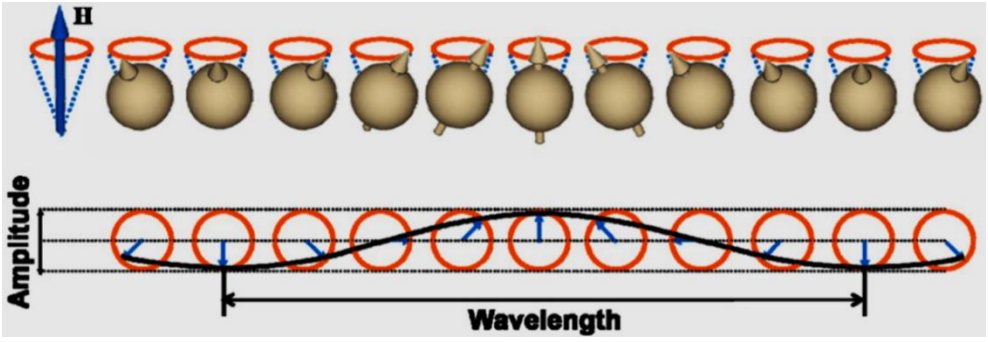

Figure 1.15: Representation of spin waves due to the collective excitation of precessing spins with a certain amplitude and wavelength. The figure is taken with permission from S. K. Kim *et. al.,* J. Phys. D: Appl. Phys. 43, 264004 (2010) [104]. Copyright 2010, IOP publishing.

Further, the energy associated with these wave-like excitation can be quantized into discrete units called quanta. The quantum of these spin waves is known as magnons [102]. Each magnon represents a quantized excitation of the spin wave with a specific energy and momentum. The dispersion relation of magnons describes how their energy and momentum depend on the wave vector (k) of the spin wave. Considering the nearest neighbour interaction, the exchange energy between two consecutive spins with a phase difference θ can be written as [105],

$$E = -2JS^2 cos\theta \qquad \text{……. (1.42)}$$

The difference in energy between this excited (having phase difference θ between two spins) state and the ground state (θ=0) becomes,

$$\Delta E = 4JS^2 sin^2 \frac{\theta}{2} \qquad \text{……. (1. 43)}$$

From this, using $\omega = \Delta E/\hbar$ and $\theta = 2\pi a/\lambda$ the dispersion relation can be deduced as,

$$\omega = \frac{4JS^2}{\hbar} sin^2 \frac{aq}{2} \qquad \text{……. (1.44)}$$

Where, ω is the frequency of oscillation, a is the lattice constant and q is the wave vector. In the long wavelength limit [105],

$$\omega \, \alpha \, q^2 \qquad \text{……. (1.45)}$$

This is known as the magnon dispersion relation. Unlike the dispersion relation of lattice waves where, ω linearly varies with q, the magnon dispersion relation indicates that the group and phase velocities of spin waves are not equal.

Chapter 2

Experimental techniques

In this chapter, an extensive overview of all the experimental techniques has been discussed which are employed for the structural as well as magnetic characterization of the samples. All the samples having thin films of these metals such as Ta, Pt, Co, CoFeB, Ru, and Ir, have been prepared by DC magnetron sputtering on rigid Si or Si/SiO_2 substrate. Structural characterizations of these multilayer samples have been conducted by X-ray reflectivity (XRR) measurement using X-ray diffractometer (XRD) and cross-sectional transmission electron microscopy (TEM) imaging. For magnetic characterization, we have performed our experiments on magneto-optic Kerr effect (MOKE) microscopy, Superconducting Quantum Interference Device vibrating sample magnetometer (SQUID-VSM), and magnetic force microscopy (MFM). Further, the resistivity vs magnetic field (R-H) measurement has been performed for the topological Hall effect (THE) study by physical property measurement system (PPMS). Magnetization dynamics of the in-plane magnetized synthetic antiferromagnets (SAF) have been studied using ferromagnetic resonance (FMR) spectroscopy.

2.1 Thin film deposition techniques:

A thin film is a layer of material that has a thickness on the order of nanometers (nm) to micrometers (μm). These films are deposited onto a substrate, which can be a solid surface or another material. The term "thin" is relative, and the thickness of a thin film is typically much smaller compared to the dimensions of the substrate. Thin films have a wide range of applications across various fields, including electronics, optics, coatings, sensors, and photovoltaics. The properties of thin films can be tailored based on the choice of materials, deposition techniques, and film thickness. Common materials used in thin films include metals, semiconductors, insulators, and organic compounds. The deposition of thin films can be

achieved through various techniques which can broadly be classified into two categories i.e., Physical Vapour Deposition (PVD) [106] and Chemical Vapour Deposition (CVD) [107]. These techniques allow for precise control over the thickness, composition, and structure of the thin films. In PVD, a vapour of solid material is created initially, and then it gets deposited on a substrate. In contrast, vapour from a solid substance undergoes a chemical reaction close to a heated substrate in CVD, thereafter it is deposited on the substrate. Another advantage of PVD over CVD is that the thin film can be deposited at a low working temperature. In this thesis work, we have deposited the samples using PVD based method i.e., sputtering. The technique is described in detail below.

2.1.1 Sputtering:

Having several advantages such as high purity, uniformity, good adhesion, compatibility with multiple substrates as well as for depositing a variety of materials, control over film properties, etc, sputtering has been proven to be a versatile and cost-effective technique for thin film deposition. It involves the removal of atoms or molecules from a target material through the impact of high-energy ions. The process takes place in a vacuum chamber, where a low-pressure inert gas, commonly argon, is introduced [108,109]. This gas serves as the working medium for the sputtering process. An electric field is applied to the gas, leading to the creation of a plasma within the vacuum chamber. This electric field can be generated by applying a direct current (DC) or radio frequency (RF) power source. The high-energy electric field ionizes the Ar, creating a plasma composed of positively charged ions i.e., Ar^+ and electrons. The positively charged Ar ions are accelerated toward the negatively biased target material and collide with the target material's surface. This collision imparts sufficient energy to dislodge atoms or molecules from the target. These sputtered atoms enter the gaseous phase and move freely within the vacuum chamber. The deposition of these sputtered atoms happens onto a substrate, which is typically placed in the line of sight of the target. The substrate can be rotated

to ensure uniform deposition of the target material. As the sputtered atoms settle onto the substrate, they form a thin film layer. The film's properties, such as thickness, composition, and structure, can be controlled by adjusting process parameters like sputtering time, power, and pressure. The deposited thin film inherits the properties of the target material. By selecting different target materials and adjusting process parameters, researchers can tailor the characteristics of the thin film for specific applications. Further, to attain a high deposition rate keeping a low Ar flow, magnetron sputtering is used. A permanent magnet or electromagnet is positioned below the target to create a magnetic field that traps electrons near the target [109–111]. The deposition rate is raised by the localization of electrons, which also contributes to the production of Ar+ ions near the target. Figure 2.1 shows the schematics of the sputtering process. Depending on the type of materials to be sputtered according to their electrical conductivity, the sputtering process can be of two types, i.e., (i) direct current (DC) sputtering, (ii) radio frequency (RF) sputtering.

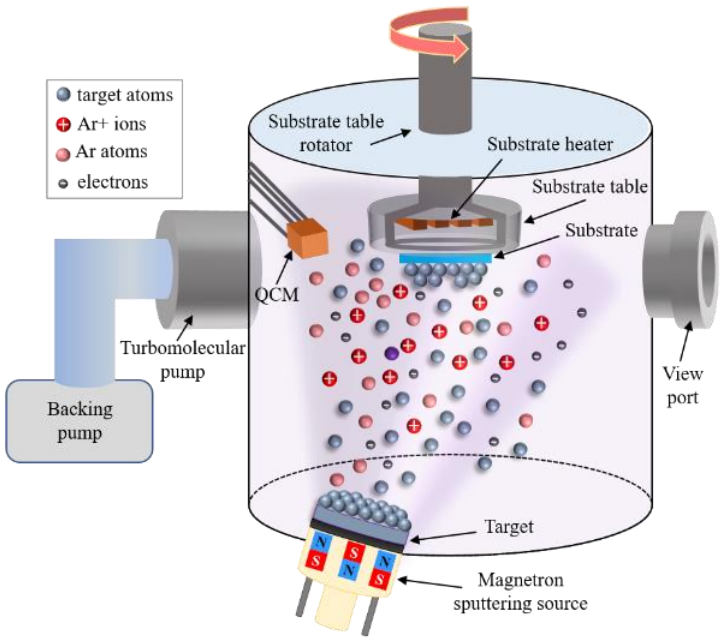

Figure 2.1: Schematic showing the thin film deposition inside a vacuum chamber by sputtering process. A few major components of a sputtering deposition system have also been shown.

DC sputtering: For the deposition of conductive materials, such as pure metals, metallic alloys, conductive oxides, nitrides, etc., DC sputtering is effective, easy to control and a low cost option [112]. In this process, a DC electrical current is applied to the target material to be sputtered. The negative bias due to the DC current is distributed evenly throughout the target because of its conducting nature. When the Ar atoms strike the target substance, Ar^+ ions are produced due to their bombardment with the electrons. Because of the momentum transfer from the argon ions, the target atoms are expelled. These sputtered atoms further go to the substrate and deposit as a thin coating.

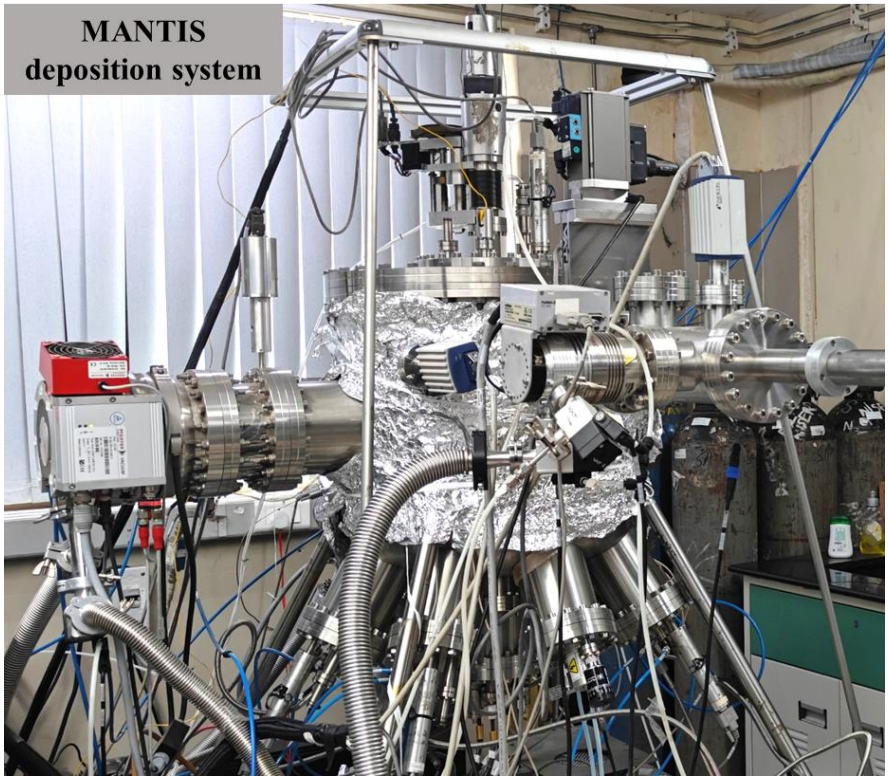

Figure 2.2: Multi deposition system manufactured by MANTIS Deposition Ltd., UK available in our lab at SPS, NISER.

RF sputtering: In the case of insulating target materials, the applied negative potential is not dispersed uniformly throughout the target surface thereby leading to the accumulation of Ar^+ ions on the surface. These accumulated positive charges cease the sputtering process and prevent any additional Ar+ ion bombardment of the target. However, using an RF power supply

provides an alternating electric potential to the target material [113]. On the positive cycle, the electrons are attracted to the target material and neutralize the accumulated Ar^+ ion from the surface. On the negative cycle, Ar^+ ion bombardment continues hence the sputtering process. This whole process occurs at a radio frequency of 13.6 MHz which is used internationally for RF power supply. The deposition rate in the case of RF sputtering is typically modest since the deposition only occurs during the half cycle of the voltage [114]. On the other hand, this method offers more control over the deposition process, enabling the uniform deposition of thin layers.

The samples shown in this thesis work have been deposited by the QPrep multi-deposition system manufactured by Mantis deposition Ltd. UK. The base pressure of this ultra-high vacuum (UHV) system can go up to ~5×10^{-10} mbar. This system consists of two vacuum chambers namely the main chamber and the load lock separated by a pneumatic gate valve. The substrate is mounted in the load lock without breaking the vacuum of the main chamber and further transferred to the main chamber after the vacuum in both chambers becomes of similar order. Two turbo molecular pumps (TMP) are connected in the main chamber and one in the load lock to evacuate the system. All the TMPs are accompanied by backing pumps. Combined full-range gauges are mounted in both chambers to measure the pressure. These full-range gauges are a combination of Pirani and cold cathode gauges. There are nine sources in total in the multi-deposition unit; the thermal evaporator is the central source, while the remaining eight sources are evenly spaced and situated at the cylindrical chamber's lower circular base. In the circular base, all eight of these equally spaced sources form a 45° angle with one another. Below is a list of all the sources:

i. Five unbalanced magnetron sputtering sources (DC and RF)

ii. E-beam evaporator with four pockets

iii. Two thermal evaporation source

iv. One nanoparticle generator source (Nano gen)

v. A Mat-60 unit producing the atomic oxygen from its molecules.

A cooling facility with a chiller is provided for all the sources and also for the TMPs to avoid overheating. The normal of the substrate table located at the center of the upper part of the chamber makes an angle of 30^0 with all the eight sources at the base. The substrate can be heated up to 800^0C with the help of a halogen lamp mounted on the substrate table. The rate of the deposition and the thickness of the films are measured by a quartz crystal microbalance (QCM) mounted near the substrate table. A picture of the multi-deposition unit have been shown in Figure 2.2 present in our lab.

2.2 Structural characterization techniques:

2.2.1 X-ray diffraction and reflectivity:

X-ray diffraction (XRD):

X-ray diffraction (XRD) is a powerful and non-destructive analytical technique used to determine the crystallographic structure of a material [115]. It relies on the principle of X-ray interference, where X-rays are scattered by the atoms in a crystal, resulting in constructive and destructive interference patterns [116,117]. Since the X-ray wavelength (~0.15 nm) is comparable to the atomic spacing in crystals, it can provide a lot of useful information such as crystallinity, lattice parameters, grain size, film thickness, roughness, dislocation density, residual stress/strain, etc. Figure 2.3 (a) depicts the schematic diagram that explains the principle of XRD. The incident X-ray is elastically scattered by the periodic arrangement of atoms inside a crystalline material. The X-rays reflected from the samples are measured in the detector with the variation of angle of incidence (θ) over a wide range. For the constructive

interference of the reflected X-rays, Bragg's condition [118] i.e., $2dsin\theta = m\lambda$, needs to be satisfied. Here, m represents the order of interference, d denotes the distance between consecutive atomic planes and λ is the incident beam's wavelength. For a particular system, the wavelength λ becomes constant. Then the reflected beam's intensities are measured as a function of the angle (2θ) between reflected and incident beams. All the samples in this thesis work have been measured by an automated X-ray diffractometer (SmartLab) manufactured by Rigaku Corporation [119], Japan, with Cu K_α radiation having an average wavelength ~ 0.15nm. The photo of the XRD machine available at NISER, has been shown in Figure 2.3 (b).

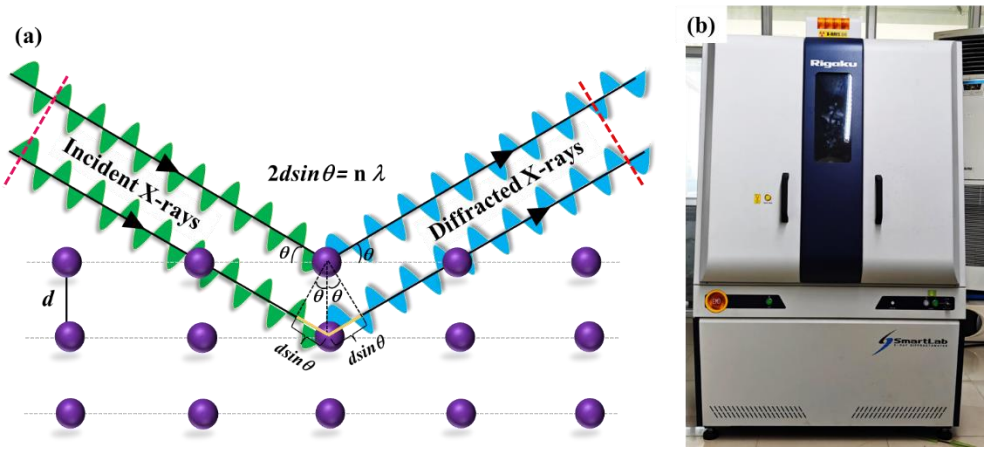

Figure 2.3: (a) Schematic representation of X-ray diffraction from crystallographic planes with interplanar spacing d, (b) multipurpose SmartLab X-ray diffractometer by Rigaku available at SPS, NISER. The inset shows the image of incident optics, receiving optics and the sample stage mounted inside the diffractometer.

X-ray reflectivity (XRR):

X-ray reflectivity (XRR) is an analytical technique used to investigate the structure and properties of thin films and multi-layered structures at surfaces and interfaces [116,120,121]. It is particularly valuable for studying the layer thickness, density, and roughness of thin films with few Angstrom precession [117]. According to Fresnel's reflection, when an X-ray strikes the interface between two media with differing refractive indices, some of the radiation is

transmitted into the second media and some of it is reflected back to the first media. As the X-ray beam falls on the sample surface through air, the refractive index of the sample can be written as,

$$\tilde{n} = 1 - \delta + i\beta \qquad \ldots\ldots. (2.1)$$

Here, $\delta = \frac{\lambda^2}{2\pi} r_e \rho_e$, and $\beta = \frac{\lambda}{4\pi}\mu$. The notations, r_e, ρ_e and μ represent the radius, density, and

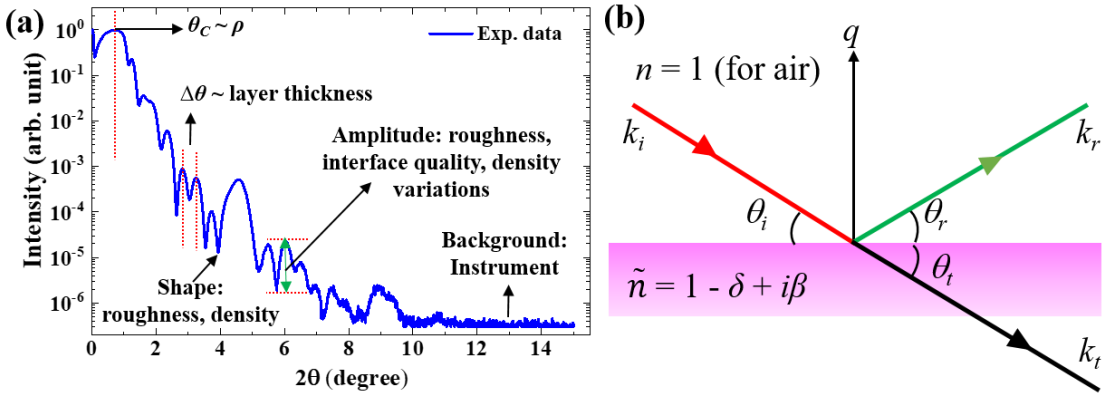

Figure 2.4: (a) A typical XRR spectrum of a thin film sample. The reflected beam's intensity has been plotted as a function of 2θ, (b) schematic representation of the incident (k_i), reflected (k_r) and transmitted (k_t) wave vectors in specular reflection geometry.

absorption length of the electron, respectively. λ represents the wavelength of incident X-ray. Since ρ_e is dependent on the material's density, δ provides information regarding the density of thin films. δ and β signify the scattering mechanism and absorption of X-rays, respectively. A typical XRR plot has been shown in the Figure 2.4 (a).

To comprehend how the graph provides information about the thickness, density, and roughness of multi-layered films, we begin with the Snell-Descartes law, i.e., $n \cos\theta_i = \tilde{n} \cos\theta_t$. Here, θ_i and θ_t are the incident and transmitted angles, respectively (see Figure 2.4 (b)). For specular reflection, θ_i and θ_t are equal. 'n ' is the refractive index of air. In actual measurement where

hard X-rays are used, β becomes very small and thus can be neglected. So after neglecting β from equation 2.1, the Snell-Descartes law becomes,

$$cos\ \theta_i = (1 - \delta)\ cos\ \theta_t \qquad \ldots\ldots. (2.2)$$

All of the X-rays are reflected when they strike the sample surface at very small angles making θ_t to be zero. Thus, for total external reflection, θ_i becomes equal to the critical angle θ_c. Thus, equation 2.2 can be written as $cos\ \theta_c = 1 - \delta$. Here, θ_c being very small, the Taylor series expansion gives $\theta_c^2 = 2\ \delta$. As δ is related to the density of each layer, so θ_c gives information about the density of the thin film layers. The detector receives the highest number of X-rays reflected from the surface because of total external reflection. However, when the critical angle becomes less than the incident angle, the intensity of the X-ray reaching the detector, gets reduced (see Figure 2.4 (a)). So, for $\theta_i > \theta_c$, the Fresnel's reflection coefficient is written as,

$$r = \frac{nsin\theta_i - \tilde{n}sin\theta_t}{nsin\theta_i + \tilde{n}sin\theta_t} \qquad \ldots\ldots. (2.3)$$

For an ideal flat surface, considering the θ_i to be small and using Snell-Descartes law, the equation 2.3 becomes,

$$r = \frac{\theta_i - \sqrt{\theta_i^2 - \theta_c^2}}{\theta_i + \sqrt{\theta_i^2 - \theta_c^2}} \qquad \ldots\ldots. (2.4)$$

Hence, the intensity (I) of the XRR curve is written as,

$$I = R(\theta) = rr^* = \left| \frac{\theta_i - \sqrt{\theta_i^2 - \theta_c^2}}{\theta_i + \sqrt{\theta_i^2 - \theta_c^2}} \right|^2 \qquad \ldots\ldots. (2.5)$$

Depending on the value of θ_i, three cases are discussed below,

(i) For $\theta_i < \theta_c$, $I = R(\theta) = 1$; the detector receives the maximum X-ray intensity

(ii) For $\theta_i = \theta_c$, I gets reduced significantly, as shown in Figure 2.4 (a).

(iii) For $\theta >> \theta_c$, I get reduced as $\frac{1}{\theta^4}$

When $\theta > \theta_c$, X-rays pass through the sample surface and are reflected off of both upper and lower surfaces of the thin film. As a result, both constructive and destructive interference appear, leading to periodic interference patterns in the reflectivity curve known as Kiessig fringes (as seen in Figure 2.4 (a)). Using Bragg's law, the thickness of single layer thin film can be determined as $t = \frac{\lambda}{2\Delta\theta}$. Here, the difference between two successive maxima or minima in the XRR fringes is represented by $\Delta\theta$. A thin film's surface is not always smooth in a real scenario. The off-specular reflection caused by the roughness of the layers reduces the intensity of the XRR curve and the oscillation's amplitude (see Figure 2.4(a)). Therefore, a new component is added to Fresnel's reflection coefficient to add roughness to the reflection coefficient and the modified form is written as [121],

$$r_r = r_f e^{-\frac{q^2\sigma^2}{2}} \qquad \ldots\ldots. (2.6)$$

where, $q = \frac{4\pi}{\lambda} sin\theta$ and σ is the surface roughness. In the case of a multilayer thin film, it is necessary to determine the reflection and transmission that arise from individual interfaces. Therefore, to overcome this problem, a recursive formalism is introduced by Parrat which is used in most of the commercially available X-ray reflectivity simulator. The thickness, roughness, and density of the thin film are thus determined by fitting the experimental data using those simulators. In this thesis work, the XRR measurements have been performed by using a Smartlab diffractometer manufactured by Rigaku Corporation Ltd., Japan, [119] and the analysis have been done by fitting the XRR data using Genx software [122–124].

2.2.2 Transmission electron microscopy (TEM):

Transmission electron microscopy (TEM) is a powerful imaging technique used to visualize the internal structure of materials with extremely high resolution. It relies on the transmission of electrons through a thin specimen to create an image [125,126]. TEM provides information about the atomic arrangement, crystal structure, defects, and morphology of materials at the nanoscale [127].

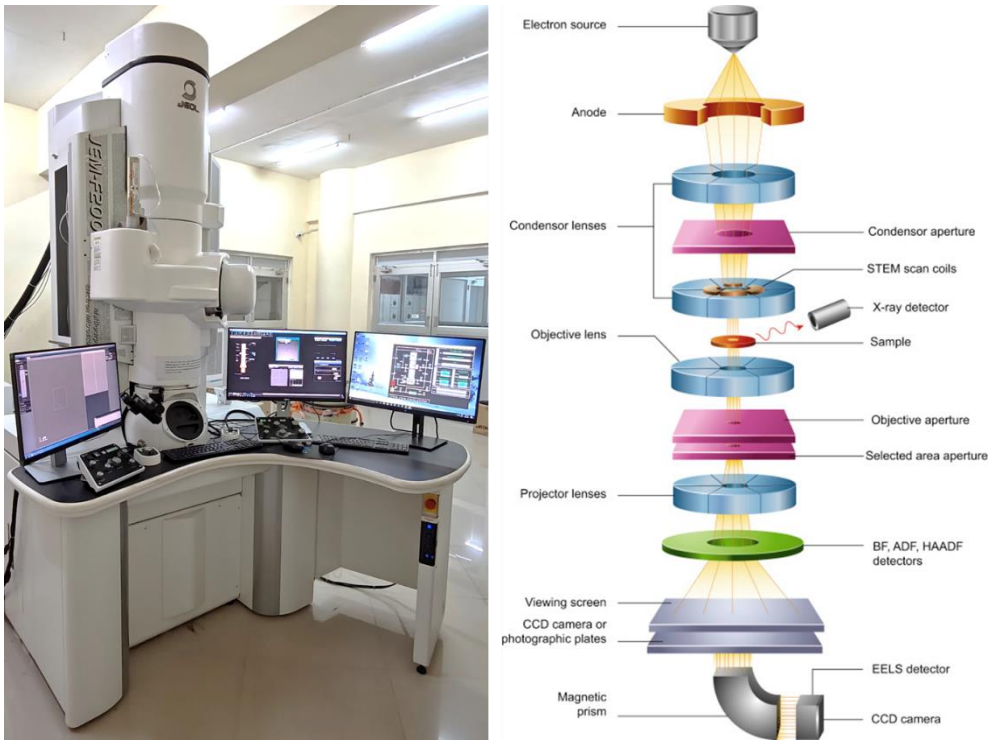

Figure 2.5: (a) Picture of the JEOL JEM-F200 TEM available at CIS, NISER, (b) Schematics of various major components of a TEM. This schematic is taken with permission from [B. J. Inkson, Materials Characterization Using Nondestructive Evaluation (NDE) Methods 17–43 [128]]. Copyright 2016, Elsevier.

Unlike the light source in optical microscopy, here a beam of electrons is generated by an electron gun to characterize the desired specimen. When electrons are accelerated by a strong electromagnetic field, their wavelength can be much shorter than visible light which increases the resolution of a TEM by several orders of magnitude. We have performed structural characterization of our samples with the help of a JEOL JEM-F200 TEM available at the Center

for Interdisciplinary Sciences (CIS), NISER (shown in Figure 2.5 (a)). The schematic of the ray diagram of TEM has been shown in Figure 2.5 (b).

The principles of measurement in TEM is described as follows: An electron beam is produced by a cathode, which consists of a V-shaped tungsten filament. Further, the electron beam is directed toward the sample using condenser lenses which are an arrangement of electromagnetic coils. Samples for TEM must be extremely thin (typically less than 100 nanometers) to allow electrons to pass through. Specimens are prepared by cutting, grinding, and thinning using techniques such as ion milling or focused ion beam (FIB) milling. The thin specimen is placed on a grid and inserted into the TEM column. The electron beam passes through the specimen, interacting with the atoms in the material. Further, the electrons that pass through the specimen interact with a fluorescent screen or detector on the opposite side and the intensity of the transmitted electrons is converted into an image. The transmitted electrons create a magnified image of the specimen's internal structure. By controlling the electron beam's focus and direction, different regions of the specimen can be imaged. TEM can be combined with various analytical techniques, such as selected area electron diffraction (SAED) for crystallographic analysis, energy-dispersive X-ray spectroscopy (EDS) for elemental analysis, etc.

Cross-sectional TEM sample preparation:

Cross-sectional transmission electron microscopy (TEM) sample preparation involves the careful preparation of thin specimens for imaging in TEM, particularly to examine materials' internal structures in a cross-sectional view [129]. There are several steps involved in the preparation of cross-sectional TEM samples. Two small pieces of thin film samples were attached with film sides facing each other by using epoxy glue. Further, a 2.3 mm strip is cut from the attachment using a diamond wire saw which is fitted into a brass tube having an inner

diameter of 2.3 mm and an outer diameter of 3 mm. Then, a circular disc of width approximately 300 µm is cut from the brass tube containing the sample. The disc is then thinned from 300 µm to 100 µm by using a disc grinder on successive emery paper of 40 µm, 15 µm and 5 µm, respectively. On this 100 µm thick disc, a dimple-like structure is made at the center using a dimple grinder which creates a thickness gradient from the center of the disc to the periphery. Then the dimpled surface of the disc is further polished using alumina suspension on the same dimple grinder. Through this process, the thickness of the disc at periphery remains 100 µm and at the center becomes approximately 20 µm.

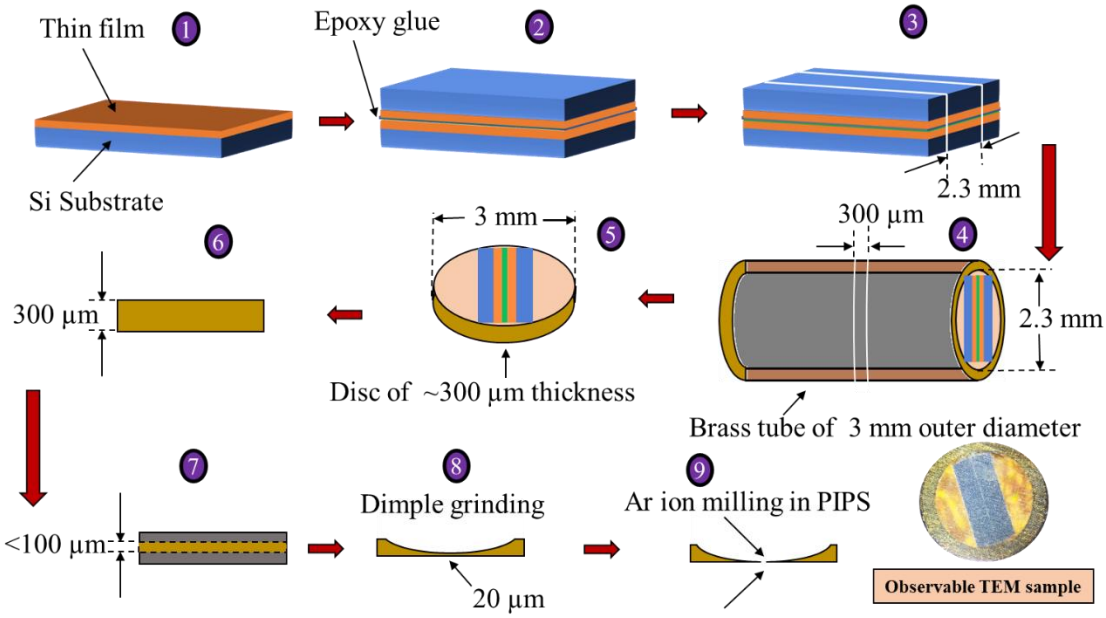

Figure 2.6: Schematic representation of various process to prepare a cross-sectional TEM sample for observing the microstructures in TEM.

This disc is further taken into precession ion polishing system (PIPS) for Ar ion milling. The milling is performed with an ion beam of required energy and an optimized milling angle from both below and above the disc by two ion guns in the dual modulation mode. In our case, we have kept the ion beam energy as 5keV and the milling angle is kept at 4^0. These techniques remove material from the sample's surface, resulting in precise and controlled thinning. All

these process make the specimen suitable for TEM imaging where the sample becomes transparent to the electron beam near to the center of the disc [130]. The schematic representation of the whole process is shown in Figure 2.6.

2.3 Magnetic Characterization:

2.3.1 Magneto-optic Kerr effect (MOKE) magnetometry and microscopy:

Magneto-optic Kerr effect (MOKE) microscopy is a very useful imaging technique used to study magnetic properties and magnetic domain structures in materials. It is based on the magneto-optic Kerr effect, which describes the change in polarization of light reflected from a magnetic material in response to an applied magnetic field [131–135]. MOKE microscopy provides valuable insights into magnetic domain dynamics, magnetization reversal processes, and magnetic anisotropy in a wide range of materials such as thin films, multilayers and nanoparticle ensembles. A linearly polarized light can be thought of as the superposition of two circularly polarized light i.e., left circularly polarized light (LCP) and right circularly polarized light (RCP) with amplitudes $E_L=E_R=E/2$. Hence, the electric field of the LCP light causes the electrons in a sample containing free electrons to move in a left circular motion, while the electric field of the RCP light causes the electrons to move in a right circular motion. This motion of electron around positive charge forms a rotating electric dipole and an attractive force ($F \propto -r$, where r is the radius of electron motion) is felt by the electron towards the positive center to have charge neutrality. By considering equilibrium condition of all forces that act on the electron, the radius of rotating electron can be written as [136,137],

$$r_{R,L} = \frac{\frac{eE}{2m}}{\omega^2 - \omega_0^2} \qquad \ldots\ldots. (2.7)$$

Here, the subscript R and L in the $r_{R,L}$ represents the right and left circular motion of electron. e, m and E represents the charge of the electron, mass of the electron and electric field

associated with the incident polarized light, respectively. ω is the angular frequency and ω_0 ($\sqrt{\frac{k}{m}}$) is constant of the material. Therefore, the displacement vector ($\boldsymbol{D}$) is written as $\boldsymbol{D} = \epsilon\boldsymbol{E}$ = ($\epsilon_0\boldsymbol{E} + \boldsymbol{P}$), here the polarization density is denoted as $\boldsymbol{P}$ that depends on the noumber of dipole moments N per unit volume. ϵ, ϵ_0 being the permittivity of the medium and free space, respectively, the dielectric constant $\epsilon_r(=\epsilon/\epsilon_0)$ is written as [136,137],

$$\epsilon_r = \left(1 + \frac{\frac{Ne^2}{2m\epsilon_0}}{\omega^2 - \omega_0^2}\right) \qquad \ldots\ldots. (2.8)$$

Which leads to the same refractive index ($n_{L,R}$) for the left and right circular polarized light. With the application of a magnetic field to the material, the electron's motion is pushed towards or away (depending on whether the motion is left or right circular) from the circle's center due to the Lorentz force. Thus, the modified radius of left circular and right circular motion becomes.

$$r_{R,L} = \frac{\frac{eE}{2m}}{\omega^2 - \omega_0^2 \mp \frac{\omega Be}{m}} \qquad \ldots\ldots. (2.9)$$

Here, the dipole moment differs due to the difference in radii for the left and right circular motion resulting different dielectric constants. Due to this the velocities of the left and right circularly polarized light becomes different. This phenomenon shows resemblance to the birefringence of circularly polarized light wherein the oppositely polarised light (LCP and RCP) experiences a phase difference of $\Delta\theta$ that is proportional to the difference of refractive index n_L and n_R. Thus, the Lorentz force arising from an applied magnetic field, induces a Kerr rotation (θ_k) which is a result of the rotation of plane of polarization of the reflected light. In case of FM, $\boldsymbol{B}=\mu_0\boldsymbol{M}$ which implies the Kerr rotation (θ_k) represents the magnetization of the sample. If the amplitudes of the reflected LCP and RCP waves are different, the light reflected

from a magnetic medium may also have some ellipticity (ϵ_K) in addition to rotation. As a result, the dielectric constant and the magnetic medium's refractive index become complex parameters. Thus, the dielectric tensor theory, $\boldsymbol{D} = \boldsymbol{\epsilon E}$ (where $\boldsymbol{\epsilon}$ is an antisymmetric tensor), which is derived from Maxwell's equation of electromagnetic wave propagation in a magnetic medium, serves as the basic macroscopic explanation of magneto-optic effects. It can also be written as [132,133,136],

$$\boldsymbol{D} = \boldsymbol{\epsilon}(\boldsymbol{E} + iQ\boldsymbol{m}\times\boldsymbol{E}) \qquad \ldots\ldots. (2.10)$$

Where, Q is a material dependent parameter that represents the strength of the Kerr effect. It is proportional to the saturation magnetization of the sample. The off-diagonal components of the dielectric tensor, which rely on the sample's magnetization, are the primary cause of MOKE. It can be represented as,

$$\boldsymbol{\epsilon}' = \boldsymbol{\epsilon}\begin{pmatrix} 1 & iQ_v m_z & -iQ_v m_y \\ -iQ_v m_z & 1 & iQ_v m_x \\ iQ_v m_y & -iQ_v m_x & 1 \end{pmatrix} \qquad \ldots\ldots. (2.11)$$

where, Q_v represents the Voigt constant and (m_x, m_y, m_z) = m represents the normalized magnetization vector. Second term of equation 2.10 is quite similar to the Lorentz force. Thus, as shown in Figure 2.7 (a), we can obtain the Kerr amplitude (K) by projecting Lorentz movement ($\boldsymbol{v_{LOR}}$) in a plane perpendicular to the propagation direction of the reflected light.

With small angle approximation, the Kerr rotation (θ_k) is represented as $\theta_k = \frac{K}{N}$, where K is the Kerr amplitude and N is the normal amplitude of the reflected and incident polarized light, respectively. Thus, the Kerr rotation becomes opposite for the domains with opposite spontaneous magnetization. One domain will show black contrast if the analyzer entirely blocks the reflected light from that domain, while the oppositely magnetized domain will show white contrast. This method allows for the acquisition of domain contrast in the image plane. The difference in the intensities from the dark and bright domains is represented as, $S = 4\beta KN$,

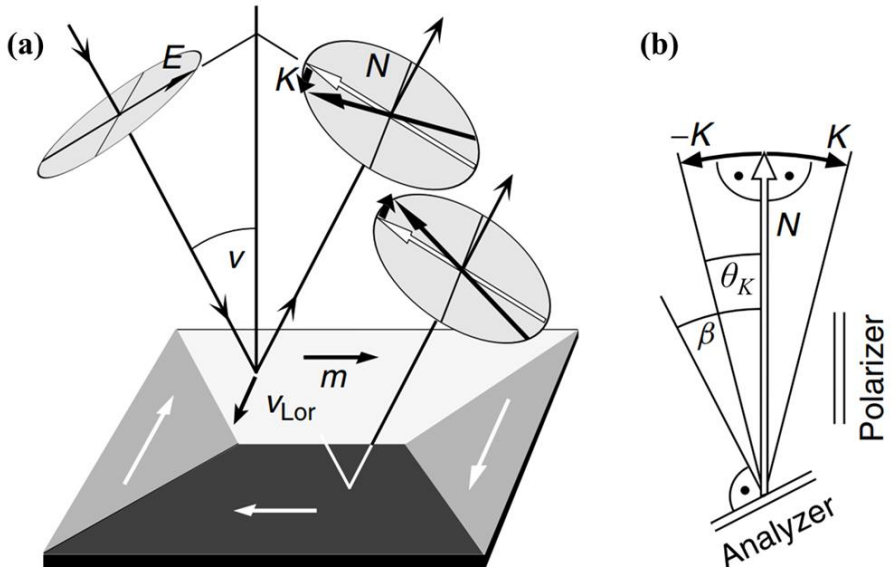

Figure 2.7: (a) Schematic representation of interaction of polarized light with a magnetized sample in longitudional configuration. The Lorentz motion ($\boldsymbol{v_{LOR}}$) of the electrons arising from the interaction of the magnetization of the sample and the electric field of the incident light gives rise to the Kerr amplitude (***K***), (b) shows the orientation of the analyser and polarizer with respect to the Kerr amplitude (***K***) and the normally reflected amplitude (***N***). The schematics are taken with permission from the book Handbook of Magnetism and Advanced Magnetic Materials, (Copyright 2007, John Wiley & Sons, Ltd.) [136].

with β being the angle between the analyser and N (shown in Figure 2.7 (b)). Three types of MOKE geometries are feasible depending on the plane of incidence of the light and the orientation of the magnetization of a sample. All the three configurations have been shown in Figure 2.8. When the sample's magnetization is parallel to the sample surface and plane of incidence of polarized light, this configuration is termed is longitudinal MOKE or L-MOKE. Similar configuration with magnetization being perpendicular to the plane of incidence is known as transverse MOKE or T-MOKE. Further, when the sample's magnetization is parallel to incident plane of the polarised light and perpendicular to the sample surface, is known as the polar MOKE or P-MOKE.

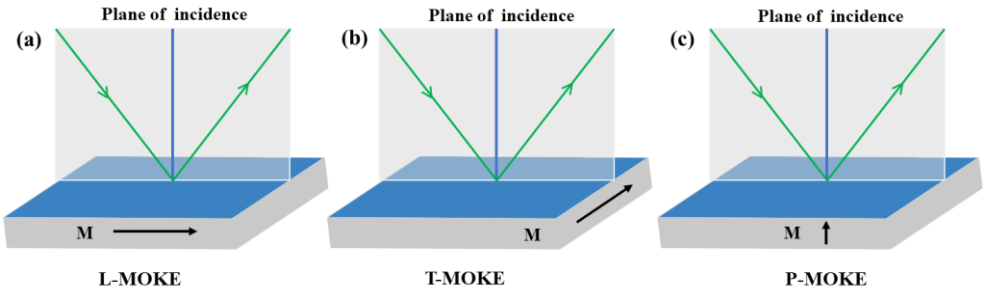

Figure 2.8: Different configurations of the MOKE geometry, (a) L-MOKE, (b) T-MOKE, (c) P-MOKE depending on the direction of the magnetization and the plane of incidence.

The principle of visualizing domain images via Kerr microscopy is explained here with reference to the schematics shown in Figure 2.9 (b). When a linearly polarized light is reflected from a sample surface having domains with opposite spontaneous magnetization, the beam 1 and 2 (as shown in Figure 2.9 (b)) experience equal rotation with opposite direction due to the Kerr effect and gets transformed to elliptically polarized light.

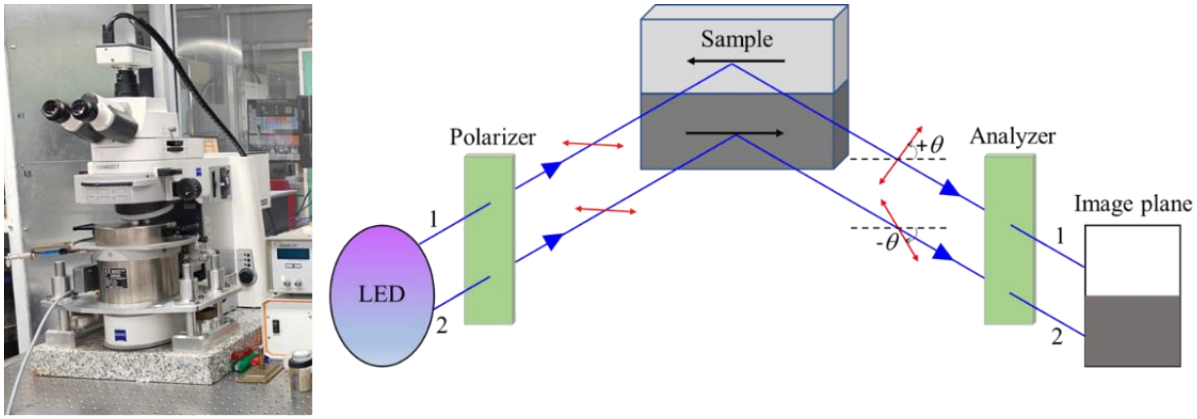

Figure 2.9: (a) MOKE based microscopy available in our lab at NISER, (b) Schematic representation of the MOKE-based microscopy equipment used to produce the domain image.

By using a quarter wave plate before the analyser, this ellipticity obtained by the reflected light is compensated. Further, by adjusting the analyser in a particular orientation, one type of reflected beam is allowed to the image plane that creates a bright contrast and another type of reflected beam is blocked there by creating a dark contrast. Hence, in this manner, Kerr

microscopy can be used to visualize the domain states of the magnetic sample. The reflected photons are further converted to electrons by a charge-coupled device (CCD), creating a digital image of the domains.

The magnetization reversal and domain images of our samples have been studied by the Kerr microscopy manufactured by Evico Magnetics Ltd., Germany. The actual image of the Kerr microscopy available at LNMM, NISER, has been shown in Figure 2.9 (a). It is equipped with eight LED sources which allows to change the sensitivity of the measurement with right combination of LEDs [138]. With an oil immersion objective, a maximum resolution of about 300 nm can be attained. Electromagnetic coils are used to apply a maximum field of 0.9 T in out-of-plane mode, while a maximum field of 1.3 T can be applied in in-plane mode. To prevent the additional heating problem, all of the electromagnetic coils are supplied with proper cooling facility. With a step of 1°, the in-plane sample stage can be rotated from 0 to 360°. Simultaneous observation of magnetic hysteresis loop and domain images are achieved by using the Kerr lab software interfaced with the microscope system.

2.3.2 Superconducting quantum interference device (SQUID) magnetometry:

A Superconducting Quantum Interference Device (SQUID) Vibrating Sample Magnetometer (VSM) is a highly sensitive instrument used to measure very weak magnetic moments (~ 10^{-8} emu) of a material [139,140]. It operates based on the principles of superconductivity and quantum interference, similar to other SQUID-based magnetometers, but with the additional capability of measuring the magnetic response of a vibrating sample. The magnetometer uses a SQUID to achieve this high sensitivity, allowing for extremely accurate magnetic flux measurement. Here, the SQUID is composed of two Josephson junctions that are parallel to one other and have a thin insulator separating the two superconductors. Supercurrents (I_s) are produced when cooper pairs tunnel through the insulating layer from one superconductor to

another. The phase coherence of all cooper pairs within a superconductor allows for the representation of each superconductor in terms of a single wave function. Hence the two superconductors having different phases are represented by two different wave functions. The solution via the Schrödinger equation for these two superconductors gives the expression of supercurrent flowing through the junction, $I_s = I_0 \sin(\varphi_2 - \varphi_1)$, with I_0 being the critical current and $(\varphi_2 - \varphi_1)$ being the phase difference. As the magnetic field can change the phase of a quantum state, the total phase shift is written as,

$$\Delta\varphi B + 2\Delta\varphi(I) = 2\pi n \quad \ldots\ldots. (2.12)$$

Therefore, a change in the magnetic field that is directly related to the flux quantization is the primary cause of the great sensitivity of SQUID. The principle of operation of this SQUID magnetometer is described as follows. The sample is initially placed inside a detecting coil composed of superconducting wires, also referred to as second-order gradiometer coils. The single-turn upper and lower coils are wound in a clockwise direction. On the other hand, the middle coil is wound counter-clockwise and has two turns. Two superconducting magnets are positioned around these coils to create a consistent magnetic field in the sample area. Additionally, the detecting coils are connected to a SQUID that is shielded from outside magnetic fields and maintained well below T_c through liquid helium. By moving the sample vertically up and down, a flux is produced that is detected by the detecting coil and used to measure magnetic properties. The applied magnetic field's effect is neutralized and the magnetic flux resulting solely from the movement of the sample is isolated by the pick-up coil's opposing four turns. Because of the induced flux, a persistent current is consequently produced in the coils. Further, the induced flux is sent to the RF SQUID, which converts it into a voltage signal. The magnetic moment of the sample is then determined by fitting the voltage versus sample position curve with an appropriate model. The output signal versus sample position graph is shown in Figure 2.10 (a). We have performed our measurements by using an MPMS3-

SQUID-VSM manufactured by Quantum Design, USA (see Figure 2.10 (b)) [141]. This has the capability of producing maximum magnetic field ±7T with temperature ranging from 1.8 to 400 K.

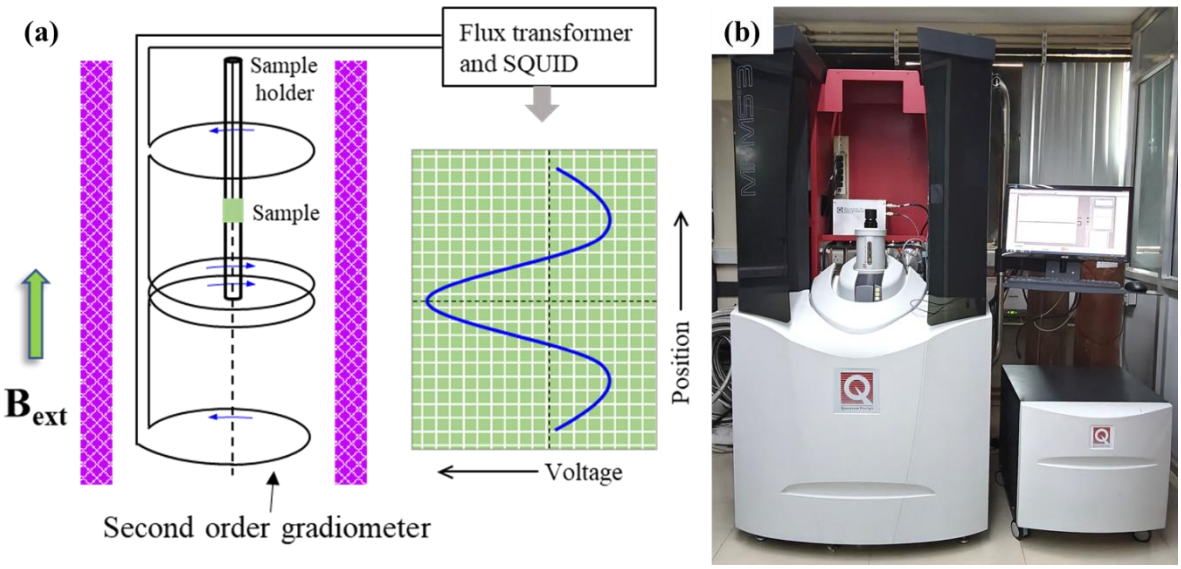

Figure 2.10: (a) A schematic of the detection coil. The plot indicates the voltage vs sample position during the centering process, (b) MPMS3 SQUID-VSM available in our lab at LNMM, NISER.

2.3.3 Magnetic force microscopy (MFM):

One of the most sophisticated techniques for examining surface magnetic characteristics with good resolution and minimal sample preparation is magnetic force microscopy (MFM) [142,143]. A sharp magnetized tip is employed in MFM to scan a magnetic sample. The magnetic interactions between the tip and sample are detected and utilized to rebuild the magnetic structure of the sample surface. Using the magnetic forces operating between the magnetized sample surface and the magnetized tip, MFM can be considered as a promising technique for mapping the magnetic field distributions on a tiny scale. Depending on the distance between the tip and sample surface (ΔD), different types of interactions are possible. These include Van der Walls force (ΔD ~1 nm), electric and magnetic force (ΔD

~0.05-1 μm), and quantum mechanical force (ΔD <1 nm). In order to optimize the impact of stray field interaction between the tip and sample, the MFM scan is conducted at a set lift height. A laser spot is set to be reflected from the top surface of the cantilever due to the change in interaction force between the magnetic tip and sample surface if magnetic textures are present in the sample. This change in force due to magnetostatic interaction and hence the deflection of laser spot is detected by a photo detector. Also, the resonant frequency of the cantilever shows a shift (Δf) due to the interaction which is proportional to the force gradient. Amplitude, phase, and frequency modulation are the three approaches that are used to detect the Δf. Among these, phase modulations are commonly used because of their improved signal-to-noise ratio and decreased artefact effect. The MFM scan results a dark or bright area in the image produced by the detector corresponding to the attractive or repulsive force (see Figure 2.11) [144]. The resonance curve will move to a higher frequency and exhibit an increase in phase shift, or bright contrast, in response to a repulsive magnetic force gradient. On the other hand, a shifts to a lower frequency shows a decrease in phase shift there by providing dark contrast which is the outcome of an attractive magnetic force gradient [145].

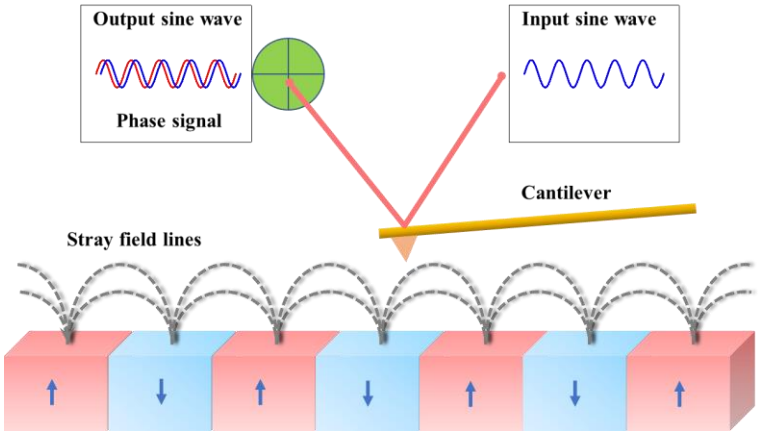

Figure 2.11: Schematic showing the principle of MFM measurement.

In this thesis work, presence of skyrmions have been observed via magnetic force microscopy (MFM) measurements using Attodry 2100 AFM/MFM system manufactured by Attocube, Germany. This has the capability of producing maximum magnetic field ±9T with temperature

ranging from 2 to 300 K. All the measurements have been performed at room temperature using commercially bought MFM tips.

2.3.4 Magneto transport measurement:

In order to understand a sample's electrical properties such as conductivity, resistivity, carrier concentration etc., electric transport and magneto transport measurements are performed. Magneto transport measurement refers to the electric properties of a system measured in presence of magnetic field. These measurements have been performed by a physical properties measurement system (PPMS) (shown in figure 2.12 (a)), manufactured by Quantum design, USA. By performing AC transport (ACT) measurements, the longitudinal resistivity (ρ_{xx}) and transverse resistivity (ρ_{xy}) are determined. Two contacts are made on the two opposite sides of the sample surface through which the AC current is applied uniformly to the sample. The voltage drop across the sample arising due to the applied current is measured using a four probe geometry as shown in the Figure 2.12 (b). The expression for ρ_{xx} and ρ_{xy} can be written as $\rho_{xx} = \frac{V_{xx}}{I} \times \frac{w.t}{L}$ and $\rho_{xy} = \frac{V_{xy}}{I} \times t$, where, V_{xx} and V_{xy} are voltage drops in the longitudinal and transverse directions, respectively [146]. The symbols *I, L, w* and *t,* are the applied current, the distance between two electrodes, width of the sample and the thickness of the thin film, respectively. Typically, van der Pauw geometry is employed to measure the transverse Hall resistivity of the sample [147,148]. To identify the pure Hall signal in this instance, the voltage adjustments must be perpendicular to the direction of current flow and opposite to one another around the perimeter. It is quite challenging to align voltage probes with such precession, because misalignment of the probes can introduce a magnetoresistance signal into the Hall resistivity. To solve the issue, a five-probe strategy is employed along with an extra voltage probe (See Figure 2.12 (c)) [149]. In this manner, a potentiometer placed between the two

probes neutralizes the excess voltage prior to the measurements at zero magnetic field. The magnetoresistance signal in the Hall measurements is much reduced using this technique.

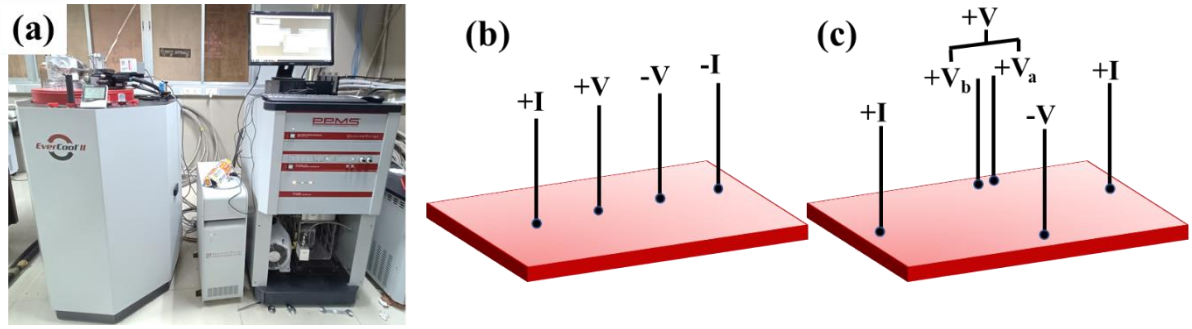

Figure 2.12: Physical property measurement system (PPMS) available at NISER, (b) longitudinal transport measurement in four probe geometry, (c) transverse transport measurement in five probe geometry.

Both AC and DC mode transport measurements can be performed in this PPMS which has the capability of applying magnetic field in the range ±9T and temperature in the range of 1.8-350K. However, all our measurements have been performed in the AC transport (ACT) mode which provides a better signal filtering process. Also, it reduces the DC offset, noise, and instrumental drift in the measurement. During the measurement, an AC current of 500 μA with 17 Hz frequency was applied to the sample. Wire bonder is used to make the contacts between the sample and the sample holder.

2.3.5 Ferromagnetic resonance (FMR) spectroscopy:

"Ferromagnetic resonance (FMR)" refers to the resonance phenomenon with the spin wave in ferromagnetic materials [99]. To investigate the dynamics of magnetization in a magnetic system, FMR is usually employed. The magnetic thin film is subjected to a magnetic field (H) in order to determine resonance where each ferromagnet's (FM) spin begins to precess at the Larmor frequency. The precession frequency υ is proportional to the applied magnetic field H. This technique is useful in determining various properties of FM material such as, magnetic

anisotropy, Gilbert damping, gyromagnetic ratio, etc. The operational principle of the FMR is described as follows. High-frequency electromagnetic waves (RF signals in the GHz range) are transmitted in FMR using a coplanar waveguide (CPW) at one end and this transmitted signal is received at the other end [150]. The signal that is incident and that is transmitted will be equal in the absence of any microwave power loss. However, joints, materials, and other factors always result in some dielectric losses which is well calibrated in the FMR set up.

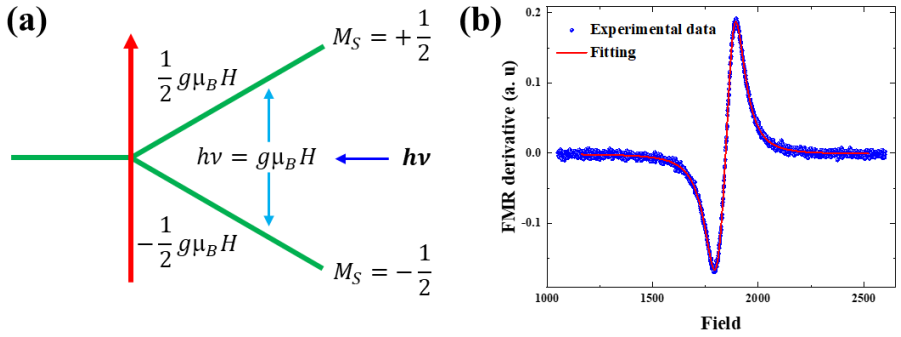

Figure 2.13: (a) Schematic representation of Zeeman splitting under applied magnetic field. (b) Typical plot of FMR derivative and its Lorentzian fitting is shown as a function of magnetic field.

If an FM material is kept on the top of the CPW line, there will be a finite loss in the microwave signal based on the microwave absorption capacity of the FM. Further by applying a DC magnetic field, the spins try to align themselves along the direction of the applied magnetic field (H) following a precessional motion. This frequency of precession or Larmor frequency (υ) happens in the GHz range and depends on the magnetic field. During the FMR measurement, between the two parameters i.e., frequency and magnetic field, one parameter is kept constant and other parameter is allowed to vary in a certain range. In the case when the magnetic field varies in a wide range by keeping the frequency constant, resonance occurs at the matching point of microwave frequency and precession frequency. At this resonance, a sudden decrease in the transmitted spectra happens due to the abrupt rise in the absorption of microwave power by the sample.

Zeeman splitting provides a macroscopic understanding of this FMR mechanism. The Zeeman energy levels split into two levels with energy $\pm\frac{1}{2}g\mu_B H_{res}$ when a magnetic field is introduced and leads to an energy gap of $g\mu_B H_{res}$. Here, g is the Lande g factor, H_{res} is the magnetic field at which resonance occurs and μ_B is Bohr magnetron. Applying an electromagnetic radiation of specific frequency (radio frequency field h_{rf}) causes the FM material to absorb energy $h\upsilon$ and enter an excited state. The microwave's energy at resonance is equal to the separation of the Zeeman energy level. Hence, we get $h\upsilon = g\mu_B H_{res}$. The splitting of Zeeman levels is shown in Figure 2.13 (a). The value of H_{res} and ΔH (FWHM) can be extracted from the transmitted spectrum shown in Figure 2.13 (b), by using the following Lorentzian function [151],

$$\frac{dP}{dH} = A\frac{4\Delta H(H-H_{res})}{[4(H-H_{res})^2+(\Delta H)^2]} - S\frac{(\Delta H)^2-4(H-H_{res})^2}{[4(H-H_{res})^2+(\Delta H)^2]} + offset \quad \ldots\ldots (2.13)$$

Here, A and S are anti-symmetric and symmetric coefficients, respectively. Several magnetic properties, including the gyromagnetic ratio, anisotropy, and Gilbert damping constant, can be calculated by analysing these extracted values. FMR spectra are obtained for a range of microwave frequency values in order to determine the damping constant. The values of ΔH and H_{res} are obtained for every FMR spectra. To get the value of gyromagnetic ratio (γ), the υ vs H_{res} plot is fitted using the Kittel equation,

$$\omega = \gamma\mu_0\sqrt{(H_{ext}+H_k)(H_{ext}+H_k+M_s)} \quad \ldots\ldots (2.14)$$

This γ value is used further to get the damping value of the FM layer by fitting the following linear equation,

$$\Delta H = \Delta H_0 + \frac{4\pi\alpha f}{\gamma} \quad \ldots\ldots (2.15)$$

The slope here gives the damping value α. In this thesis work, we have used a lock-in based FMR set up to perform the FMR measurements. The picture of the set up available in our lab is shown is Figure 2.14. The different components of this set up are,

i) Coplanar waveguide (CPW): through which the RF signal is sent

ii) Electromagnets: the DC magnetic field is produced using this

iii) RF signal generator: the radio frequency (RF) signal is generated through this

iv) Helmholtz coil: It modulates the generated signal.

v) Diode Detector: The transmitted signal is detected by the detector.

vi) Lock-in-Amp: for better signal to noise ratio and to lock the detecting signal.

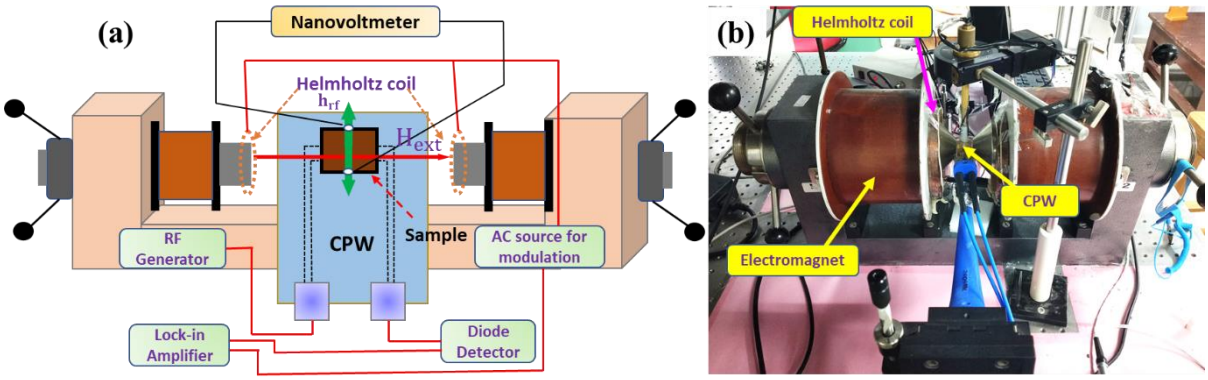

Figure 2.14: (a) Schematic of the FMR set-up based on the CPW, (b) Picture of the FMR set-up available in our lab at LNMM, NISER.

As mentioned earlier, the set-up can be operated in two different modes. One is the constant frequency mode where the DC magnetic field is swept at a constant frequency. The other is constant field mode where the rf frequency is swept by keeping the field value fixed. In our set up the magnetic field value varies in the range ±5 KOe and the RF frequency can be varied from 2 to 17 GHz.

Chapter 3

Stabilization of synthetic antiferromagnetic structure in Pt/Co PMA system with Ru spacer:

The quest for efficient and stable magnetic structures is a fundamental pursuit in the field of spintronics, which can be used for data storage, sensing, and computing technologies. In recent times, artificially engineered layered magnetic structures have drawn considerable attention due to their potential in various spintronic applications. Synthetic antiferromagnetic (SAF) structures, composed of two or more ferromagnetic layers separated by non-magnetic (NM) spacer layer having antiparallel alignment of magnetization among the consecutive FM layers, have garnered considerable attention due to their potential for high thermal stability and reduced susceptibility to external magnetic perturbations [152,153]. The FM layers are coupled by RKKY type interlayer exchange coupling (IEC) [154–157]. This coupling is of oscillatory nature and decays with the NM layer thickness [158–160]. Therefore, in a FM/NM/FM system, global FM or AFM behaviour is seen depending on the thickness of the spacer. Appropriate choice of FM layer as well as NM spacer material is the key part of these SAFs for desired application purpose. Ru, Ir, Rh etc., are some of the widely used spacer materials for SAF providing strong AFM coupling between the FM layers as well as easy manipulation of antiferromagnetic order by varying the spacer layer thickness [161]. Along with achieving the AFM coupling among the FM layers, it is also crucial to have stable perpendicular magnetic anisotropy (PMA) in the FM layers. PMA results in higher thermal stability compared to in-plane magnetization [162–165]. This stability is crucial for maintaining the desired magnetic state at elevated temperatures. This can lead to a reliable device operation over a wider temperature range avoiding disturbances due to thermal fluctuations [166,167]. By utilizing SAFs with PMA in magnetic tunnel junctions (MTJs) or spin valves, one can achieve increased data storage capacity and faster read/write

operations [163,168–171]. Further, as discussed in the introduction section, SAFs also possess its promise towards achieving reduced skyrmion Hall effect (SkHE) for skyrmionic applications [172–174]. In this regard, first we wanted to achieve a stable SAF phase in our system which can be optimized for further application purpose. Previously it is reported that, Ru spacers with less thickness promote stronger coupling between the adjacent FM layers, leading to a more pronounced antiferromagnetic alignment [167,175–178]. On the other hand, increasing the thickness of the Ru spacer reduces the coupling strength, allowing for the manipulation of magnetic states and domain configurations within the SAF structure. In this context, we have considered a system of Pt/Co with Ru as spacer layer between two FM Co layers. Here, we have tuned the Co thickness for achieving PMA as well as the Ru thickness in a wide range for having strong AFM coupling among the Co layers.

3.1 Sample details:

The samples have been prepared on a Si substrate with 100nm thick SiO_2 layer. The sample structure is Si/SiO_2/Ta(3)/Pt(3.5)/Co(t_{Co})/Ru(t_{Ru})/Co(t_{Co})/Pt(3.5). Numbers in the parenthesis indicate the thicknesses in nm. Two series of samples have been prepared by considering Co thickness as 0.8 nm and 1.0 nm which are named as series 1 and series 2, respectively. In both the series, t_{Ru} is varied from 0.4 nm to 1.4 nm with a difference of 0.1 nm. A schematic of the sample structures have been shown in Figure 3.1. All the samples of series 1 and series 2 have been named as S1-t_{Ru} and S2- $t_{Ru,}$ respectively, where, t_{Ru} represents the thickness of the Ru spacer layer for that particular sample. A seed layer of Ta is grown on the substrate which favours the growth of the Pt layer to have PMA in the Co layer. Pt is employed as a capping layer in all samples to protect the Co layer from oxidation. All the samples have been prepared in a high-vacuum multi-deposition chamber manufactured by Mantis Deposition Ltd., UK. The base pressure of the chamber was < 1×10^{-7} mbar. The deposition pressure was ~ 2.9×10^{-3} mbar for Ta layer and ~ 1.5×10^{-3} for Pt, Co and Ru layers. The substrate table was rotated at 15 rpm

during sample preparation. The rates of deposition were 0.1 Å/s, 0.13 Å/s, 0.3 Å/s and 0.1 Å/s for Co, Ta, Pt and Ru, respectively.

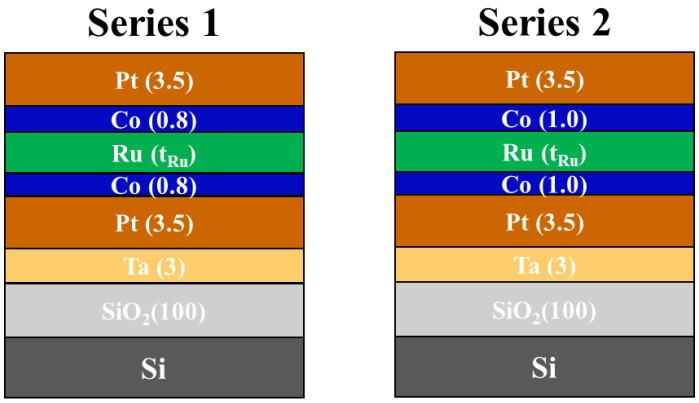

Figure 3.1: Schematics of the sample structure with Ru spacer for Series 1 and Series 2.

3.2 Structural characterization:

We have performed cross-sectional transmission electron microscopy (TEM) imaging of the sample Si/SiO_2/Ta(3)/Pt(3.5)/Co(0.8)/Ru(1.2)/Co(0.8)/Pt(3.5) (shown in Figure 3.2) in a high-resolution TEM (HRTEM) (JEOL F200, operating at 200 kV and equipped with a GATAN oneview CMOS camera) for the structural characterization of these ultrathin layers. From TEM image, the thicknesses of the layers Ta, Pt, Co/Ru/Co, Pt are found to be 2.8, 3.5, 2.8, 3.5 nm, respectively, which matches with the calibrated thicknesses from sputtering by quartz crystal microbalance (QCM).

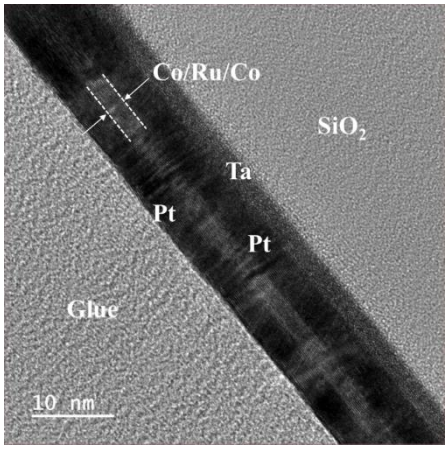

Figure 3.2: Cross-sectional TEM image of sample Si/SiO_2/Ta(3)/Pt(3.5) /Co(0.8)/Ru(1.2)/Co(0.8)/Pt(3.5) from Series 1.

3.3 Magnetic characterization:

The magnetic hysteresis loops of all the samples have been measured at room temperature by SQUID-VSM (Superconducting Quantum Interference Device-Vibrating sample magnetometer) manufactured by Quantum Design, USA. Figure 3.3 shows the hysteresis loops for the samples of both the series with Ru thickness as 0.6nm, 1.0nm and 1.4nm, respectively.

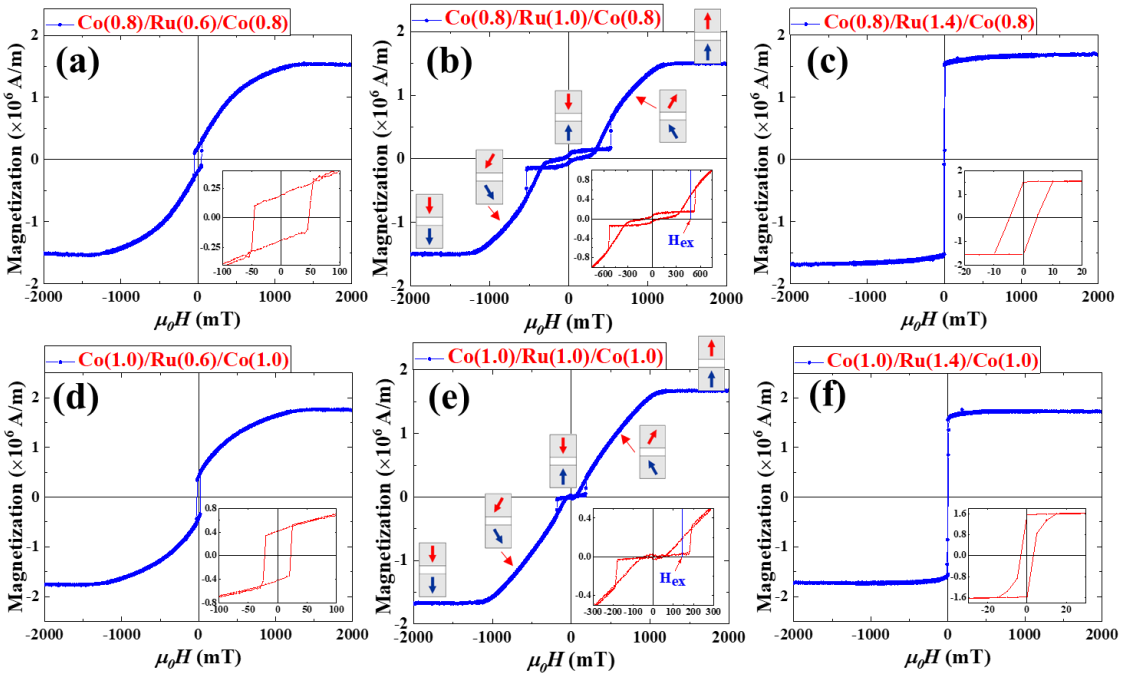

Figure 3.3: Magnetization reversal of the samples (a) S1-0.6, (b) S1-1.0 and (c) S1-1.4 from Series 1 and of the samples (d) S2-0.6, (e) S2-1.0 and (f) S2-1.4 from the Series 2. The schematic arrows shown in the plot (b) and (e) indicates the possible configuration of magnetic moments of the FM layers below and above the Ru spacer layer.

From the hysteresis loop it is evident that the samples with t_{Ru}=0.6nm, show a usual ferromagnetic (FM) hysteresis loop with single-step reversal happening at a negative magnetic field. This indicates the coupling between the two Co layers to be ferromagnetic. However, for samples with t_{Ru}=1.0nm, a two-step hysteresis loop is observed with reversal starting from the positive side. This step-like reversal which can be considered as a signature of the AFM

coupling between the FM layers, can be explained as follows with reference to the hysteresis loop in Figure 3.3 (b). At an applied magnetic field leading to positive saturation, the Zeeman energy becomes dominant and the magnetic moments of both the FM layers align in the direction of applied field. While reducing the magnetic field from positive saturation, due to strong interlayer exchange coupling (IEC), the moments in each layer start rotating in opposite directions with a deviation from the perpendicular easy axis. The steep-like or slope-type behaviour in the hysteresis loop here is indicative of the relatively canted state of magnetization of both layers at this point. By reducing the field even more, the magnetizations in both layers go through a nucleation propagation event, become antiparallel, and align with the easy axis of magnetic anisotropy that is perpendicular to the film plane. This minimizes the energy of both anisotropy and AFM-IEC at the expense of Zeeman contribution. Here, the remanence becomes near to zero which accounts for the direction of magnetic moments in both the FM layers below and above the Ru spacer to be oppositely aligned to each other thereby reducing the overall moment. By further reducing the magnetic field, the magnetic moment of both the Co layers align in the direction of applied field leading to the negative saturation. Here, the coupling between both layers is lost. Further, at t_{Ru}=1.4nm, the hysteresis loop again shows a FM type magnetization reversal which may be due to the appearance of FM coupling again at this thickness regime of Ru spacer. This behaviour accounts for the oscillatory behaviour of the RKKY interaction with the variation of spacer layer thickness. The strength of the exchange coupling for the AF coupled samples can be quantified with the exchange constant $J_{ex} = H_{ex}M_s t$ [171], where H_{ex} is the is the exchange coupling field at which the AFM coupling between the FM layers vanishes and the magnetization directions in both the layers try to become parallel with the applied field. M_s is the saturation magnetization and t is the thickness of FM layer. H_{ex} can be calculated from the hysteresis loop of the AFM coupled samples measured by SQUID-VSM as shown in Figure 3 (b) and (e) [179]. However, the calculation

of H_{ex} for the FM-coupled samples is not trivial since the magnetizations of the layers are already parallel coupled. In the case of parallel coupled layers, the determination of H_{ex} can be done using dynamic techniques like ferromagnetic resonance [180]. Since we have not calculated the coupling strength for the FM coupled samples, the values have not been plotted in the J_{ex} vs t_{Ru} plot in Figure 3.4 (a) and (b) and only the values pertaining to the AFM coupled samples have been shown. All the calculated values of H_{ex}, M_s and J_{ex} for the AFM coupled samples of both the series 1 and 2 have been mentioned in table 3.1.

Table 3.1: calculated values of H_{ex}, M_s and J_{ex} for the AFM coupled samples of both the series 1 and 2.

Sample name	**H_{ex} (mT)**	**M_s ($\times 10^6$A/m)**	**J_{ex} ($\times 10^{-4}$J/m^2)**	**Coupling type**	**Sample name**	**H_{ex} (mT)**	**M_s ($\times 10^6$A/m)**	**J_{ex} ($\times 10^{-4}$J/m^2)**	**Coupling type**
S1-0.4	-	-	-	**FM**	S2-0.4	-	-	-	**FM**
S1-0.5	-	-	-	**FM**	S2-0.5	-	-	-	**FM**
S1-0.6	-	-	-	**FM**	S2-0.6	-	-	-	**FM**
S1-0.7	130	1.535	1.59	**AFM**	S2-0.7	-	-	-	**FM**
S1-0.8	375	1.388	4.16	**AFM**	S2-0.8	-	-	-	**FM**
S1-0.9	460	1.417	5.21	**AFM**	S2-0.9	124	1.466	1.81	**AFM**
S1-1.0	478	1.498	5.72	**AFM**	S2-1.0	148	1.675	2.47	**AFM**
S1-1.1	234	1.621	3.03	**AFM**	S2-1.1	81	1.743	1.41	**AFM**
S1-1.2	69	1.669	0.92	**AFM**	S2-1.2	-	-	-	**FM**
S1-1.3	-	-	-	**FM**	S2-1.3	-	-	-	**FM**
S1-1.4	-	-	-	**FM**	S2-1.4	-	-	-	**FM**

The samples with 0.8nm (Series 1) Co thickness show stronger AFM coupling strength as compared to the samples with 1.0nm Co thickness (Series 2). This can be attributed to the higher anisotropy for the samples with lower Co thickness (Series 1) as compared to the samples of Series 2. Also, Series 1 shows a wide range of AFM coupling with the variation of Ru thickness ranging from 0.7-1.2nm. Whereas, Series 2 shows AFM coupling in a comparatively smaller range of Ru spacer variation ranging from 0.9-1.1nm.

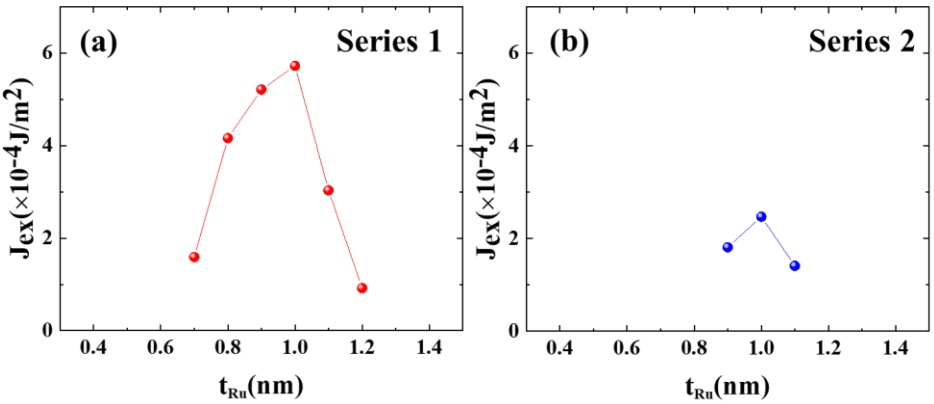

Figure 3.4: Plot of the interlayer exchange coupling energy with the variation of Ru spacer thickness ranging from 0.4nm to 1.4nm for (a) Series 1 and (b) Series 2.

In Summary, we have Prepared SAF samples with PMA by considering Ru as a spacer layer between the two Co layers. Samples with lower Co thickness i.e. 0.8 nm show a larger antiferromagnetic coupling plateau than the samples with Co thickness 1.0 nm. Studying the domain behaviour in these SAF samples would be interesting. However, due to limitation of applying a maximum perpendicular magnetic field of 0.9 T in our magneto-optic Kerr effect (MOKE) microscopy, which is lower than the saturation magnetic field of our SAF samples, we could not explore the behaviour of magnetic domains in these samples via Kerr microscopy. Further, we have considered the Co thickness as 0.8 nm in our following work due to the wide range of AFM coupling with the variation of the spacer layer as well as due to the stronger coupling. However, due to a few limitations in the measurement, we have considered Ir as a spacer layer in all the next chapters.

Chapter 4

Magnetization reversal and domain structures in perpendicularly magnetized Pt/Co system with Ir as a spacer layer:

In the previous chapter (i.e., chapter 3) we have discussed about the SAF structure comprising of Pt/Co perpendicular magnetic anisotropic (PMA) system with Ru as the non-magnetic spacer layer between the two ferromagnetic (FM) layers i.e., Co. However, Ir can also be a good candidate for non-magnetic (NM) spacer layer in the SAF with its advantage of having strong antiferromagnetic interlayer exchange coupling (AFM-IEC) as well as provide better tunability for hosting skyrmions in the FM layer by manipulating the Dzyaloshinskii–Moriya interaction (DMI) in the system [154,155,157,181,182]. Gabor *et. al.*, have shown a strong AFM-IEC in a Pt/Co PMA system with Ir spacer [179]. Yakushiji *et. al.,* have observed large coupling in a similar Pt/Co system with Ir spacer along with a high magnetoresistance ratio in the magnetic tunnel junction (MTJ) stack consisting of this PMA-SAF [183]. Further, Dohi *et. al.,* have studied the current induced motion of skyrmions in a SAF system of Co/CoFeB multilayers with Ir spacer [173]. There are several other works where Ir has been a promising material to be used as a spacer layer in the SAF for various applications [184–186]. In this context, we have fabricated SAF samples by taking Co as FM layer and Ir as NM spacer layer. Through this work, we aim to study the magnetization reversal as well as domain structures in these SAF multilayer systems. From the previous work, we have considered the Co thickness to be 0.8nm to have PMA as well as to have a wide range of AFM coupling with the variation of spacer layer. By varying the Ir thickness between the two Co layers as 1.0nm, 1.5nm and 2.0nm, we have observed three different types of spin configuration during the magnetization reversal such as, FM coupling, AFM coupling and canted magnetic configuration, respectively [130].

4.1 Sample details:

Nine samples have been prepared on rigid Si (100) substrates with sample structure Si/Ta(3)/[Pt(3.5)/Co(0.8)]$_m$/Ir(t_{Ir})/[Co(0.8)/Pt(3.5)]$_n$ along with a reference sample (R1) of Si/Ta(3)/[Pt(3.5)/Co(0.8)]$_2$/ Ta(3). All the thicknesses shown in the parentheses are in nm. In the sample structure, the number of stacking of [Pt/Co] layers below and above the Ir spacer, i.e., (m, n), are (2, 1) and (1, 1), respectively, for t_{Ir} = 1.0, 1.5, and 2.0 nm. We name these six samples as S-2-1.0-1, S-2-1.5-1, S-2-2.0-1, S-1-1.0-1, S-1-1.5-1 and S-1-2.0-1. Another two samples with t_{Ir} = 1.5 nm and (m, n) as (1, 2) and (2, 2) are named S-1-1.5-2 and S-2-1.5-2, respectively. The sample names and their structures are listed in Table 4.1. A schematic of the sample structure is shown in Figure 4.1 (a). A seed layer of Ta is grown on the substrate. It favours the growth of the Pt layer to provide PMA in the Co layer. In all the samples (except reference one), Pt is used as a capping layer to prevent oxidation of the Co layer.

Table 4.1: Sample names and corresponding layer structures.

Sample	**Structure**	**(m, n)**
R1	Si/Ta(3)/[Pt(3.5)/Co(0.8)]$_2$/Ta(3)	
S-2-1.0-1	Si/SiO$_2$/Ta(3)/[Pt(3.5)/Co(0.8)]$_2$/Ir(1.0)/[Co(0.8)/Pt(3.5)]	2, 1
S-2-1.5-1	Si/SiO$_2$/Ta(3)/[Pt(3.5)/Co(0.8)]$_2$/Ir(1.5)/[Co(0.8)/Pt(3.5)]	2, 1
S-2-2.0-1	Si/SiO$_2$/Ta(3)/[Pt(3.5)/Co(0.8)]$_2$/Ir(2.0)/[Co(0.8)/Pt(3.5)]	2, 1
S-1-1.0-1	Si/SiO$_2$/Ta(3)/[Pt(3.5)/Co(0.8)]/Ir(1.0)/[Co(0.8)/Pt(3.5)]	1, 1
S-1-1.5-1	Si/SiO$_2$/Ta(3)/[Pt(3.5)/Co(0.8)]/Ir(1.5)/[Co(0.8)/Pt(3.5)]	1, 1
S-1-2.0-1	Si/SiO$_2$/Ta(3)/[Pt(3.5)/Co(0.8)]/Ir(2.0)/[Co(0.8)/Pt(3.5)]	1, 1
S-1-1.5-2	Si/SiO$_2$/Ta(3)/[Pt(3.5)/Co(0.8)]/Ir(1.5)/[Co(0.8)/Pt(3.5)]$_2$	1, 2
S-2-1.5-2	Si/SiO$_2$/Ta(3)/[Pt(3.5)/Co(0.8)]$_2$/Ir(1.5)/[Co(0.8)/Pt(3.5)]$_2$	2, 2

All the samples have been prepared in a high-vacuum multi-deposition chamber manufactured by Mantis Deposition Ltd., UK. The base pressure of the chamber was < 1×10^{-7} mbar. The deposition pressure was ~1.5×10^{-3} mbar for Ta and Pt layers. Furthermore, for Co and Ir, the

deposition pressures were ~5×10^{-3} mbar and ~2.1×10^{-3} mbar, respectively. During sample preparation, the substrate table was rotated at 15 rpm to minimize the growth-induced anisotropy and also to have uniform growth of the films. The rates of deposition were 0.1 Å/s, 0.13 Å/s, 0.3 Å/s and 0.1 Å/s for Ir, Ta, Pt and Co, respectively.

4.2 Structural characterization:

For the structural characterization of these ultrathin layers, we have performed cross-sectional TEM imaging in a high-resolution transmission electron microscope (HRTEM) (JEOL F200, operating at 200 kV and equipped with a GATAN oneview CMOS camera) in the STEM mode. Figure 4.1 (b) shows the high-resolution STEM images of sample S-2-1.5-1. The growth of individual layers is clearly visible (indicated in the image with respective layer names).

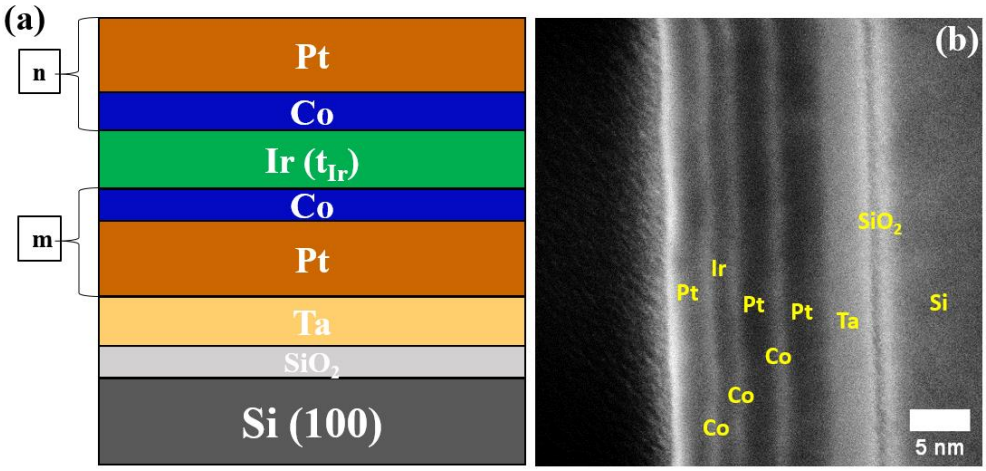

Figure 4.1: (a) Schematic of the sample structure. (b) Cross-sectional STEM image of sample S-2-1.5-1.

4.3 Magnetic characterization:

For quantifying the IEC energy and anisotropy energy, etc., we have performed the hysteresis measurements of all the samples at room temperature using a SQUID-VSM (Superconducting Quantum Interference Device-Vibrating sample magnetometer) manufactured by Quantum Design, USA.

Hysteresis loop of the reference sample R1 measured by SQUID-VSM in the presence of an out-of-plane applied magnetic field is shown in Figure 4.2 (a). This shows a sharp reversal indicating PMA in the sample. Samples S-2-1.0-1 and S-1-1.0-1, with t_{Ir} = 1.0 nm, show FM coupling indicating that this thickness of Ir is not in the AFM coupling regime. M-H loops corresponding to these samples have been shown in Figure 4.2 (b) and (c).

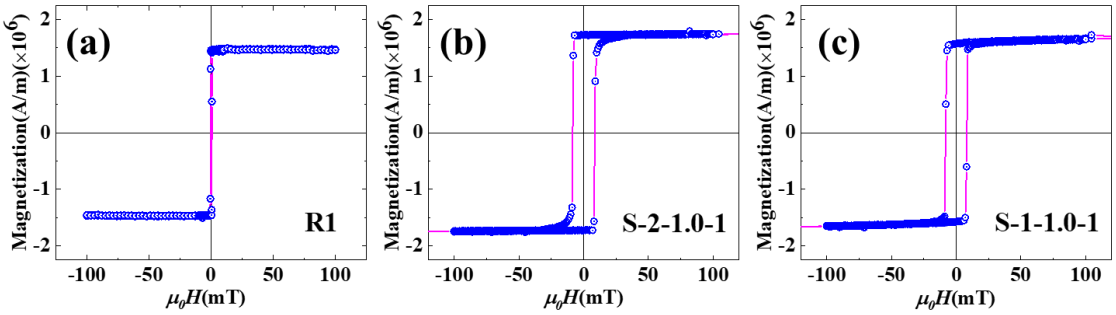

Figure 4.2: Hysteresis loop measured by SQUID-VSM for samples (a) R1, (b) S-2-1.0-1, (c) S-1-1.0-1. The magnetic field was applied perpendicular to the film plane.

Magnetic hysteresis loops of samples S-2-1.5-1 and S-1-1.5-1 are shown in Figure 4.3 (a) and (b), respectively, measured by SQUID-VSM. The steps in the hysteresis loops indicate AFM coupling between the FM layers below and above the Ir spacer layer.

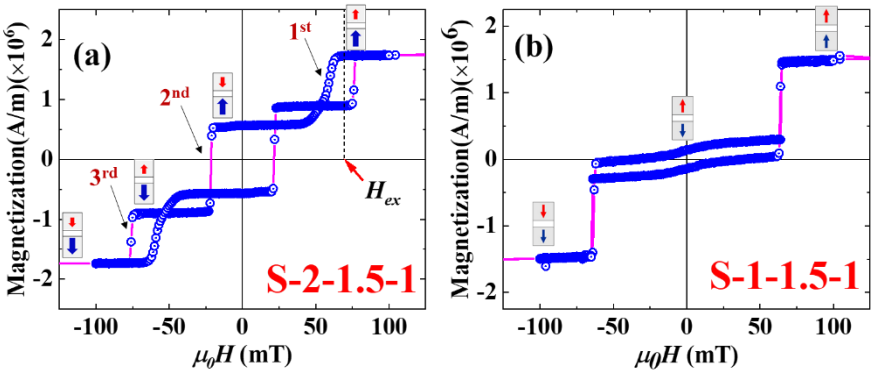

Figure 4.3: Hysteresis loop measured by SQUID-VSM for samples (a) S-2-1.5-1 and (b) S-1-1.5-1. The magnetic field was applied perpendicular to the film plane.

Figure 4.3 (a) shows that the magnetization reversal is accompanied by three steps in the hysteresis loop. Here, the two Co layers below the Ir spacer layer behave such that they are coupled ferromagnetically and reverse simultaneously during the magnetic field sweep. However, the Co layer above the Ir layer reverses separately [187]. The magnetization reversal may be explained in the following manner. In the first reversal the top FM layer switches first and becomes AFM coupled to the bottom FM layers. In the second reversal, both the top and bottom FM units switch oppositely because of strong AFM coupling. Finally, under sufficiently negative external field (Zeeman energy), the top layer switches along the negative field direction, and hence saturation is achieved. For sample S-1-1.5-1, there are only two reversals, indicating that in the first reversal, both layers become AFM coupled, and in the second reversal, the coupling is lost and both FM layers become negatively saturated. Furthermore, we observe in Figure 4.3 (a) that there is a substantial remanent magnetization in the sample indicating that S-2-1.5-1 is an uncompensated SAF, but in Figure 4.3 (b), the remanence is almost close to zero, which indicates that S-1-1.5-1 is a compensated SAF. The other two samples, S-1-1.5-2 and S- 2-1.5-2, also show the AFM coupling between the FM layers. The IEC energy of these AFM coupled FM layers can be calculated by using the expression $J_{ex} = H_{ex}M_s t$, where H_{ex} is the exchange coupling field (shown in Figure 4.3 (a)) at which the coupling between the FM layer vanishes and the magnetization directions in both the layers become parallel [179,183]. M_s is the saturation magnetization and t is the thickness of the FM layers [178]. H_{ex} can be calculated from the hysteresis loop measured by SQUID-VSM as indicated in Figure 4.3 (a). The IEC energy (J_{ex}) of AFM coupled samples S-2-1.5-1, S-1-1.5-1, S-1-1.5-2 and S-2-1.5- 2 is found to be 2.96×10^{-4}, 1.64×10^{-4}, 2.74×10^{-4} and 4.56×10^{-4} J/m^2, respectively. Here, it shows an increase in the coupling strength with the increase in the number of Co/Pt layers indicating that it needs more energy to break the coupling for more Co/Pt layers below and above the spacer. The other two samples, S- 2-2.0-1 and S-1-2.0-1, with t_{Ir} = 2.0

nm, show a bow-tie shape hysteresis loop (shown in Figure 5.2 of chapter 5) with no steps. This indicates that the AFM coupling is reduced at this Ir thickness.

Table 4.2: Anisotropy energy calculation for all the samples from the SQUID data.

Sample name	Saturation Magnetization(M*s*) in A/m	Anisotropy field (H_k) in mT	Anisotropy energy (K_{eff}) in $J/m3$
S-2-1.0-1	1.75×10^6	969	8.47×10^5
S-2-1.5-1	1.75×10^6	1100	9.62×10^5
S-2-2.0-1	1.78×10^6	837	7.44×10^5
S-1-1.0-1	1.74×10^6	781	6.79×10^5
S-1-1.5-1	1.59×10^6	1138	9.04×10^5
S-1-2.0-1	1.76×10^6	631	5.55×10^5
S-1-1.5-2	1.64×10^6	1183	9.70×10^5
S-2-1.5-2	1.78×10^6	1302	1.15×10^6

The effective anisotropy energy values for all the samples have been evaluated by measuring the hysteresis loops along both in-plane and out-of-plane directions of the samples in the SQUID magnetometer. In this context, we have used the relation $K_{eff} = H_k M_s/2$, where H_k is the anisotropy field (in-plane saturation field) and *Ms* is the saturation magnetization. The corresponding values along with the anisotropy energy have been mentioned in Table 4.2.

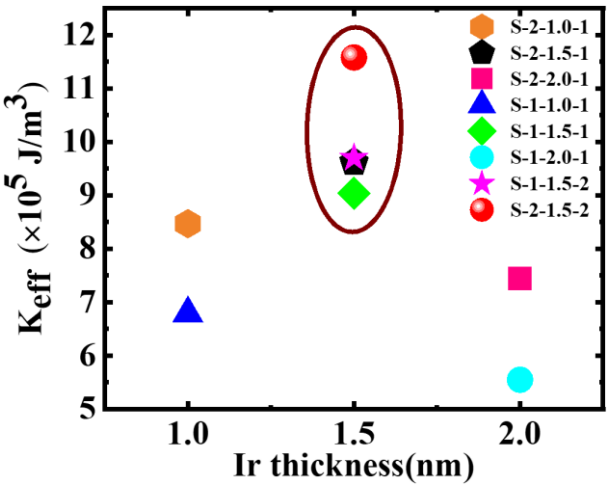

Figure 4.4: Effective anisotropy energy density calculated for the samples with Ir spacer.

We found an enhancement in the anisotropy energy of the samples with AFM coupling compared to the samples with FM coupling. The comparison of anisotropy energies of these samples are shown in Figure 4.4, where the points inside the ellipse show the effective anisotropy energy values for the SAF samples. The anisotropy energy of the samples are higher

than the IEC energy (J_{ex}=t) resulting in a smaller intermediate angle between the magnetic moments of the two layers [167,187].

Simultaneous observations of magnetic domain images and qualitative hysteresis loop in polar mode have been performed for all the samples with the help of a magneto-optic Kerr effect (MOKE)-based microscope manufactured by Evico magnetics GmbH, Germany. Hysteresis loops with sharp reversal (similar to that obtained via SQUID-VSM measurement) have been observed for the samples S-2-1.0-1 and S-1-1.0-1 with Ir thickness 1.0nm. The images captured by the MOKE microscopy show big bubble domains during the magnetization reversal (Shown in Figure 4.5).

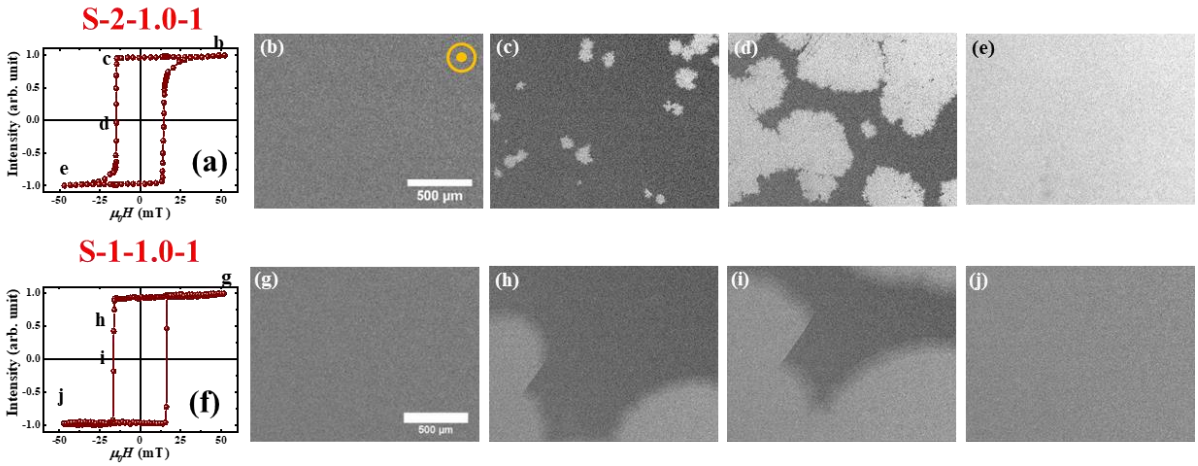

Figure 4.5: Hysteresis loops and domain images of the FM-coupled samples S-2-1.0-1 and S-1-1.0-1, measured via MOKE microscopy.

However, for the AFM coupled samples, the behaviour of the domains changes. Figure 4.6 shows the hysteresis loops and the corresponding domain images measured by MOKE microscopy in polar mode for the AFM coupled samples S-2-1.5-1, S-1-1.5-1, S-1-1.5-2 and S-2-1.5-2. From left to right, the hysteresis loops represent the samples S-2-1.5-1, S-1-1.5-1, S-1-1.5-2 and S-2-1.5-2, respectively, and below each loop the domain images are shown and the respective field points are mentioned in the hysteresis loop.

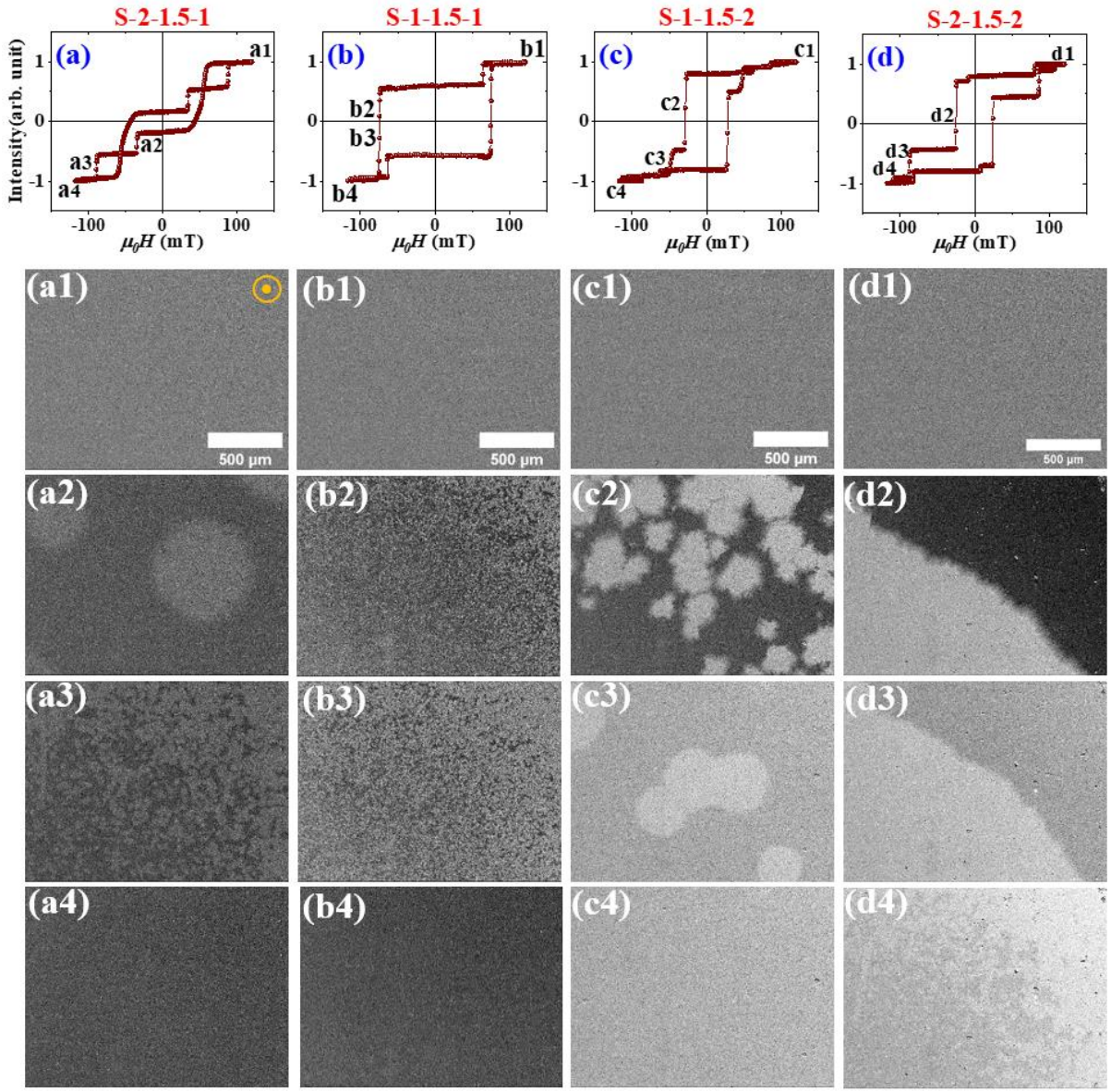

Figure 4.6: Hysteresis loops and domain images of the SAF samples S-2-1.5-1, S-1-1.5-1, S-1-1.5-2 and S-2-1.5-2 measured via MOKE microscopy.

For sample S-2-1.5-1, the hysteresis has three steps as shown in Figure 4.6 (a). Here, the magnetization reversal is achieved by both domain nucleation and domain wall (DW) propagation (Figure 4.6 (a1)–(a4)). Here, we have defined the magnetization directions for the Pt/Co layers above and below the Ir spacer layer by a red arrow (↑) and blue arrow (↑), respectively. In the first reversal (↑↑ – ↓↑), no domain has been observed and only a change in the contrast of domain image is there. This type of domain behavior may be explained as the

spin flop transition, which can be inferred from the slanted reversal of the hysteresis loop at the first reversal [188,189]. However, in the second reversal (↓↑ – ↑↓), bubble domains have been observed because of the sharp transition (Figure 4.6 (a2)). In the third reversal (↑↓ – ↓↓), the domains become remarkably small, which may be due to the lowering of AFM coupling between the layers (Figure 4.6 (a3)) [190]. In sample S-1-1.5-1, only two step reversal (see Figure 4.6 (b)) has been achieved via a large nucleation of small bubble domains (Figure 4.6 (b2)– (b3)).

In sample S-1-1.5-2, a three-step hysteresis loop is observed, which is shown in Figure 4.6 (c). Here, two different types of domains are observed at two different reversals, i.e., distorted bubble domain with a higher number of nucleations and symmetric bubble domain as shown in Figure 4.6 (c2) and (c3), respectively. Here, the bubble domains are quite similar to sample S-2-1.5-1 because of their comparable IEC strength. Sample S-2-1.5-2 exhibits a multi-step magnetization reversal where the reversal process is accompanied via first no domains and afterwards bigger domains. Finally, the reversal is completed via smaller bubble domains with more nucleations.

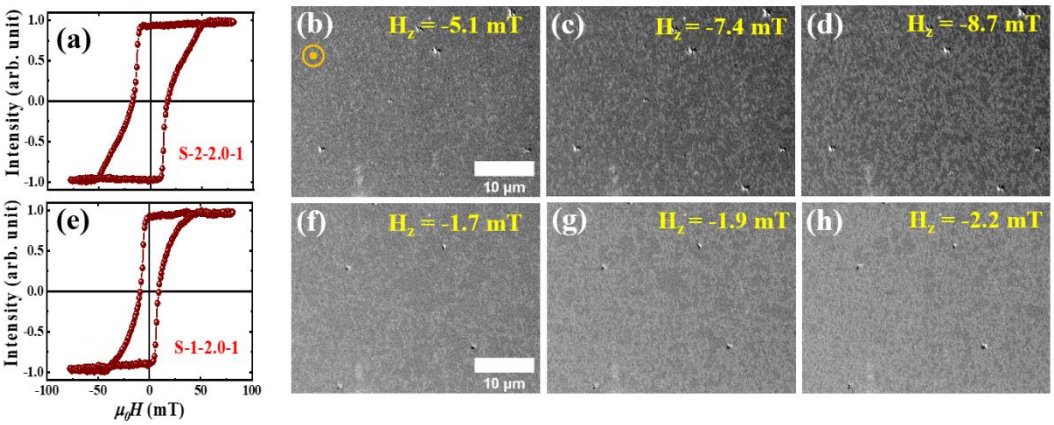

Figure 4.7: Hysteresis loops and domain images of the SAF samples S-2-2.0-1 and S-1-2.0-1, measured via MOKE microscopy.

Samples S-2-2.0-1 and S-1-2.0-1 show a bow-tie shaped hysteresis loop measured by magneto-optic Kerr effect microscopy shown in Fig. 6a and c. At the reversal, very small ripple kinds of domains are observed, indicated in Fig. 6b–d and f–h. The hysteresis loops for samples S-2-2.0-1 and S-1-2.0-1 shown in Figure 4.7 have been measured using a 5X objective. However, due to very small domain size, the domain images are captured using a 50X objective (as shown in Figure 4.7).

In Summary, SAF samples with PMA have been prepared and their magnetic properties have been studied extensively. The variation of Ir spacer layer thickness leads to different types of coupling among the FM layers with different spin configurations, i.e., FM and AFM couplings. Comparison of IEC energy and anisotropy energy suggests the relatively smaller angle between the spins of FM layers below and above the spacer layer in SAF samples. The size of the domains in the AFM coupled samples are found to be smaller than the FM coupled samples. At certain thickness of Ir spacer layer i.e., t_{Ir}=2.0nm, a canted magnetization reversal has been observed which needs to be explored further for the presence of chiral spin textures in this. Also, the multilayer stack needs to be optimized further to have AFM coupled skyrmions in that.

Chapter 5

Observation of Topological Hall Effect and Skyrmions in Pt/Co/Ir/Co/Pt System:

In the previous chapter (chapter 4), we have studied the magnetization reversal and domain structures in a perpendicularly magnetized Pt/Co system by varying the Ir thickness as well as the number of Co layers [130]. There we have varied the Ir spacer layer thickness as 1.0, 1.5 and 2.0 nm between two Co layers of 0.8 nm thickness. We found that for Ir 1.0 nm the interlayer exchange coupling (IEC) is ferromagnetic (FM) and for Ir 1.5 nm, the IEC is antiferromagnetic (AFM) i.e., synthetic antiferromagnets (SAF) [153,161]. In both of these multilayers with Ir thickness of 1.0nm and 1.5nm, we have observed bubble domains during the magnetization reversal which can be attributed to the higher anisotropy in the system. However, for the multilayer with Ir thickness of 2.0 nm, the hysteresis loop showed a slanted type of reversal which indicates that the magnetizations of different Co layers are in a relatively canted state during the reversal. This led us to explore these systems for a possible presence of chiral spin textures like skyrmions in it. Skyrmions [191–195] are highly promising topological structures that have garnered significant attention due to potential applications in spintronic devices such as magnetic data storage technologies and logic devices [196–198]. . These quasiparticles are stabilized by competing interactions/energies within the material such as exchange interaction, anisotropy [81,199], Dzyaloshinskii-Moriya interaction (DMI) [200], frustrated exchange interaction [201], dipolar interaction [202] etc. We have discussed the properties and advantages of these magnetic structures for application purpose [17,18,203–206] in the introduction part of these thesis. However, creating a good platform for the deterministic nucleation as well as detecting the presence of these quasi-particles in the system through the simplest techniques available is still a crucial part of this field. Previously, skyrmions have been observed in metallic thin films consisting of a single FM layer with thickness near spin reorientation transition (SRT) [207], in a multilayer system with significant

repetition of the FM and NM layers [71,173,208,209] etc. Raju et. al., have observed high-density skyrmions by taking multilayers of Ir/Fe/Co/Pt system by enhancing the DMI at both the interface of Ir/Fe and Pt/Co [79]. Similarly, Chen et. al., have observed the presence of skyrmions in Pd/Co multilayers with Ru spacer [71]. In the later work, the competition between DMI, dipolar interaction as well as RKKY interaction leads to the formation of these chiral spin textures. Further, skyrmion lattices can be stabilized by various types of other interactions and symmetries, such as multi-spin interactions [210], magnetic frustration [211,212], and bond-dependent exchange anisotropy [213–215]. However, there are no such reports where skyrmions have been observed just by varying the NM spacer layer thickness between two FM layers having a thickness in perfect PMA regime i.e. far away from the SRT regime. Therefore, in this work, we focus on these two samples (S-2-2.0-1 and S-1-1.0-1) from the work in the previous chapter with an Ir thickness of 2.0nm. Our goal is to comprehensively explore the formation and stability of skyrmionic structures, as well as its influence on Topological Hall effect (THE) signals, paying particular attention to how change in the Ruderman-Kittel-Kasuya-Yosida (RKKY) [158,159] interaction due to varying Ir spacer layer thickness impact these phenomena. To gain deeper insights into the magnetic structure, we utilize magnetic force microscopy for imaging of these chiral spin textures. Further THE experiments are performed to confirm the observed magnetic microstructure to be chiral in nature.

5.1 Sample details:

The two multilayer samples studied in this chapter are the samples S-2-2.0-1 and S-1-2.0-1 from our previous chapter with structure Si/Ta(3)/$[Pt(3.5)/Co(0.8)]_2$/Ir(2.0)/Co(0.8)/Pt(3.5) and Si/Ta(3)/Pt(3.5)/Co(0.8)/Ir(2.0)/Co(0.8)/Pt(3.5), respectively. Here onwards in this chapter, the two samples are renamed as Ir-2-1 and Ir-1-1, respectively. The schematic of the sample

structure has been shown in Figure 5.1 (a). The details of the growth of these samples have been explained in the "sample details" section of the previous chapter.

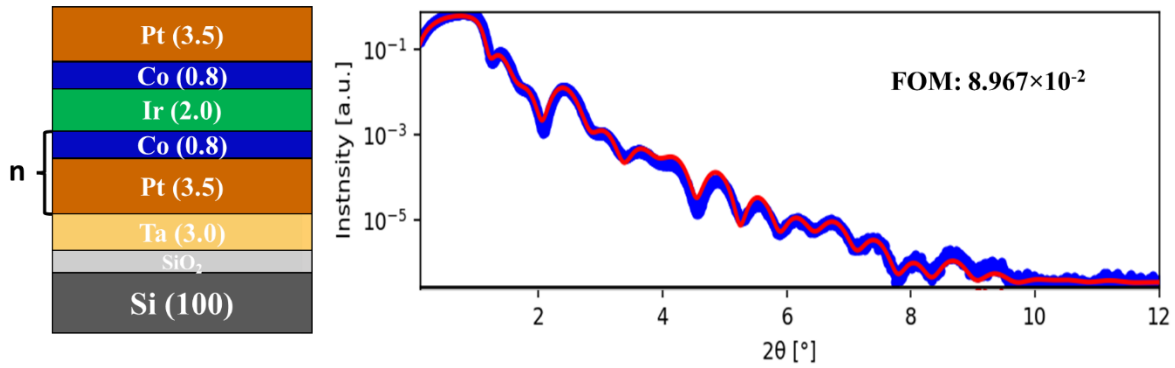

Figure 5.1: (a) Schematic of sample structure where n is 1 and 2 for samples Ir-1-1 and Ir-2-1, respectively, (b) XRR fitting of the sample Ir-1-1 performed by GenX.

5.2 Structural characterization:

The structural characterization of one of the samples of this series has been performed via cross-sectional transmission electron microscopy (TEM) measurement. This has been discussed in the previous chapter. Further, to understand the detailed structural property of the multilayer stack presented in this chapter, we have performed XRR for sample Ir-1-1. The fitting of the XRR data for the Ir-1-1 sample is shown in Figure 5.1 (b). The thicknesses of the layers are found to be 3.31, 3.73, 0.83, 2.05, 0.79, 3.08 nm for Ta, Pt, Co, Ir, Co, Pt layers,

Table 5.1: Thickness and roughness of respective layers of the sample Ir-1-1 extracted from XRR fitting by GenX. The error bars are also given for every layer.

Layers	Thickness (nm)	Error	Roughness (nm)	Error
Si	-	-	0.01	-
SiO2	0.76	-0.05, 0.08	0.29	-
Ta	3.31	-0.02, 0.02	0.29	-0.02, 0.01
Pt	3.73	-0.02, 0.03	0.49	-0.02, 0.03
Co	0.83	-0.04, 0.01	0.53	-0.01, 0.01
Ir	2.05	-0.04, 0.01	0.31	-0.01, 0.01
Co	0.79	-0.01, 0.03	0.59	-0.04, 0.01
Pt	3.08	-0.02, 0.01	0.36	-0.01, 0.01

respectively. Also, the roughness of the layers are found to be 0.29, 0.49, 0.53, 0.31, 0.59, 0.36 nm, respectively. The error bars for each layer are mentioned in the Table 5.1.

5.3 Magnetic characterization:

The magnetization reversal of the samples Ir-1-1 and Ir-2-1 have been shown in Figure 5.2 (a) and (b), respectively. It is observed that the magnetic hysteresis loops showed an out-of-plane easy axis with slanted magnetization reversal. The small remanence at zero magnetic field for Ir-1-1. is due to the balance of up and down domains with one layer of Co below and above the Ir spacer. However, for Ir-2-1, as there are two Co layers below the Ir and one Co layer above the Ir, a finite remanence is observed at zero field in this sample due to the imbalance of up- and down-domains [216]. It should be noted that the other samples of this series having Ir thickness 1.0 nm showed a sharp reversal in the out-of-plane applied magnetic field which indicates the FM coupling between the two Co layers. Whereas, by changing the Ir thickness to 1.5 nm, the coupling became AFM leading to SAF structure. Further, bubble domains have been observed in these samples having Ir thickness 1.0 nm as well as 1.5 nm [130]. However, the samples Ir-1-1 and Ir-2-1 show small ripple domains during the magnetization reversal as shown in the Figure 4.7 of chapter 4. Due to the limitations (resolution) of our Kerr microscopy,

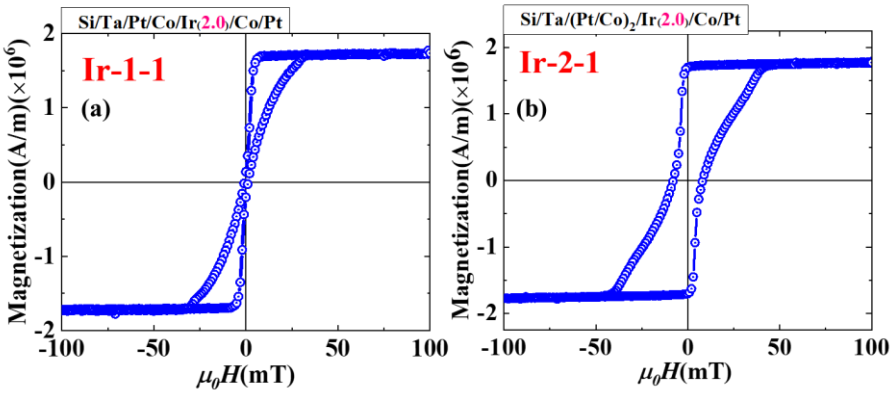

Figure 5.2: Out-of-plane magnetic hysteresis loops of sample (a) Ir-1-1 and (b) Ir-2-1 measured by SQUID-VSM.

we could not properly investigate these observed very small ripple domains. However, the loop

shape, as well as the domain structures, indicated the possible presence of chiral spin textures like skyrmions in it.

In order to observe if there is existence of any skyrmionic states, one needs to perform high resolution magnetic imaging. There are several methods to detect the presence and characteristics of skyrmions in magnetic materials. A few can be pronounced here such as, magnetic force microscopy (MFM)[21], magneto-optic Kerr effect (MOKE) microscopy [173,208], scanning tunnelling microscopy (STM) [77], X-ray photoemission electron microscopy (XPEEM) [75], Hall Effect Measurements, Lorentz transmission electron microscopy (LTEM) [71,76] etc. In this work, we have performed the magnetic force microscopy (MFM) measurement on both the samples Ir-1-1 and Ir-2-1 to detect the presence of skyrmions. The MFM images shown in Figure 5.3 (a) and (e) are taken at the demagnetized state (i.e., without applying any external magnetic field to the sample) for samples Ir-1-1 and Ir-2-1, respectively. In this condition, we have observed a labyrinth kind of domains or spin spirals which may be the outcome of the dominance of DMI, which favours the non-collinear spin textures, over the exchange favouring the collinear spin textures at this state [79,207,217]. By minimizing the total energy which includes exchange, DMI, anisotropy etc., one can get the spin spiral states in a system at a demagnetized state. The total energy of the system can be written as shown in equation 5.1,

$$E_{tot} = E_{ex} + E_{DMI} + E_{ani} + E_{Ze} + E_{RKKY} \quad \ldots\ldots. (5.1)$$

Where E_{exch} is the exchange energy, E_{DMI} is the DMI energy, E_{anis} the anisotropy energy, E_{Zeem} is the Zeeman energy and E_{RKKY} is the RKKY interaction energy. The Zeeman energy tends to align the magnetic moments along the field direction. It leads to the nucleation of skyrmions. Hence, further applying external magnetic fields in both samples, these labyrinth domains gradually break into smaller parts and form chiral spin textures like skyrmions. Here, isolated skyrmions rather than a skyrmion lattice phase have been observed in our samples. Skyrmion

lattices usually appear in bulk materials, where the bulk Dzyaloshinskii–Moriya interaction (DMI) stabilises the topological structures [194,218–220]. In a thin film system, metastable isolated skyrmions have been observed for $0 < \kappa < 1$ and skyrmion lattice phase for $\kappa \geq 1$. Here, $\kappa = \pi D/4\sqrt{AK_{eff}}$ is the temperature-dependent stability parameter where D, A and K_{eff} are DMI, exchange coupling, and magnetic anisotropy, respectively [217,221]. The observation of isolated skyrmions in our system may be due to $0 < \kappa < 1$. By further applying a higher magnetic field, the skyrmions get annihilated and a uniform saturated magnetic state is formed. It is found that the size of the skyrmions in Ir-2-1 is smaller as compared to the size of skyrmions in Ir-1-1. The reason may be attributed to the comparatively smaller anisotropy energy of sample Ir-2-1 which favours the smaller size of skyrmions [71]. The values of K_{eff} are found to be 5.55×10^5 and 7.44×10^5 J/m^3 for samples Ir-1-1 and Ir-2-1, respectively (mentioned in Table 4.2 of chapter 4) [130].

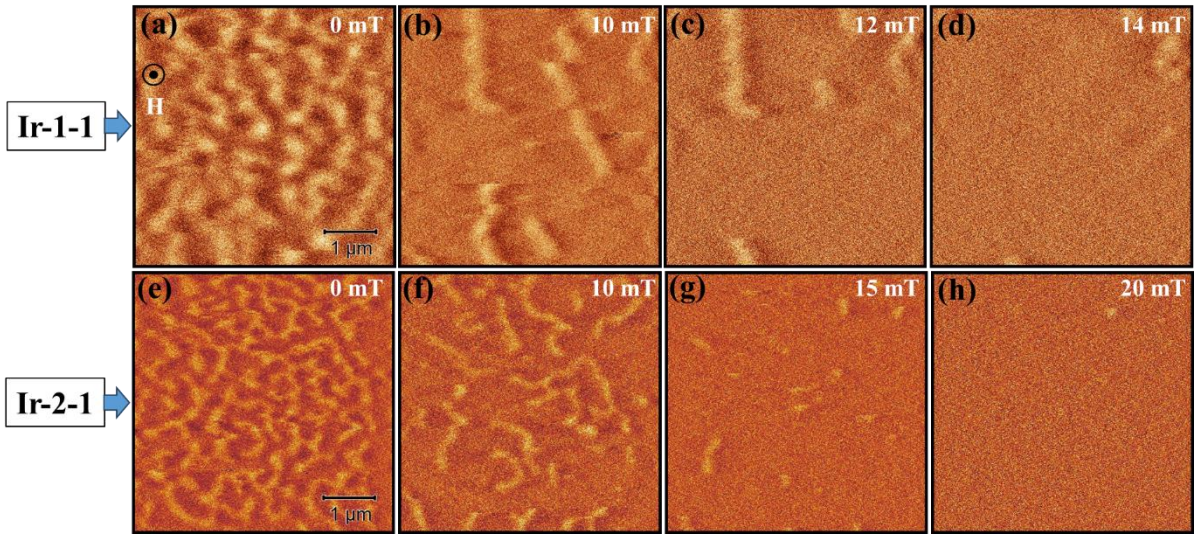

Figure 5.3: (a)-(d) are the MFM images of the sample Ir-1-1 at different external applied field of 0 mT, 10 mT, 12 mT and 14 mT, respectively. (e)-(h) are the MFM images of the sample Ir-2-1 at applied field 0 mT, 10 mT, 15 mT and 20 mT, respectively. The scale bar of 1 µm is shown (a) and (e).

Further to confirm the chirality of these observed spin textures, we have performed the magneto-transport measurements on a small rectangular piece of the sample Ir-1- 1 in the Van der Pauw geometry as shown in Figure 5.4 (a). The THE, characterized by the generation of a transverse charge current perpendicular to an applied magnetic field, has been the subject of extensive investigation due to its deep connection to the underlying magnetic texture's topological properties and becomes even more important when coupled with the existence of skyrmions. The conduction electrons' interactions with the chiral spin textures like skyrmions result in an emergent magnetic field, which is what causes the THE [76,221]. There are various reports in which topological Hall resistivity (ρ_{THE}) have been reported in different systems and a selected set of results are shown in Table 5.2. The observed ρ_{THE} value in our case is comparable to the literature values.

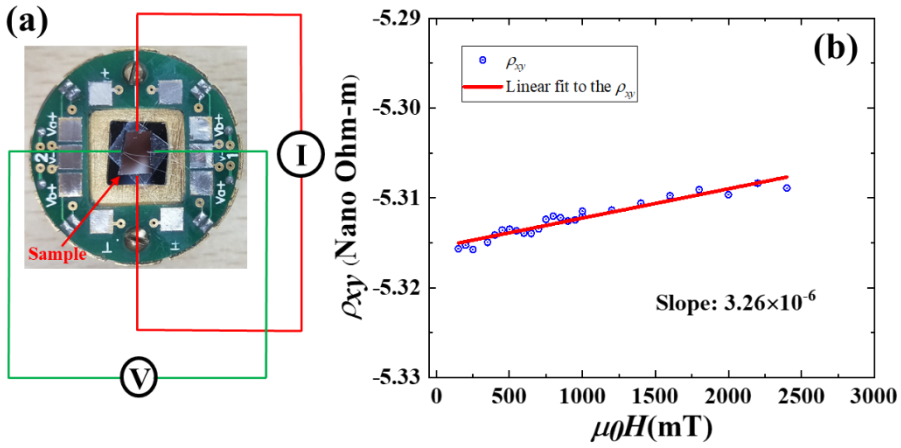

Figure 5.4: (a) Schematic of the measurement geometry for magneto transport measurement of the sample Ir-1-1 in the Van der Pauw geometry. (b) Saturation part of the resistivity measurement data (blue circles). The red line is the linear fit to this data.

To calculate the ρ_{THE} in our system, three effects have been considered that contribute to the total Hall resistivity of the sample. The ordinary Hall effect (OHE) has linear contributions in accordance with the magnetic field. The anomalous Hall effect (AHE) which usually arises in an FM due to the Berry curvature in momentum space, scales linearly with the perpendicular

component of magnetization. Then the THE related to the Berry phase in real space, occurs due to the presence of topologically nontrivial or chiral spin textures like skyrmions in the system.

Table 5.2: Comparison of the value of ρ_{THE} with a few existing literature.

System	ρ_{THE} in nΩ.m	Authors
[Pt(1.5)/Co(t_{Co})/W (1.5)]$_7$	1.3	Mourkas et al.[46]
T a(4)/[Pt(3)/Co(t)/T a(3)]$_6$	1.7	He et al.[40]
[Ir(1)/F e(0.5)/Co(0.5)/Pt(1)]$_{20}$	0.15	Raju et al.[26]
Single crystal MnSi	0.04	Schulz et al.[47]
Epitaxial thin film of FeGe	0.05	Kanazawa et al. [48]
Pt(3.5)/Co(0.8)/Ir(2.0)/Co(0.8)/Pt(3.5)	0.13	This work

Electrons when moving in such chiral spin textures, experience an extra fictitious magnetic field, get deflected perpendicular to the current direction giving rise to the THE [79,222–224]. Hence, the total Hall resistivity of the sample can be written as equation 5.2,

$$\rho_{xy} = R_0 H + R_s M + \rho_{THE} \quad \ldots\ldots. (5.2)$$

R_0H is the contribution from OHE. R_sM is the contribution from AHE. The subscript xy indicates the resistivity of the sample has been measured by applying the current in the x direction and measuring the voltage in the y direction. R_0 is the ordinary Hall coefficient, Rs is the AHE coefficient, and M is the out-of-plane magnetization of the sample. Therefore, the THE can be obtained by subtracting the other two contributions i.e., OHE and AHE contributions from the total Hall resistivity of the sample. In Figure 5.5 (a), the curve with blue circles depicts the Hall resistivity (AHE and THE) for our sample Ir-2 after subtracting the contribution from OHE by correcting the slope of the linear part of the total Hall resistivity (ρxy). The OHE contribution is very small in our case which is shown in Figure 5.4 (b). Further,

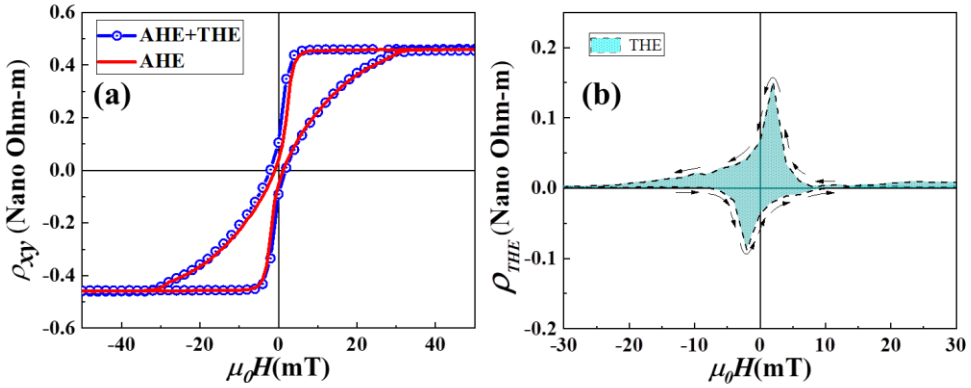

Figure 5.5: Topological Hall effect (THE) measurement of the sample Ir-1-1. (a) Total resistivity of the sample after removing the ordinary Hall effect component (blue circles) and the AHE fitting to the total Hall resistivity (red line), (b) ρ_{THE} extracted from the resistivity vs magnetic field measurement data after subtracting the OHE and AHE part.

the contribution from AHE is scaled with the $\rho_{xy}^{AHE+THE}$ by evaluating the AHE coefficient (Rs) which is plotted as the red line curve in Figure 5.5 (a). The calculation can be summarized in the following [217,225,226]. Equation 5.2 describes the total resistivity as a sum of three components. After subtracting the contribution from OHE, equation 5.2 becomes,

$$\rho_{xy} = R_s M + \rho_{THE} \quad \ldots\ldots (5.3)$$

At an applied magnetic field beyond the magnetic saturation, all the magnetic moment points in the direction of applied field and no topologically non-trivial spin textures are present in the system. Hence, ρ_{THE} becomes zero and equation 5.3 becomes,

$$\rho_{xy}^{Sat} = R_s M_s \quad \ldots\ldots (5.4)$$

where M_s is the saturation magnetization. Next, by putting the value of R_s from equation 5.4 i.e., ρ_{xy}^{sat}/M_S in equation 5.3 we extract the ρ_{THE} as equation 5.5.

$$\rho_{THE} = \rho_{xy} - R_s M \quad \ldots\ldots (5.5)$$

After subtracting the red line curve from the blue circle curve shown in Figure 5.5 (a), we have found a hump kind of feature in both the field sweeps from +ve saturated state to -ve one as well as from -ve saturated state to +ve one, represented in the Figure 5.5 (b) which is regarded as the contribution from THE. This shows the presence of chiral spin textures i.e. skyrmions in our system. The magnitude of THE in our sample is found to be 0.135 Nano Ohm-m.

In summary, we have observed a canted state of magnetization reversal and presence of skyrmions in a Pt/Co PMA system with Ir spacer layer by varying only the Ir spacer layer thickness between the two Co layers. The MFM images show labyrinth kind of domains at the demagnetized state and the presence of skyrmions is observed after applying external magnetic field to the samples. Further, we have observed a THE signal which indicates that the observed structures via MFM are of chiral spin textures. In this work we show that via the proper tuning of various energy along with inter-layer interactions (both dipolar and RKKY) it is possible to stabilize the skyrmions in the ferromagnet (e.g. Co) even when the thickness of the ferromagnet is well below the SRT regime. This paves the path to engineer such multilayer structure by varying the spacer layer thickness to have the presence of chiral spin textures such as skyrmions in the system.

Chapter 6

Effect of RKKY and dipolar interaction on the nucleation of high-density skyrmions in Pt/Co multilayer system with Ir as spacer layer:

The emergence of magnetic skyrmions as topologically protected spin textures has sparked significant interest in the field of condensed matter physics and spintronics due to their unique properties and potential applications in future magnetic storage and computing devices [204,227–230]. These nanoscale spin configurations, characterized by a swirling arrangement of magnetic moments, exhibit topological stability and non-trivial spin textures, making them promising candidates for information storage and manipulation at ultrahigh densities and low energy consumption [86,203,205,206]. In recent years, considerable efforts have been devoted to the investigation of skyrmion nucleation and manipulation in various magnetic systems, including thin films, multilayers, and heterostructures [199,207,221,231–233]. Characterising the spin configuration of these skyrmions is one of the primary objective to comprehend the underlying competing interactions that stabilise them as well as for optimizing device performance and designing novel skyrmion-based technologies. Previously, observation of skyrmions has been extensively studied in thin film multilayer systems with the repetitions of HM/FM layers [81,216,234,235], by considering the FM thickness near to spin reorientation transition (SRT) [236,237], with enhanced DMI by taking different heavy metal (HM) at both interfaces of FM layer [238], etc. Among the various thin film systems hosting chiral spin textures like skyrmions, HM1/FM/HM2 magnetic multilayers have garnered significant interest due to the generation of non-cancelling interfacial DMI produced by breaking the inversion symmetry. Also, it provides the flexibility to tune the magnetic properties largely by changing the thickness of each layer. He *et. al.*, have shown the evolution of skyrmions in a Pt/Co/Ta multilayer system with Co thickness near to SRT [231].

Lin *et. al.*, have shown the observation of these chiral spin textures in a Pt/Co/W multilayer system with enhanced Dzyaloshinskii-Moriya interaction (DMI) [232]. Recently, Cheng *et. al.*, have demonstrated the observation of bubble-like Neel skyrmions in a Pt/Co/Cu multilayer system by tuning the Co thickness as well as the number of periods of these multilayers [233]. However, there are very few reports which demonstrate the nucleation of these skyrmionic features by considering the FM thickness much below the SRT (in the PMA regime), with less repetition of number of period of these multilayers and simultaneously introducing the Ruderman–Kittel–Kasuya–Yosida (RKKY) interaction between the FM layers.

In the previous chapter (chapter 5), we have explored the stabilization of skyrmionic states with the variation of Ir spacer layer thickness between the two Co layers. In this chapter, we have considered a particular thickness of Ir spacer to have strong antiferromagnetic (AFM) coupling between the Co layers adjacent to the spacer. However, we have increased the number of repetitions of Pt/Co layers below and above the Ir spacer layer to simultaneously have the effect of dipolar interaction for the stabilization of skyrmions in our systems. By carefully balancing the contributions from DMI energy, RKKY interaction energy, dipolar energy, and magnetic anisotropy energy, we have achieved the nucleation of high-density skyrmions in these multilayer systems. The observation of skyrmions in these systems have been confirmed through the detection of topological Hall effect (THE) signals and magnetic force microscopy (MFM) imaging.

6.1 Sample details:

Two samples have extensively been studied in this work with structure $Si/SiO_2/Ta(3)/Pt(2.5)/[Pt(1)/Co(t_{Co})]_3/Ir(1.3)/[Co(t_{Co})/Pt(1)]_2/Pt(2.5)$ by varying t_{Co} as 0.8 and 1.0 nm and named as S1 and S2, respectively. Another two samples have also been prepared as control samples to demonstrate the existence of perpendicular magnetic anisotropy (PMA) in

the Pt/Co system and AFM coupling between the Co layers via Ir spacer. The sample names with structures have been mentioned in Table 6.1 below.

Table 6.1: Sample names with their structures. All the thicknesses shown in the parentheses are in nm.

Sample name	Structure
R1-FM	$Si/SiO_2/Ta(3)/Pt(3.5)/Co(0.8)/Ir(1.3)/Pt(3.5)$
R2-SAF	$Si/SiO_2/Ta(3)/Pt(3.5)/Co(0.8)/Ir(1.3)/Co(0.8)/Pt(3.5)$
S1	$Si/SiO_2/Ta(3)/Pt(2.5)/[Pt(1)/Co(0.8)]_3/Ir(1.3)/[Co(0.8)/Pt(1)]_2/Pt(2.5)$
S2	$Si/SiO_2/Ta(3)/Pt(2.5)/[Pt(1)/Co(1.0)]_3/Ir(1.3)/[Co(1.0)/Pt(1)]_2/Pt(2.5)$

All the samples have been prepared in a high-vacuum multi-deposition chamber manufactured by Mantis Deposition Ltd., UK. The base pressure of the chamber was ~ 7.5×10^{-8} mbar. The deposition pressure was ~1.7×10^{-3}mbar for Ta and ~1.5×10^{-3}mbar for Pt, Co and Ir layers. During sample preparation, the substrate table was rotated at 15 rpm to minimize the growth-induced anisotropy and also to have uniform growth of the films. The rates of deposition were 0.1 Å/s, 0.13 Å/s, 0.3 Å/s and 0.1 Å/s for Ir, Ta, Pt and Co, respectively.

6.2 Structural characterization:

The schematics of the sample structure for the sample S1 and S2 have been shown in Figure 6.1 (a). For the structural characterization of our samples, we have performed cross-sectional TEM imaging on the sample S1 (shown in Figure 6.1 (b)) in a high-resolution transmission electron microscope (HR-TEM) (JEOL F200, operating at 200 kV and equipped with a GATAN oneview CMOS camera). From the TEM image, the growth of these ultrathin layers are clearly visible. All the respective layers with their names have been indicated in the image itself.

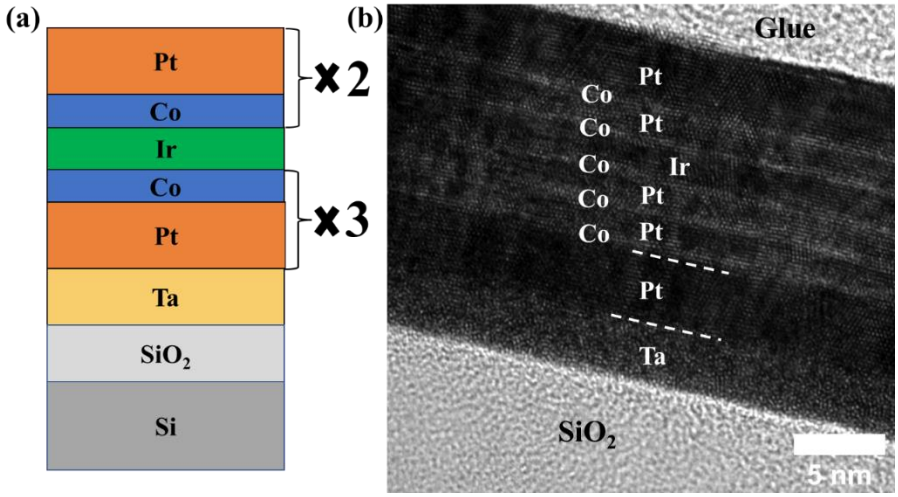

Figure 6.1: (a) Schematic of the sample structure for sample S1 and S2, (b) Cross-sectional TEM imaging for the sample S1.

6.3 Magnetic characterization:

The magnetization reversal of the samples have been measured at room temperature using a SQUID-VSM (Superconducting Quantum Interference Device-Vibrating sample magnetometer) manufactured by Quantum Design, USA. Figure 6.2 (a) shows the hysteresis loop of the reference sample R1-FM. Here the single Co layer with thickness 0.8nm deposited on the Pt heavy metal (HM) layer, shows strong PMA in the sample. The Ta layer has been used as a seed layer on the substrate which also favours the growth of Pt to have PMA in the Co layer. We have used the same thickness of Co i.e., 0.8nm considered from our previous study. However, for sample S2, the thickness of Co has been considered as 1.0nm to investigate the effect of reduction in the effective anisotropy on the evolution of skyrmionics spin textures in our sample. Further, before preparing the multilayer samples, we have optimized Ir spacer layer thickness to have strong AFM coupling between the Co layers. Figure 6.2 (b) shows the step-like behaviour in the hysteresis loop of the sample R2-SAF which indicates the AFM coupling between the FM layers forming a SAF structure for an Ir spacer thickness (t_{Ir}) of 1.3nm.

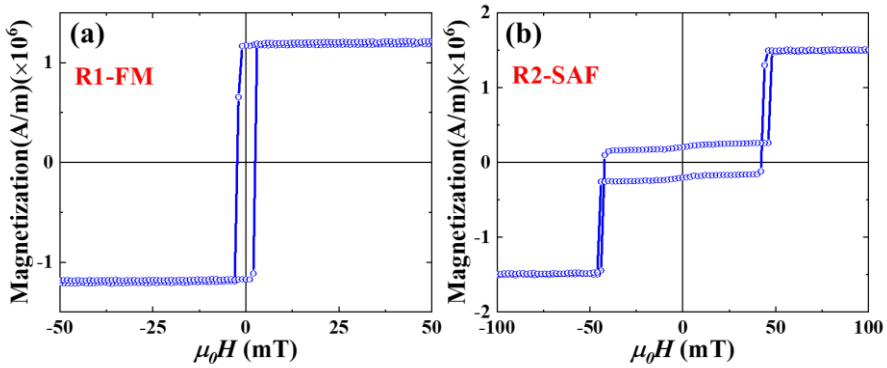

Figure 6.2: Magnetization reversal at room temperature for the sample (a) R1-FM and (b) R2-SAF. The measurement has been performed in the presence of an out-of-plane applied magnetic field.

Further, samples S1 and S2 have been measured in SQUID-VSM in the presence of an out-of-plane applied magnetic field as shown in Figure 6.3 (a) and (b). Both the samples showed the easy axis along the out-of-plane direction along with a slanted type of magnetization reversal with almost zero remanence. This may be due to the decrease in PMA of these sample with the introduction of RKKY coupling layer (i.e., Ir) between the Co layers.

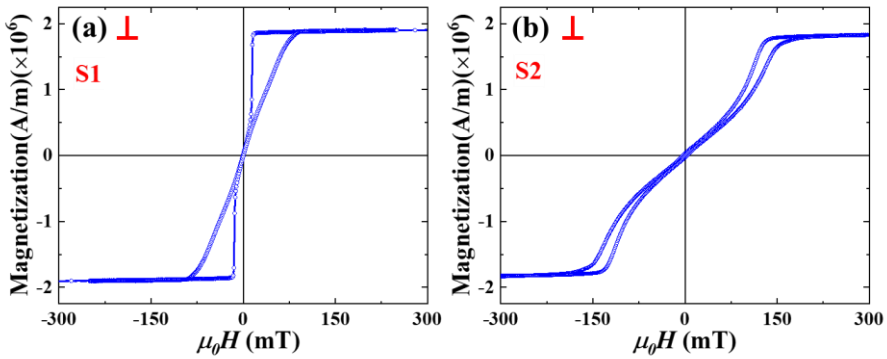

Figure 6.3: Out-of-plane hysteresis loop for the sample (a) S1 and (b) S2, measured by SQUID-VSM.

This indicates a favourable condition for the plausible presence of skyrmions in our multilayer samples. Although the t_{Ir} is kept at 1.3nm to have AFM coupling among the Co layers below and above the spacer layer, no intermediate step has been observed in the hysteresis loop for

both samples which indicates that the dipolar coupling due to the repetition of Pt/Co layers below and above the Ir spacer may be dominant over the RKKY interaction.

To get further insight into the change in anisotropy of the multilayer samples S1 and S2 as compared to the reference SAF sample, we have calculated the effective anisotropy energies (K_{eff}) of the samples R2-SAF, S1 and S2 by measuring the hard axis hysteresis loop in presence of an in-plane magnetic field. This is depicted in the below figure i.e., Figure 6.4 where the green arrow in each hysteresis plot indicates the anisotropy field (H_K) of the samples. The values of K_{eff} is calculated by using the relation $K_{eff} = H_K M_S/2$, with M_S being the saturation magnetization . The calculated values of H_K, M_S and K_{eff} for these three samples R2-SAF, S1 and S2 have been mentioned in the Table 6.2 below.

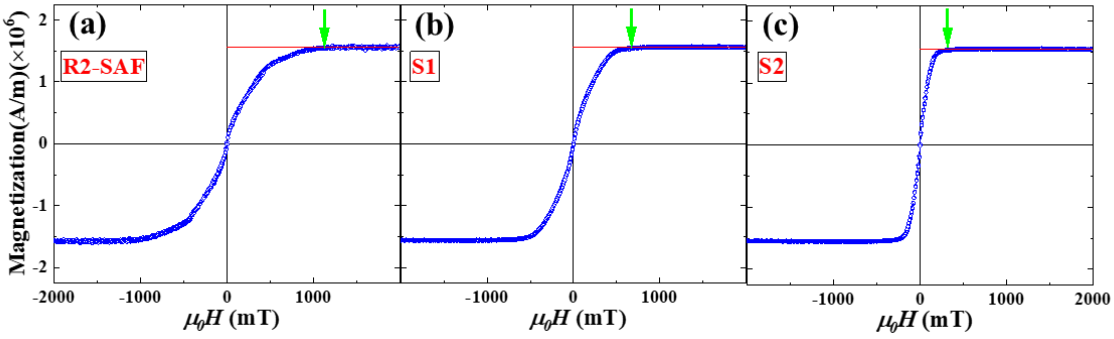

Figure 6.4: Hard axis hysteresis loop measured in presence of an in-plane magnetic field for the samples (a) R2-SAF, (b) S1 and (c) S2. The red line in each plot starting from the y-axis and parallel to the x-axis, indicates the saturation magnetization (M_S) of the samples.

It should be noted that the anisotropy energy is higher in the reference SAF sample (R2-SAF) as compared to the samples S1 and S2 having repetition of Pt/Co layers. This is due to the dominance of dipolar interaction over the PMA in the system. However, there is also a reduction in the K_{eff} value of S2 than S1. Although the sample structure as well as the number

of repetition of Pt/Co layers in both the sample are same, the reduction in the K_{eff} value is due to the higher thickness of Co layer in S2 as compared to S1.

Table 6.2: Calculated values of H_K, M_S and K_{eff} for the samples R2-SAF, S1 and S2

Sample	M_s **(in A/m)**	H_k **(in mT)**	K_{eff} **(in J/m^3)**
R2-SAF	1.56×10^6	1240	9.67×10^5
S1	1.56×10^6	744	5.81×10^5
S2	1.56×10^6	495	3.86×10^5

In order to elucidate the existence of skyrmionic states in both the samples, we have further performed magnetic force microscopy (MFM) measurement with an attodry 2100 MFM system manufactured by Attocube, Germany. Figure 6.5 shows the gradual evolution of skyrmionics states from the demagnetized state with respect to the increase in magnetic field values. The appearance of labyrinth domains at the demagnetized state shown in Figure 6.5 (a), is a consequence of the balance among various competiting energies present in our system such as, dipolar interaction, DM interaction, RKKY interaction, etc. Here, it should be noted that, the dominance of dipolar energy in our sample comes from the repetition of Pt/Co layers below and above the Ir spacer layer. The contribution from DMI energy comes from the Pt/Co interface as well as Co/Ir interface. Due to the less number of repetition of Pt/Co layers, the dipolar energy may not be sufficient to dominate over the exchange and anisotropy energy of the system to make a spin spiral state. However, due to the simultaneous effect of dipolar and RKKY interaction energy, labyrinth type of domains are formed in the demagnetized state. By applying out-of-plane magnetic field to the sample, these highly densed labyrinth type domains form into less densed stripes (shown in Figure 6.5 (b)-(d)). Here, the Zeeman energy tries to make the spins align in the direction of applied magnetic field from the spin spiral state and

forms the stripe phase. When the magnetic field is increased further, these magnetic stripes gradually breaks into isolated skyrmion like magnetic domains as shown in Figure 6.5 (e)-(g) and forms a disordered skyrmion state. By further increasing the magnetic field towards the saturation, the magnetic contrast of these isolated skyrmions gradually fades away and go to a single domain state by showing uniform contrast through out the image. Similar type of behavior of labyrinth type domain formation at demagnetized state and gradual beaking into skyrmionic phases with the application of magnetic field, has been observed for the sample S2 via MFM imaging which has been shown in the Figure 6.6. In both the samples S1 and S2, the skyrmions have been observed to be stable in a wide range of magnetic field after their nucleation at different field values.

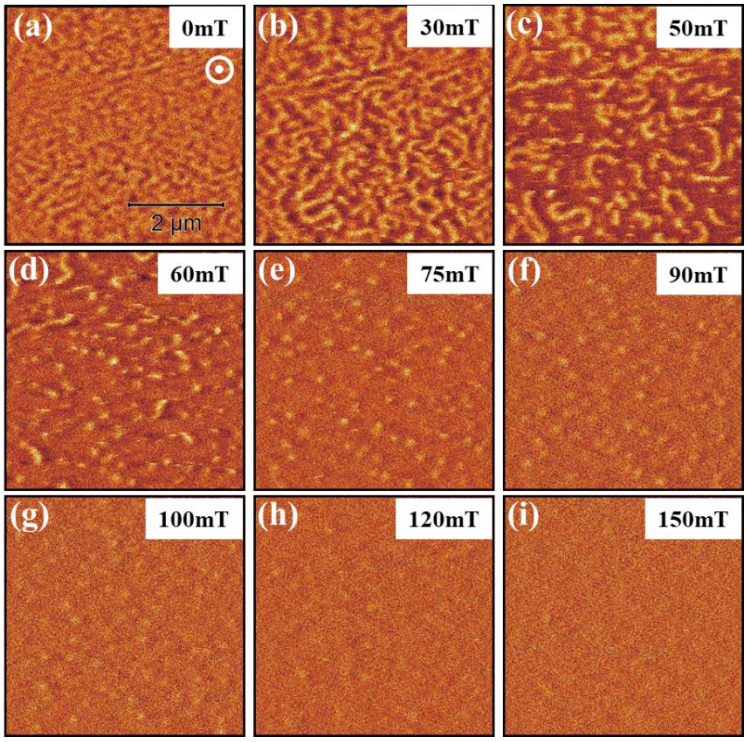

Figure 6.5: MFM images of the sample S1 at different out-of-plane applied magnetic field. The field values have been mentioned in the inset of each image.

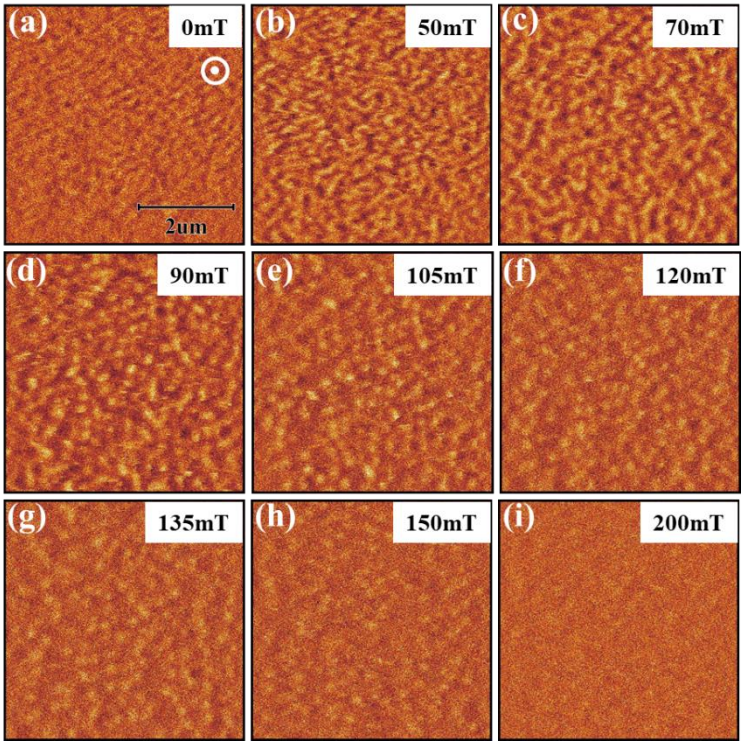

Figure 6.6: MFM images of the sample S2 at different out-of-plane applied magnetic field. The field values have been mentioned in the inset of each image.

In order to confirm the observed spin textures to be chiral in nature, magnetotransport measurements have been performed on both sample S1 and S2 via a physical property measurement system (PPMS) manufactured by Quantum Design, USA. Small rectangular pieces of both the samples have been measured in the Van der Pauw geometry keeping two voltage probes exactly perpendicular to the two current probes. However, we have adapted a five-probe measurement with an extra voltage probe to avoid the contribution of the magnetoresistance signal to the total Hall resistivity of our sample. This has been discussed extensively in the sub-section 2.3.3 of Chapter 2 of this thesis. The measurement is performed by applying a constant current to the sample in the presence of a sweeping perpendicular magnetic field which results in a transverse Hall voltage proportional to the magnetic field and the charge carrier density. This gives the total resistivity of the sample which consists of these components i.e., ordinary Hall effect (OHE) and anomalous Hall effect (AHE) [239]. In the presence of chiral spin textures like skyrmions in the sample, an emergent magnetic field is

produced due to the interaction of the conduction electrons with the skyrmions, which yields the additional contribution i.e., topological Hall effect (THE) [229,240–242]. Hence, the total Hall resistivity of the system in the presence of chiral spin textures can be written as [76,79,217,243,244],

$$\rho_{xy} = R_0 H + R_s M + \rho_{THE} \quad \text{.....(6.1)}$$

R_0H is the contribution from OHE. R_sM is the contribution from AHE. The subscript xy indicates the resistivity of the sample has been measured by applying the current in the x direction and measuring the voltage in the y direction. R_0 is the ordinary Hall coefficient, Rs is the AHE coefficient, and M is the out-of-plane magnetization of the sample. By subtracting the contribution of OHE and AHE from the total Hall resistivity, the topological Hall resistivity of the sample is calculated. This has also been explained in detail in the previous chapter (i.e., Chapter 5) explaining the importance of getting THE signal with connection to the presence of skyrmions in our system. During the measurement, a current value of 0.5 mA is applied and the corresponding voltage is measured. The curve with blue circles in Figure 6.7 (a) and (b) depicts the Hall resistivity (AHE and THE ($\rho_{xy}^{AHE+THE}$)) for our samples S1 and S2, respectively. The contribution from OHE, which is very small in our case, has been subtracted by correcting the slope of the linear part of the total Hall resistivity (ρ_{xy}). Further, the contribution from AHE is scaled with the $\rho_{xy}^{AHE+THE}$ by evaluating the AHE coefficient (R_s) which is plotted as the red line curve (ρ_{xy}^{AHE}) in Figure 6.7 (a) and (b). Thus, by subtracting the ρ_{xy}^{AHE} from $\rho_{xy}^{AHE+THE}$, we get a hump like behaviour in both the field sweeps i.e., from +ve to -ve and from -ve to +ve, which is the contribution from THE in our samples. The topological Hall resistivity has been shown in the Figure 6.7 (c) and (d) for sample S1 and S2, respectively.

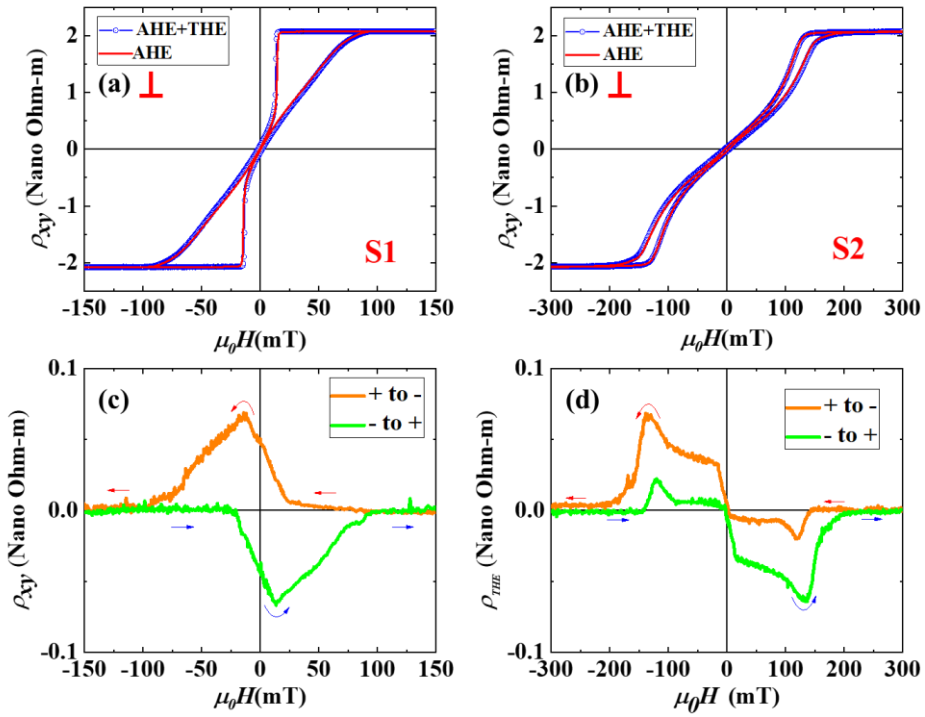

Figure 6.7: Scaling of the contribution from AHE and THE (blue circle) with the AHE (red line) for (a) S1 and (b) S2. (c) and (d) represents the subtracted topological Hall resistivity for the sample S1 and S2, respectively.

The values of the topological Hall resistivity for samples S1 and S2 are found to be 0.062 and 0.068 Nano Ohm-m, respectively which is comparable to the previously reported literature values. The comparatively higher values of the THE in sample S2 as compared to S1 is due to the higher density of skyrmions observed in S2 . By counting the number of skyrmions present in an area of 5µm × 5µm area as shown in Figure 6.5 and Figure 6.6, the densities of skyrmions are found to be 3.6×10^{12} Skyrmions/m^2 and 5.2×10^{12} Skyrmions/m^2 for S1 and S2, respectively. Further, the shape of the skyrmions found in our sample are circular in nature. Therefore, we calculate the size of these skyrmions by measuring the diameters from the MFM images. Figure 6.8 (a) and (b) shows the measured diameter of various skyrmions observed in the MFM images for sample S1 and S2, respectively. From the lognormal fitting, the average skyrmion dimeter for samples S1 and S2 are found to be 135 and 154 nm, respectively. The increase in average

size of the skyrmions in S2 is due to the reduction in the anisotropy of S2 as compared to S1 [71].

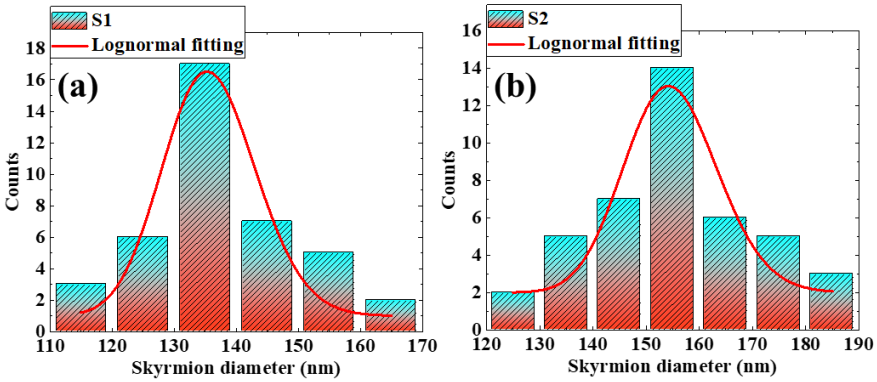

Figure 6.8: The average skyrmion size analysis for the skyrmions observed in the sample (a) S1 and (b) S2. The red line in the both the plots depicts the lognormal fitting to the measured data to calculate the average skyrmion size.

In summary, we have prepared multilayer samples having repetition of Pt/Co layers with Ir as a spacer layer of particular thickness to have antiferromagnetic RKKY interaction between the ferromagnetic layers below and above the Ir spacer. The simultaneous effect of dipolar and RKKY interaction leads to a slanted type of magnetization reversal giving rise to the nucleation of high density skyrmions observed via MFM imaging. Further, the finite THE signal from our samples confirm observed spin textures to be chiral in nature. Further, we found that the higher topological Hall resistance in the sample leads to the higher skyrmion density whereas, the decrease in the anisotropy makes the skyrmion size comparatively larger. Our study reveals a very robust method of necluating high density skyrmions with the simultaneous effect of dipolar and RKKY interaction in the system. These systems can further be explored for the deterministic current induced nucleation as well as propagation of skyrmions which can be useful for future spintronic application.

Chapter 7

Spin dynamics in an in-plane magnetized CoFeB/Ir/CoFeB system with FM and AFM coupling:

The coupling between two ferromagnetic (FM) layers via a nonmagnetic spacer layer holds significant importance in spintronic applications, enabling the development of advanced spin-based devices with improved stability, functionality, energy efficiency, and integration capabilities. The characteristics and coupling strength between FM layers can be tailored by adjusting the properties of the nonmagnetic spacer layer [159,160,245]. This tunability allows for fine-tuning device functionalities, such as switching behavior, magnetic anisotropy, and spin wave propagation, etc., to meet specific application requirements. Depending on the thickness of spacer layer, if the relative orientation of the magnetic moments in the FM layers below and above the spacer layer are parallel, the coupling becomes FM. On the otherhand, the antiparallel orientation of magnetic moments in both the FM layer leads to the synthetic antiferromagnetic (SAF) configuration. This has extensively been discussed in the introduction part of this thesis and also in Chapter 3. Several aspects of SAFs have been explored having advantage for spntronic applications such as, a key component in the magnetic tunnel junction (MTJ) devices [176,246,247], reduction of skyrmion Hall effect in SAF bilayers [172,173,209], etc. Apart from these, it is also very crucial to study the spin dynamics in these SAFs which has not been explored much yet. By studying spin dynamics, researchers can explore how spin waves propagate, interact, and transfer information within SAFs, which is relevant for spintronic devices like spin torque oscillators and magnetic memory devices. Spin waves, which are basically the disturbance in the local magnetic ordering, are considered as promising data carriers for modern computing devices. Spin waves are particularly interesting due to their unique features, which include the ability to have Joule heat free transfer

of spin information over relatively long distances, the ability to achieve submicrometer wavelength at microwave frequencies, to be manipulated by electronic signal via magnetic fields, and realizing the concepts of wave based computing, etc [248,249]. Magnons are quanta of these spin waves which can coherently connect to distinct physical platforms in quantum systems where information can be encoded by both the amplitude and the phase of spin waves [250]. Hybrid magnonic systems have attracted great attention due to their applications in quantum information, communications, and sensing [251,252]. Although individual magnonic modes can be manipulated by varying the material properties of the magnetic layer, a unique approach of generating new spin-wave states involves coherently coupling two modes by tuning them into resonance. Previously, magnon-magnon coupling has been explored in single magnets [253–256] and magnetic bilayers [250,257,258]. However, SAF systems also show a great potential as a host of magnon-magnon coupling. Recently, Dai *et. al.*, have numerically demonstrated coupling between acoustic and optic magnon modes in an SAF system [259]. Further, Shiota *et. al.*, have experimentally observed the presence of magnon-magnon coupling in a SAF system of CoFeB layers exchange coupled via Ru spacer [260]. In-phase acoustic mode (AM) and out-of-phase optic mode (OM) are the two uniform precession magnon modes that characterise the magnetization dynamics of the SAF. The hybridization of these two magnon modes can happen as a result of the interlayer exchange coupling (IEC) between the two FM layers which can lead to the magnon-magnon coupling in SAF. The coupling in such systems can be introduced by a few approaches which can break the parity or exchange symmetry to introduce an anti-crossing gap between the AM and OM [256]. One approach is to tilt the sample towards a perpendicular direction thereby breaking the rotational symmetry of the hard axis [260]. Another approach is to consider different thicknesses of FM layers below and above the spacer layer which can break the parity symmetry to introduce a magnon-magnon coupling [261,262]. In this context, we have prepared in-plane magnetized

CoFeB layers of different thicknesses interleaved with the Ir spacer layer to explore the possibility of magnon-magnon coupling in our system. By performing the ferromagnetic resonance (FMR) measurements in the frequency sweep mode, we have extracted the acoustic and optical modes for our sample. However, from the analysis, we could not find any anti-crossing gap between these two magnon modes which indicates the absence of magnon-magnon coupling in our system.

7.1 Sample details:

Two samples M1 and M2 have been prepared with structure $Si/SiO_2/Ta(3)/CoFeB(10)/Ir(t_{Ir})/CoFeB(7)/Ta(3)$ where, t_{Ir} is varied as 0.8 nm and 1.3 nm for M1 and M2, respectively. Another reference sample R1 of one FM layer with structure $Si/SiO_2/Ta(3)/CoFeB(10)/Ir(1.3)/Ta(3)$ has been prepared. The Ir layer with 1.3 nm thickness has been considered from the previous chapter to have antiferromagnetic (AFM) coupling between the CoFeB layers. All the samples have been prepared in a high-vacuum multi-deposition chamber manufactured by Mantis Deposition Ltd., UK. The base pressure of the chamber was better than 5×10^{-8} mbar. The deposition pressure for the Ta, CoFeB and Ir layers were approximately 1.6×10^{-3} mbar, 8.1×10^{-4} mbar and 1.5×10^{-3} mbar, respectively. During sample preparation, the substrate table was rotated at 10 rpm to minimize the growth-induced anisotropy and also to have uniform growth of the films. The rates of deposition were 0.13 Å/s, 0.2 Å/s and 0.1 Å/s for Ta, CoFeB and Ir layers, respectively.

7.2 Structural characterization:

The schematic of the sample structure has been shown in Figure 7.1 (a). For the structural characterization of our samples, we have performed cross-sectional TEM imaging on the sample M1 (shown in Figure 7.1 (b)) in a high-resolution transmission electron microscope (HR-TEM) (JEOL F200, operating at 200 kV and equipped with a GATAN oneview CMOS

camera). From the TEM image, the growth of the layers seems to be uniform and the thicknesses of each layer matches with the calibrated thicknesses by quartz crystal microbalance (QCM) in our sputtering system. From the image the bright contrast in the major portion of top layer indicate that the capping Ta layer has almost been oxidized.

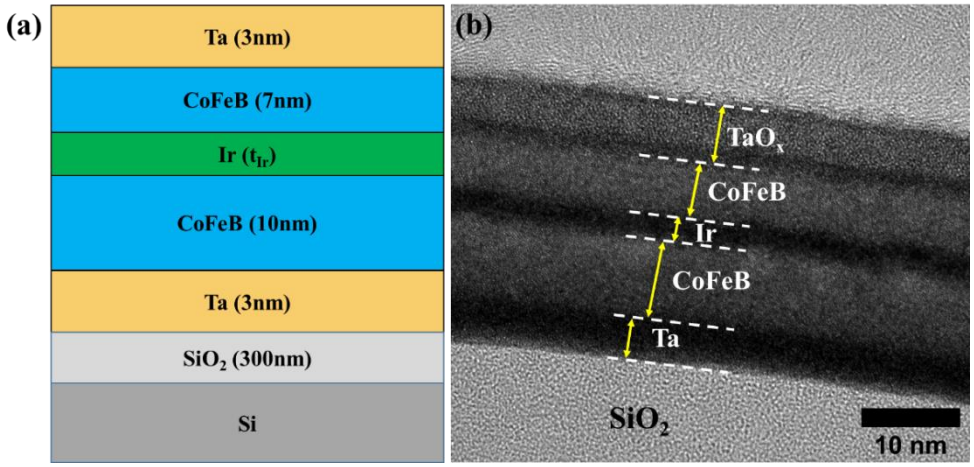

Figure 7.1: (a) Schematic of sample structure, (b) Cross-sectional TEM image of sample M1.

7.3 Magnetic characterization:

The magnetization reversal as well as domain images of all the samples have been measured via magneto-optic Kerr effect (MOKE) microscopy in presence of an in-plane applied magnetic field. Sample R1 having a single FM layer, shows a sharp reversal with square shaped hysteresis loop along its easy axis (EA). Here the magnetization reversal is happening through the domain wall (DW) motion. It should be noted here that at this position, the angle between the orientation of the sample and the applied magnetic field direction is considered as 0 degree. Here the sample shows a sharp reversal with maximum remanence. However, by rotating the sample in the plane making a 90 degree angle with respect to the easy axis, the magnetization reversal happens through coherent rotation indicating it to be the hard axis (HA). This behaviour indicates that the reference sample R1 with a single FM layer shows an uniaxial anisotropic nature. Figure 7.2 (a) shows the hysteresis loops of the sample R1 measured at EA (0 degree). Further, the sample M1 with a 0.8 nm thick Ir spacer layer between the two CoFeB

layers of thickness 10 nm and 7 nm, respectively, shows a similar type of magnetization reversal as of R1. This may be due to the FM-IEC between the CoFeB layers via the Ir spacer i.e., at this particular thickness of Ir spacer, the sample M1 is ferromagnetically coupled. Figure 7.2 (b) shows the hysteresis loops of the sample M1 along the EA. However, for the sample M2 with Ir spacer thickness of 1.3 nm, the Kerr microscopy hysteresis loop at the easy axis shows a clear step-like reversal with an in-plane applied magnetic field sweep. This clearly indicates that the CoFeB layers are antiferromagnetically coupled forming a SAF structure (shown in Figure 7.2 (c)). The sharpness of the steps gradually reduces towards the hard axis. The hysteresis loops at different angles (0, 30, 60 and 90 degrees) for the samples R1, M1 and M2 have been shown in Figure 7.2 (d), (e) and (f), respectively.

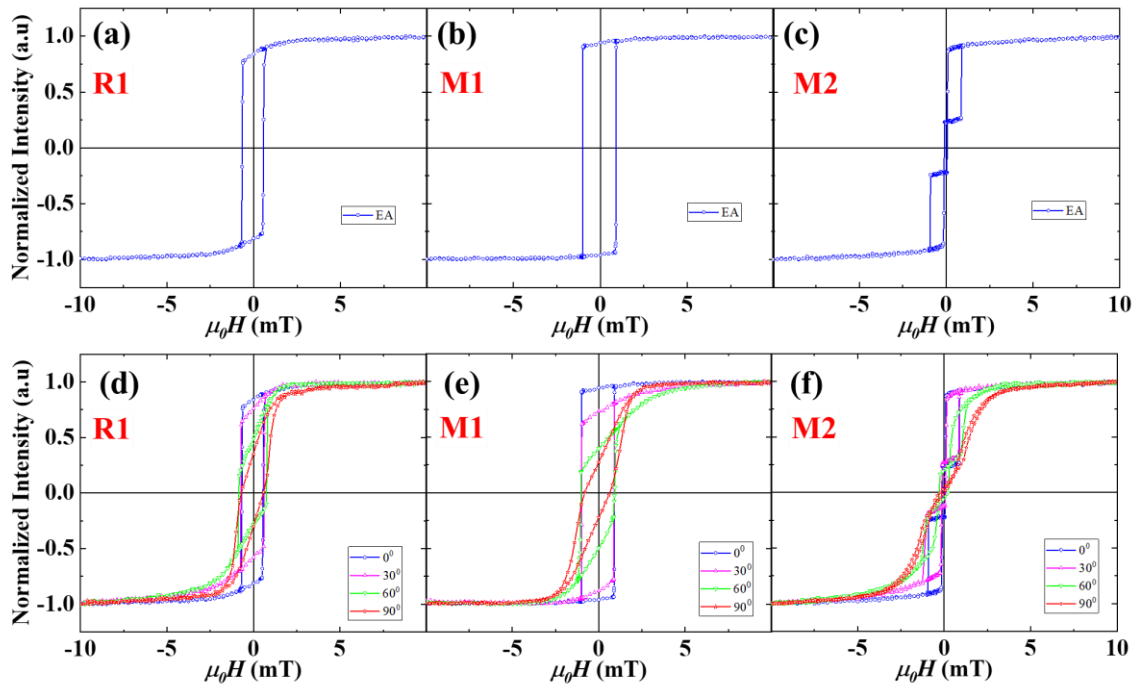

Figure 7.2: Kerr microscopy hysteresis loops for the samples (a) R1, (b) M1, and (c) M2 measured along the easy axis. (d), (e) and (f) shows the comparison of hysteresis loops for R1, M1 and M2 at different angles such as 0, 30, 60 and 90 degrees.

The magnetic domain images captured at easy axis for all the samples have been shown in Figure 7.3. For the sample R1, the domain images recorded clearly shows the big stipes during the reversal as shown in Figure 7.3 (a1)-(a4). For the sample M1, although the magnetization reversal happens through DW motion similar to the sample R1, the sharp reversal hinders the capturing of better domain images (shown in Figure 7.3 (b1)-(b4)). For the SAF sample (M2), (c1)-(c4) are the domain images shown in Figure 7.3. The big stripe domain observed in Figure 7.3 (c2) is during the first step of magnetization reversal. However, due to very sharp reversal in the second step, domain images could not be captured.

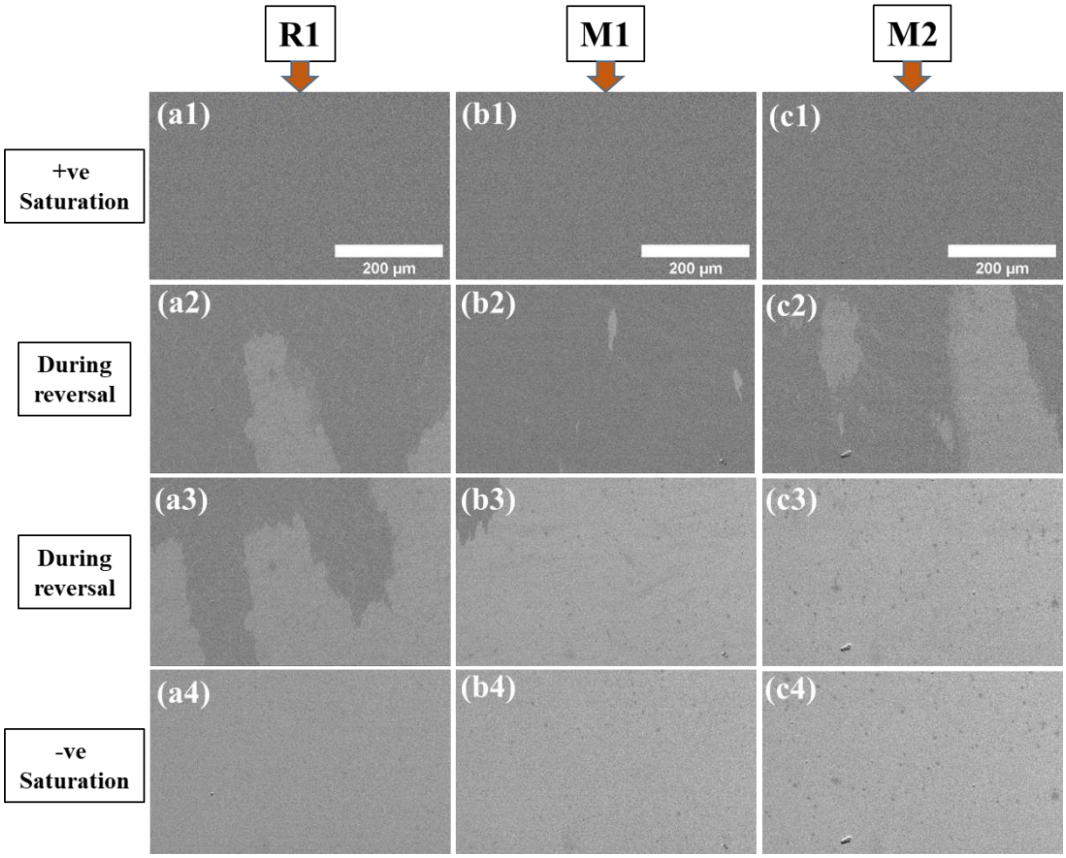

Figure 7.3: Magnetic domain images captured by Kerr microscopy for the samples R1, M1 and M2. (a1) and (a4) are the domain images at +ve and –ve saturation, respectively, for the sample R1. (a2) and (a3) shows the domains during the reversal. Similarly, (b1)-(b4) are the domain images for M1 and (c1)-(c4) are the domain images for M2.

In order to investigate the magnetization dynamics of the prepared samples, co-planer wave-guide (CPW) based NanoOsc instrument phase FMR measurements have been performed. Here the sample was placed on the CPW in a flip-chip manner. All the FMR measurements were carried out where the applied magnetic field is in the film plane direction. For each field sweep measurement, the frequency was fixed and swept an external magnetic field in the range of 0-5000 Oe. The gilbert damping parameter (α) is estimated by the acquisition of FMR spectra within the frequency (*f*) range of 4-10 GHz. The measured FMR spectra have been shown in Figure 7.4 for all the samples. All FMR measurements in this study were carried out at a microwave power of 25 mW. To extract the FMR peak position (H_{res}) and the line width (ΔH) each FMR spectra has been fitted by the derivative Lorentzian function,

$$FMR\ Signal = A\frac{4\Delta H(H-H_{res})}{[4(H-H_{res})^2+\ \Delta H^2]^2} - S\frac{\Delta H^2-4(H-H_{res})2}{[4(H-H_{res})^2+\ \Delta H^2]^2} + offset \quad \text{..... (7.1)}$$

Where, *A* and *S* are the coefficients of antisymmetric and symmetric components, respectively [25–27]. The extracted H_{res}values are plotted with *f* as shown in Fig 7.4 (d) and fitted using the Kittel equation [263]. Further, to get the value of gyromagnetic ratio (*γ*), the frequency (*f*) vs H_{res} plot is fitted (shown in Figure 7.4 (d)) using the Kittel equation [263],

$$f = \frac{\gamma}{2\pi}\sqrt{(H_{res}+H_k)(H_{res}+H_k+4\pi M_{eff})} \quad \text{..... (7.2)}$$

where, H_K is anisotropy field and $4\pi M_{eff}$ is the effective magnetization. The gyromagnetic ratio (*γ*) is obtained from this fitting and used to further evaluate the damping value (α) of the FM layer by fitting the following linear equation the ΔH vs *f* plot (as shown in Figure 7.4 (e)),

$$\Delta H = \Delta H_0 + \frac{4\pi\alpha f}{\gamma} \qquad \ldots\ldots. (7.3)$$

Here, ΔH_0 is the broadening due to inhomogeneity in the sample. The slope of equation 7.3 gives the damping value α as 0.0135 ± 0.0002, 0.0109 ± 0.0002 and 0.0128 ± 0.0002 for the samples R1, M1 and M2, respectively. Interestingly, we have observed a shift in the H_{res} value for the samples M1 and M2 as compared to the reference layer R1. Accordingly, a change in damping values has been observed which may be due to the interlayer coupling in our system. This motivated us to explore the nature of the coupling in these SAF systems. The existing literature suggests the presence of magnon-magnon coupling in these types of SAF system.

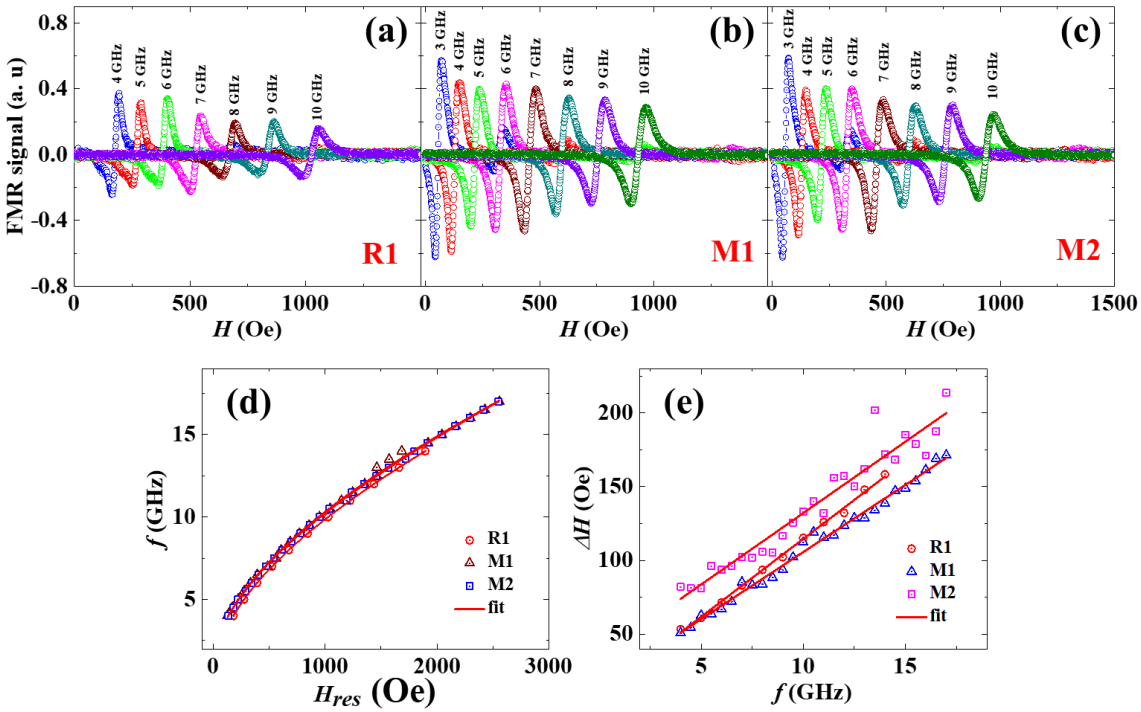

Figure 7.4: Frequency dependent FMR spectra with a varying in-plane magnetic field for the samples (a) R1, (b) M1, and (c) M2. (d) The f vs H_{res} plot with the Kittel equation fitting. (e) The damping value (α) is evaluated by the linear fit of ΔH vs f for all the samples.

Further, to find out the possible existence of magnon-magnon coupling in our SAF sample, we have performed the FMR measurement in the frequency sweep mode at different magnetic field

values for sample M1 and M2 [260,261,264]. The FMR spectra for all the samples in frequency sweep mode are fitted with the Lorentzian equation,

$$FMR\ Signal = A\frac{4\Delta f(f-f_{res})}{[4(f-f_{res})^2+\ \Delta f^2]^2} - S\frac{\Delta f^2-4(f-f_{res})2}{[4(f-f_{res})^2+\ \Delta f^2]^2} + offset \quad \ldots\ldots. (7.4)$$

There are two uniform precession magnon modes that describe the magnetization dynamics of the SAF, namely the in-phase acoustic mode (AM) and the out-of-phase optic mode (OM). From the Lorentzian fitting, the resonance frequencies (f_{res}) for the two modes are extracted for each magnetic field value. Further, these AM and OM mode resonance frequencies are plotted for each field value as shown in Figure 7.5 (a) and (b) for the samples M1 and M2, respectively. The FMR curves for a few selected field values for sample M2 in the frequency sweep mode has been shown in the Figure 7.5 (c). In the presence of coupling between the two modes, an avoided crossing region is expected to occur. The coupling strength (g) is calculated as the half

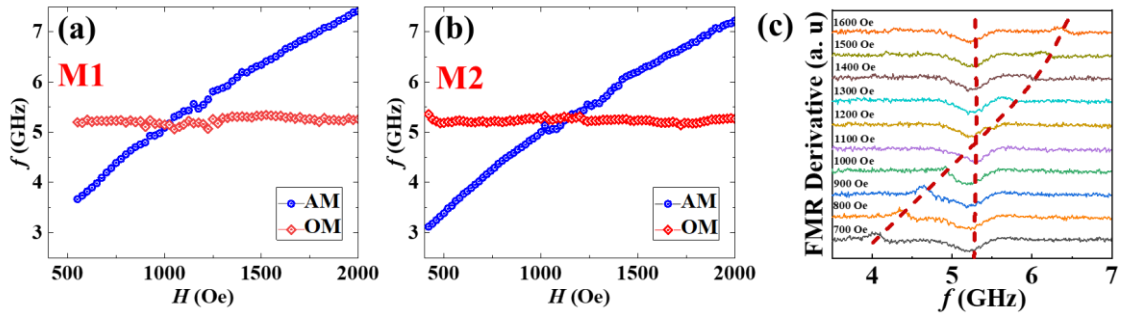

Figure 7.5: Plot of f_{res} vs H for both the AM and OM branches for the samples (a) M1 and (b) M2. (c) FMR curves for a few selected field values in the frequency sweep mode for sample M2.

of the minimum splitting between the two frequency modes at the anticrossing point [259]. However, we observe the clear crossing of these two modes for both the FM as well as SAF samples [265–267]. This crossing reflects that there is no coupling between the two modes. This indicates the absence of magnon-magnon coupling in our studied system.

In summary, we have prepared in-plane SAF samples of asymmetric structure (i.e., the thicknesses of FM layers below and above the spacer layer are different) with Ir as the spacer layer. The step-like reversal of the hysteresis loop confirms the AFM coupling between the CoFeB layers via the Ir spacer. FMR measurements in the frequency sweep mode have been performed to explore the possible presence of magnon-magnon coupling in our system. However, the signature of the magnon-magnon coupling i.e. the avoided crossing region is absent between the AM and OM modes in the observed data. This clearly indicates the absence of magnon-magnon coupling in the studied SAF systems. Moreover, this can be further explored by modifying the sample structure.

Chapter 8

Summary and conclusion:

Synthetic antiferromagnets (SAFs) play a crucial role in spintronics, a field that aims to harness the spin of electrons for advanced electronic devices. SAFs consist of two or more ferromagnetic layers coupled antiferromagnetically through a non-magnetic spacer via the RKKY interaction. This configuration allows for precise control over magnetic properties, such as magnetic moment and coercivity, offering several advantages for spintronic applications. One key advantage is their stability against external magnetic fields. Unlike single FM layers that can be easily influenced by external perturbations, SAFs exhibit robustness due to the reduction of stray fields as an effect of AFM coupling. This stability is essential for maintaining data integrity and reliability in spintronic devices. Further, SAFs are also promising for hosting chiral spin textures like skyrmions which can be free from skyrmion Hall effect (SkHE). This is essential for the straight-line motion of skyrmions in a track without deviating to the edge. Moreover, SAFs enable the manipulation of spin currents and spin waves, essential for information processing and communication in spin-based devices. The ability to engineer spin configurations in SAFs opens doors to novel functionalities, such as spin wave devices, magnetic memory logic circuits, etc., contributing significantly to the advancement of spintronics technology. Overall, SAFs are crucial in spintronics for their stability, tunability, and potential for spintronic devices, making them a focal point in research for next-generation spintronic applications. This thesis work has been focused on studying the magnetization reversal, domain structures and stabilization of chiral spin textures like skyrmion in SAF systems. Also, the spin dynamics properties have been explored for the possible presence of magnon-magnon coupling in an SAF system. For the earlier part i.e., magnetization reversal, domains and skyrmions, we have considered Co as the FM layer. Pt is used as a heavy metal

with high spin-orbit coupling to provide perpendicular magnetic anisotropy (PMA) in the Co layer. For achieving AFM interlayer exchange coupling (IEC) between the FM layers, Ru or Ir is used as a spacer layer for this study. All the samples in this study have been protected from oxidation by using Pt as a capping layer. For the later part i.e., spin dynamics study in SAF, CoFeB has been considered as the FM layer having an easy axis in the plane. Here, Ir is used as a spacer layer for having antiferromagnetic RKKY interaction between the CoFeB layers and Ta is used as a capping layer to protect the magnetic thin films from oxidation. Structural characterization of these thin films has been investigated by performing XRR measurement and TEM imaging. Further, MOKE microscopy is employed to observe the hysteresis loop as well as domain images. To evaluate the interlayer exchange coupling and anisotropy energy, SQUID-VSM measurements have been performed. Topological Hall resistivity of the skyrmionic samples has been evaluated by performing magneto-transport measurement via PPMS. Nucleation of skyrmions is observed by performing MFM imaging on our samples. Furthermore, for the spin dynamics study in the in-plane magnetized SAF, we have performed FMR measurement. All the outcomes of this thesis work have been summarized below.

Primarily, SAF samples have been prepared by considering the Pt/Co PMA system with Ru as a spacer layer. The sample structure considered for this study is Ta/Pt/Co(t_{Co})/Ru(t_{Ru})/Co(t_{Co})/Pt. The samples having Co thickness 0.8 nm show a larger antiferromagnetic coupling plateau than the samples having Co thickness 1.0 nm with a similar variation of Ru spacer layer in both the series. The strength of the interlayer exchange coupling is found to be higher for the samples with lower Co thickness. However, due to some limitations in the measurement, we could not study the behaviour of magnetic domains in this system. In further studies, Ir has been considered as a spacer layer between the FM layers. The sample structure considered here is Si/Ta(3)/$[Pt(3.5)/Co(0.8)]_m$/Ir(t_{Ir})/$[Co(0.8)/Pt(3.5)]_n$. By varying the Ir spacer thickness (t_{Ir}) as 1.0, 1.5 and 2.0 nm between the Co layers, three different types

of magnetization reversal have been observed showing FM coupling, AFM coupling i.e., SAF structure and canted state of magnetization reversal, respectively. Higher anisotropy energy as compared to the IEC energy results in a smaller intermediate angle between the magnetic moments of the two layers. The domain size is found to be smaller in the SAF samples than in the FM-coupled samples. The samples with t_{Ir}=2.0 nm with canted magnetization reversal are further investigated for the presence of chiral spin textures in this system. At the demagnetized state, a labyrinth kind of domains appeared which is observed via MFM imaging and the presence of skyrmions is seen after applying an external magnetic field to the samples. Further, we have observed a THE signal indicating the observed isolated structures to be chiral in nature. Therefore, skyrmion could be stabilized in an FM/NM/FM system with the FM layer thickness well below the spin reorientation transition by optimizing the non-magnetic spacer layer thickness. Further, we have considered Ir spacer thickness to have strong antiferromagnetic (AFM) coupling between the Co layers adjacent to the spacer. On the other hand, the effect of dipolar interaction has been increased by increasing the number of repetitions of the Pt/Co layer below and above the Ir spacer. The structure of the samples investigated in this study is $Si/SiO_2/Ta(3)/Pt(2.5)/[Pt(1)/Co(t_{Co})]_3/Ir(1.3)/[Co(t_{Co})/Pt(1)]_2/Pt(2.5)$.

The simultaneous effect of dipolar and RKKY interaction leads to a slanted type of magnetization reversal giving rise to the nucleation of high-density skyrmions observed via MFM imaging with the application of an external out-of-plane magnetic field. Further, the finite THE signal from our samples confirms observed spin textures to be chiral in nature. The average size of the skyrmions is found to be 130-160 nm. These systems can further be explored for the deterministic current-induced nucleation as well as propagation of skyrmions which can be useful for future spintronic applications.

Apart from applications of SAF for domains and skyrmions, it is also promising for spin dynamics study nowadays which can further investigate the spin waves propagation, interact,

and transfer spin information. SAF systems also show a great advantage as a host of magnon-magnon coupling. In this regard, we have prepared in-plane SAF samples with Ir spacer having structure Ta(3)/CoFeB(10)/Ir(t_{Ir})/CoFeB(7)/Ta(3). For exploring the possible presence of magnon-magnon coupling in our system, FMR measurements have been performed in the frequency sweep mode to extract the acoustic and optical magnon modes. However, due to the absence of anti-crossing gap between the acoustic and optical modes, the magnon-magnon coupling is absent in our system.

Future outlook:

In this thesis work, we have studied the domains, skyrmions and spin dynamics study in synthetic antiferromagnetic (SAF) systems which can be useful for spintronic applications. For domains and skyrmions, perpendicular magnetic anisotropic systems have been considered, whereas, for spin dynamics study, in-plane systems have been used. However, in the course of our study, we found several open questions that can be addressed in future as mentioned below.

i. Multilayers of Pt/Co PMA system with Ru spacer in the antiferromagnetic coupling regime can be investigated in detail about the domain structures as well as skyrmion static and dynamic study.
ii. Nano track devices can be made out of the Pt/Co multilayer system with Ir spacer layer where high-density skyrmions have been observed. In these devices, the current-induced skyrmion motion can be investigated which may have a reduced or negligible skyrmion Hall effect.
iii. By optimizing the properties like DMI, anisotropy, RKKY interaction, etc., in our system, the size of the skyrmions can be reduced further.
iv. The in-plane magnetized SAF systems can be tailored further to achieve robust magnon-magnon coupling for coherent information processing.

References:

[1] J. Puebla, J. Kim, K. Kondou, and Y. Otani, *Spintronic Devices for Energy-Efficient Data Storage and Energy Harvesting*, Commun Mater **1**, 1 (2020).

[2] S. Bhatti, R. Sbiaa, A. Hirohata, H. Ohno, S. Fukami, and S. N. Piramanayagam, *Spintronics Based Random Access Memory: A Review*, Materials Today **20**, 530 (2017).

[3] R. Sbiaa, H. Meng, and S. N. Piramanayagam, *Materials with Perpendicular Magnetic Anisotropy for Magnetic Random Access Memory*, Physica Status Solidi (RRL) – Rapid Research Letters **5**, 413 (2011).

[4] R. A. Duine, K.-J. Lee, S. S. P. Parkin, and M. D. Stiles, *Synthetic Antiferromagnetic Spintronics*, Nature Phys **14**, 217 (2018).

[5] V. V. Amelichev, D. V. Vasilyev, A. I. Krikunov, Yu. V. Kazakov, D. V. Kostyuk, E. P. Orlov, D. A. Zhukov, and P. A. Belyakov, *Synthetic Antiferromagnetic Structures in Technology of Spintronic Devices*, Nanotechnol Russia **16**, 155 (2021).

[6] P. Bruno and C. Chappert, *Ruderman-Kittel Theory of Oscillatory Interlayer Exchange Coupling*, Phys. Rev. B **46**, 261 (1992).

[7] P. Bruno and C. Chappert, *Oscillatory Coupling between Ferromagnetic Layers Separated by a Nonmagnetic Metal Spacer*, Phys. Rev. Lett. **67**, 1602 (1991).

[8] P. Bruno, *Theory of Interlayer Magnetic Coupling*, Phys. Rev. B **52**, 411 (1995).

[9] A. Bergman, B. Skubic, J. Hellsvik, L. Nordström, A. Delin, and O. Eriksson, *Ultrafast Switching in a Synthetic Antiferromagnetic Magnetic Random-Access Memory Device*, Phys. Rev. B **83**, 224429 (2011).

[10] T. Takenaga, T. Kuroiwa, T. Furukawa, M. Taki, K. Yoshiara, and Y. Tokuda, *Thermal Robustness in Synthetic Antiferromagnetic Free Layer for Magnetic Random Access Memory Applications*, Journal of Applied Physics **99**, 08C911 (2006).

[11] T. Nakano, M. Oogane, T. Furuichi, and Y. Ando, *Magnetic Tunnel Junctions Using Perpendicularly Magnetized Synthetic Antiferromagnetic Reference Layer for Wide-Dynamic-Range Magnetic Sensors*, Applied Physics Letters **110**, 012401 (2017).

[12] K. Yakushiji, A. Fukushima, H. Kubota, M. Konoto, and S. Yuasa, *Ultralow-Voltage Spin-Transfer Switching in Perpendicularly Magnetized Magnetic Tunnel Junctions with Synthetic Antiferromagnetic Reference Layer*, Appl. Phys. Express **6**, 113006 (2013).

[13] A. Natarajarathinam, R. Zhu, P. B. Visscher, and S. Gupta, *Perpendicular Magnetic Tunnel Junctions Based on Thin CoFeB Free Layer and Co-Based Multilayer Synthetic Antiferromagnet Pinned Layers*, Journal of Applied Physics **111**, 07C918 (2012).

[14] W. Legrand, D. Maccariello, F. Ajejas, S. Collin, A. Vecchiola, K. Bouzehouane, N. Reyren, V. Cros, and A. Fert, *Room-Temperature Stabilization of Antiferromagnetic Skyrmions in Synthetic Antiferromagnets*, Nat. Mater. **19**, 34 (2020).

[15] K. Everschor-Sitte, J. Masell, R. M. Reeve, and M. Kläui, *Perspective: Magnetic Skyrmions—Overview of Recent Progress in an Active Research Field*, Journal of Applied Physics **124**, 240901 (2018).

[16] A. Fert, N. Reyren, and V. Cros, *Magnetic Skyrmions: Advances in Physics and Potential Applications*, Nat Rev Mater **2**, 1 (2017).

[17] R. Tomasello, E. Martinez, R. Zivieri, L. Torres, M. Carpentieri, and G. Finocchio, *A Strategy for the Design of Skyrmion Racetrack Memories*, Scientific Reports **4**, 6784 (2014).

[18] X. Zhang, G. P. Zhao, H. Fangohr, J. P. Liu, W. X. Xia, J. Xia, and F. J. Morvan, *Skyrmion-Skyrmion and Skyrmion-Edge Repulsions in Skyrmion-Based Racetrack Memory*, Scientific Reports **5**, 7643 (2015).

[19] R. Tomasello, V. Puliafito, E. Martinez, A. Manchon, M. Ricci, M. Carpentieri, and G. Finocchio, *Performance of Synthetic Antiferromagnetic Racetrack Memory: Domain Wall versus Skyrmion*, J. Phys. D: Appl. Phys. **50**, 325302 (2017).

[20] W. Kang, B. Wu, X. Chen, D. Zhu, Z. Wang, X. Zhang, Y. Zhou, Y. Zhang, and W. Zhao, *A Comparative Cross-Layer Study on Racetrack Memories: Domain Wall vs Skyrmion*, J. Emerg. Technol. Comput. Syst. **16**, 2:1 (2019).

[21] K. Wang, V. Bheemarasetty, J. Duan, S. Zhou, and G. Xiao, *Fundamental Physics and Applications of Skyrmions: A Review*, Journal of Magnetism and Magnetic Materials **563**, 169905 (2022).

[22] S. Luo, M. Song, X. Li, Y. Zhang, J. Hong, X. Yang, X. Zou, N. Xu, and L. You, *Reconfigurable Skyrmion Logic Gates*, Nano Lett. **18**, 1180 (2018).

[23] K. M. Song et al., *Skyrmion-Based Artificial Synapses for Neuromorphic Computing*, Nat Electron **3**, 148 (2020).

[24] S. Luo and L. You, *Skyrmion Devices for Memory and Logic Applications*, APL Materials **9**, 050901 (2021).

[25] S. S. P. Parkin, M. Hayashi, and L. Thomas, *Magnetic Domain-Wall Racetrack Memory*, Science **320**, 190 (2008).

[26] G. Chen, *Skyrmion Hall Effect*, Nature Phys **13**, 112 (2017).

[27] W. Jiang et al., *Direct Observation of the Skyrmion Hall Effect*, Nature Phys **13**, 162 (2017).

[28] T. Dohi, S. DuttaGupta, S. Fukami, and H. Ohno, *Formation and Current-Induced Motion of Synthetic Antiferromagnetic Skyrmion Bubbles*, Nat Commun **10**, 5153 (2019).

[29] Y. Shiota, T. Taniguchi, M. Ishibashi, T. Moriyama, and T. Ono, *Tunable Magnon-Magnon Coupling Mediated by Dynamic Dipolar Interaction in Synthetic Antiferromagnets*, Phys. Rev. Lett. **125**, 017203 (2020).

[30] W. He et al., *Anisotropic Magnon–Magnon Coupling in Synthetic Antiferromagnets*, Chinese Phys. Lett. **38**, 057502 (2021).

[31] P. F. Carcia, *Perpendicular Magnetic Anisotropy in Pd/Co and Pt/Co Thin-film Layered Structures*, Journal of Applied Physics **63**, 5066 (1988).

[32] S. Blundell, *Magnetism in Condensed Matter* (OUP Oxford, 2001).

[33] M. Getzlaff, *Fundamentals of Magnetism* (Springer Science & Business Media, 2007).

[34] B. D. Cullity and C. D. Graham, *Introduction to Magnetic Materials* (John Wiley & Sons, 2011).

[35] N. B. Ekreem, A. G. Olabi, T. Prescott, A. Rafferty, and M. S. J. Hashmi, *An Overview of Magnetostriction, Its Use and Methods to Measure These Properties*, Journal of Materials Processing Technology **191**, 96 (2007).

[36] L. Nistor, *Jonctions tunnel magnétiques à aimantation perpendiculaire: anisotropie, magnétorésistance, couplages magnétiques et renversement par couple de transfert de spin* (2011).

[37] F. J. A. den Broeder, W. Hoving, and P. J. H. Bloemen, *Magnetic Anisotropy of Multilayers*, Journal of Magnetism and Magnetic Materials **93**, 562 (1991).

[38] I. Dzyaloshinsky, *A Thermodynamic Theory of "Weak" Ferromagnetism of Antiferromagnetics*, Journal of Physics and Chemistry of Solids **4**, 241 (1958).

[39] T. Moriya, *Anisotropic Superexchange Interaction and Weak Ferromagnetism*, Phys. Rev. **120**, 91 (1960).

[40] G. Finocchio and C. Panagopoulos, *Magnetic Skyrmions and Their Applications* (Woodhead Publishing, 2021).

[41] M. Johnson, *Magnetoelectronics* (Elsevier, 2004).

[42] N. A. Spaldin, *Magnetic Materials: Fundamentals and Applications* (Cambridge University Press, 2010).

[43] C. Appino, M. Valsania, and V. Basso, *A Vector Hysteresis Model Including Domain Wall Motion and Coherent Rotation*, Physica B: Condensed Matter **275**, 103 (2000).

[44] N. Chowdhury, S. Bedanta, and G. S. Babu, *Study of Magnetization Reversal Processes in a Thin Co Film*, Journal of Magnetism and Magnetic Materials **336**, 20 (2013).

[45] P. Weiss, *L'hypothèse du champ moléculaire et la propriété ferromagnétique*, J. Phys. Theor. Appl. **6**, 661 (1907).

[46] *Zur Theorie des Austauschproblems und der Remanenzerscheinung der Ferromagnetika*, (n.d.).

[47] L. Landau and E. Lifshits, *ON THE THEORY OF THE DISPERSION OF MAGNETIC PERMEABILITY IN FERROMAGNETIC BODIES*, **53**, (n.d.).

[48] L. Néel, *Some Theoretical Aspects of Rock-Magnetism*, Advances in Physics **4**, 191 (1955).

[49] D. Kumar, T. Jin, R. Sbiaa, M. Kläui, S. Bedanta, S. Fukami, D. Ravelosona, S.-H. Yang, X. Liu, and S. N. Piramanayagam, *Domain Wall Memory: Physics, Materials, and Devices*, Physics Reports **958**, 1 (2022).

[50] T. H. R. Skyrme and B. F. J. Schonland, *A Non-Linear Field Theory*, Proceedings of the Royal Society of London. Series A. Mathematical and Physical Sciences **260**, 127 (1997).

[51] A. N. Bogdanov and D. A. Yablonskii, *Thermodynamicallystable "Vortices" in Magneticallyordered Crystals.The Mixed State of Magnets*, (n.d.).

[52] S. Mühlbauer, B. Binz, F. Jonietz, C. Pfleiderer, A. Rosch, A. Neubauer, R. Georgii, and P. Böni, *Skyrmion Lattice in a Chiral Magnet*, Science **323**, 915 (2009).

[53] W. Jiang et al., *Blowing Magnetic Skyrmion Bubbles*, Science **349**, 283 (2015).

[54] N. Nagaosa and Y. Tokura, *Topological Properties and Dynamics of Magnetic Skyrmions*, Nature Nanotech **8**, 899 (2013).

[55] I. Kézsmárki et al., *Néel-Type Skyrmion Lattice with Confined Orientation in the Polar Magnetic Semiconductor GaV4S8*, Nature Mater **14**, 1116 (2015).

[56] C. Pfleiderer, *Surfaces Get Hairy*, Nature Phys **7**, 673 (2011).

[57] A. Thiaville, S. Rohart, É. Jué, V. Cros, and A. Fert, *Dynamics of Dzyaloshinskii Domain Walls in Ultrathin Magnetic Films*, EPL **100**, 57002 (2012).

[58] S. Rohart and A. Thiaville, *Skyrmion Confinement in Ultrathin Film Nanostructures in the Presence of Dzyaloshinskii-Moriya Interaction*, Phys. Rev. B **88**, 184422 (2013).

[59] W. Legrand, *Crafting Magnetic Skyrmions at Room Temperature: Size, Stability and Dynamics in Multilayers* (2019).

[60] B. Göbel, I. Mertig, and O. A. Tretiakov, *Beyond Skyrmions: Review and Perspectives of Alternative Magnetic Quasiparticles*, Physics Reports **895**, 1 (2021).

[61] G. P. Müller, M. Hoffmann, C. Dißelkamp, D. Schürhoff, S. Mavros, M. Sallermann, N. S. Kiselev, H. Jónsson, and S. Blügel, *Spirit: Multifunctional Framework for Atomistic Spin Simulations*, Phys. Rev. B **99**, 224414 (2019).

[62] C. Moreau-Luchaire et al., *Additive Interfacial Chiral Interaction in Multilayers for Stabilization of Small Individual Skyrmions at Room Temperature*, Nature Nanotech **11**, 5 (2016).

[63] O. Boulle et al., *Room-Temperature Chiral Magnetic Skyrmions in Ultrathin Magnetic Nanostructures*, Nature Nanotech **11**, 5 (2016).

[64] S. von Malottki, B. Dupé, P. F. Bessarab, A. Delin, and S. Heinze, *Enhanced Skyrmion Stability Due to Exchange Frustration*, Sci Rep **7**, 1 (2017).

[65] M. Ezawa, *Giant Skyrmions Stabilized by Dipole-Dipole Interactions in Thin Ferromagnetic Films*, Phys. Rev. Lett. **105**, 197202 (2010).

[66] S. Heinze, K. von Bergmann, M. Menzel, J. Brede, A. Kubetzka, R. Wiesendanger, G. Bihlmayer, and S. Blügel, *Spontaneous Atomic-Scale Magnetic Skyrmion Lattice in Two Dimensions*, Nature Phys **7**, 713 (2011).

[67] C. H. Marrows and K. Zeissler, *Perspective on Skyrmion Spintronics*, Applied Physics Letters **119**, 250502 (2021).

[68] W. Jiang, G. Chen, K. Liu, J. Zang, S. G. E. te Velthuis, and A. Hoffmann, *Skyrmions in Magnetic Multilayers*, Physics Reports **704**, 1 (2017).

[69] B. Ojha, S. Mallick, S. Panigrahy, M. Sharma, A. Thiaville, S. Rohart, and S. Bedanta, *Driving Skyrmions with Low Threshold Current Density in Pt/CoFeB Thin Film*, Phys. Scr. **98**, 035819 (2023).

[70] S. Mohanty, B. Ojha, M. Sharma, and S. Bedanta, *Observation of Topological Hall Effect and Skyrmions in Pt/Co/Ir/Co/Pt System*, Mater. Res. Express **11**, 046406 (2024).

[71] R. Chen et al., *Realization of Isolated and High-Density Skyrmions at Room Temperature in Uncompensated Synthetic Antiferromagnets*, Nano Letters **20**, 3299 (2020).

[72] X. Yu et al., *Current-Induced Nucleation and Annihilation of Magnetic Skyrmions at Room Temperature in a Chiral Magnet*, Advanced Materials **29**, 1606178 (2017).

[73] A. Hrabec, J. Sampaio, M. Belmeguenai, I. Gross, R. Weil, S. M. Chérif, A. Stashkevich, V. Jacques, A. Thiaville, and S. Rohart, *Current-Induced Skyrmion Generation and Dynamics in Symmetric Bilayers*, Nat Commun **8**, 15765 (2017).

[74] K. Gerlinger et al., *Application Concepts for Ultrafast Laser-Induced Skyrmion Creation and Annihilation*, Applied Physics Letters **118**, 192403 (2021).

[75] R. Juge et al., *Skyrmions in Synthetic Antiferromagnets and Their Nucleation via Electrical Current and Ultra-Fast Laser Illumination*, Nature Communications **13**, 4807 (2022).

[76] M. He et al., *Evolution of Topological Skyrmions across the Spin Reorientation Transition in Pt/Co/Ta Multilayers*, Physical Review B **97**, 174419 (2018).

[77] K. Palotás, L. Rózsa, E. Simon, L. Udvardi, and L. Szunyogh, *Spin-Polarized Scanning Tunneling Microscopy Characteristics of Skyrmionic Spin Structures Exhibiting Various Topologies*, Physical Review B **96**, 024410 (2017).

[78] R. Chen, Q. Cui, L. Han, X. Xue, J. Liang, H. Bai, Y. Zhou, F. Pan, H. Yang, and C. Song, *Controllable Generation of Antiferromagnetic Skyrmions in Synthetic Antiferromagnets with Thermal Effect*, Adv Funct Materials **32**, 2111906 (2022).

[79] M. Raju, A. Yagil, A. Soumyanarayanan, A. K. C. Tan, A. Almoalem, F. Ma, O. M. Auslaender, and C. Panagopoulos, *The Evolution of Skyrmions in Ir/Fe/Co/Pt Multilayers and Their Topological Hall Signature*, Nature Communications **10**, 696 (2019).

[80] W. S et al., *Current-Driven Dynamics and Inhibition of the Skyrmion Hall Effect of Ferrimagnetic Skyrmions in GdFeCo Films.*, Nature Communications **9**, 959 (2018).

[81] C. Moreau-Luchaire et al., *Additive Interfacial Chiral Interaction in Multilayers for Stabilization of Small Individual Skyrmions at Room Temperature*, Nature Nanotechnology **11**, 444 (2016).

[82] C. Back et al., *The 2020 Skyrmionics Roadmap*, Journal of Physics D: Applied Physics **53**, 363001 (2020).

[83] C. H. Marrows and K. Zeissler, *Perspective on Skyrmion Spintronics*, Applied Physics Letters **119**, 250502 (2021).

[84] X. Zhang, Y. Zhou, K. Mee Song, T.-E. Park, J. Xia, M. Ezawa, X. Liu, W. Zhao, G. Zhao, and S. Woo, *Skyrmion-Electronics: Writing, Deleting, Reading and Processing Magnetic Skyrmions toward Spintronic Applications*, Journal of Physics: Condensed Matter **32**, 143001 (2020).

[85] H. Zhang, Y. Zhang, Z. Hou, M. Qin, X. Gao, and J. Liu, *Magnetic Skyrmions: Materials, Manipulation, Detection, and Applications in Spintronic Devices*, Materials Futures **2**, 032201 (2023).

[86] J. Iwasaki, M. Mochizuki, and N. Nagaosa, *Current-Induced Skyrmion Dynamics in Constricted Geometries*, Nature Nanotech **8**, 742 (2013).

[87] V. T. Pham et al., *Fast Current-Induced Skyrmion Motion in Synthetic Antiferromagnets*, Science **384**, 307 (2024).

[88] S. L. Zhang, W. W. Wang, D. M. Burn, H. Peng, H. Berger, A. Bauer, C. Pfleiderer, G. van der Laan, and T. Hesjedal, *Manipulation of Skyrmion Motion by Magnetic Field Gradients*, Nat Commun **9**, 2115 (2018).

[89] A. Casiraghi, H. Corte-León, M. Vafaee, F. Garcia-Sanchez, G. Durin, M. Pasquale, G. Jakob, M. Kläui, and O. Kazakova, *Individual Skyrmion Manipulation by Local Magnetic Field Gradients*, Commun Phys **2**, 1 (2019).

[90] S. Woo et al., *Spin-Orbit Torque-Driven Skyrmion Dynamics Revealed by Time-Resolved X-Ray Microscopy*, Nat Commun **8**, 15573 (2017).

[91] S. A. Montoya, R. Tolley, I. Gilbert, S.-G. Je, M.-Y. Im, and E. E. Fullerton, *Spin-Orbit Torque Induced Dipole Skyrmion Motion at Room Temperature*, Phys. Rev. B **98**, 104432 (2018).

[92] M. Mochizuki, X. Z. Yu, S. Seki, N. Kanazawa, W. Koshibae, J. Zang, M. Mostovoy, Y. Tokura, and N. Nagaosa, *Thermally Driven Ratchet Motion of a Skyrmion Microcrystal and Topological Magnon Hall Effect*, Nature Mater **13**, 241 (2014).

[93] E. Raimondo, E. Saugar, J. Barker, D. Rodrigues, A. Giordano, M. Carpentieri, W. Jiang, O. Chubykalo-Fesenko, R. Tomasello, and G. Finocchio, *Temperature-Gradient-Driven Magnetic Skyrmion Motion*, Phys. Rev. Applied **18**, 024062 (2022).

[94] A. A. Thiele, *Applications of the Gyrocoupling Vector and Dissipation Dyadic in the Dynamics of Magnetic Domains*, Journal of Applied Physics **45**, 377 (1974).

[95] A. A. Thiele, *Steady-State Motion of Magnetic Domains*, Phys. Rev. Lett. **30**, 230 (1973).

[96] X. Zhang, Y. Zhou, and M. Ezawa, *Magnetic Bilayer-Skyrmions without Skyrmion Hall Effect*, Nature Communications **7**, 10293 (2016).

[97] L. Landau and E. Lifshits, *ON THE THEORY OF THE DISPERSION OF MAGNETIC PERMEABILITY IN FERROMAGNETIC BODIES*, **53**, (n.d.).

[98] T. L. Gilbert, *A Phenomenological Theory of Damping in Ferromagnetic Materials*, IEEE Transactions on Magnetics **40**, 3443 (2004).

[99] D. O. Yalçın, *Ferromagnetic Resonance: Theory and Applications* (BoD – Books on Demand, 2013).

[100] A. G. Gurevich and G. A. Melkov, *Magnetic Oscillations and Waves in Unsaturated Ferromagnet*, in *Magnetization Oscillations and Waves* (CRC Press, 1996).

[101] N. A. Spaldin, *Magnetic Materials: Fundamentals and Applications* (Cambridge University Press, 2010).

[102] S. Blundell, *Magnetism in Condensed Matter* (OUP Oxford, 2001).

[103] F. Bloch, *Zur Theorie des Ferromagnetismus*, Z. Physik **61**, 206 (1930).

[104] S.-K. Kim, *Micromagnetic Computer Simulations of Spin Waves in Nanometre-Scale Patterned Magnetic Elements*, J. Phys. D: Appl. Phys. **43**, 264004 (2010).

[105] M. A. Omar, *Elementary Solid State Physics: Principles and Applications* (Pearson Education India, 1999).

[106] J. E. Mahan, *Physical Vapor Deposition of Thin Films* (2000).

[107] T. M. Besmann, D. P. Stinton, and R. A. Lowden, *Chemical Vapor Deposition Techniques*, MRS Bulletin **13**, 45 (1988).

[108] D. Depla, S. Mahieu, and J. E. Greene, *Chapter 5 - Sputter Deposition Processes*, in *Handbook of Deposition Technologies for Films and Coatings (Third Edition)*, edited by P. M. Martin (William Andrew Publishing, Boston, 2010), pp. 253–296.

[109] P. J. Kelly and R. D. Arnell, *Magnetron Sputtering: A Review of Recent Developments and Applications*, Vacuum **56**, 159 (2000).

[110] J. Musil, *Recent Advances in Magnetron Sputtering Technology*, Surface and Coatings Technology **100–101**, 280 (1998).

[111] P. Sigmund, *Theory of Sputtering. I. Sputtering Yield of Amorphous and Polycrystalline Targets*, Phys. Rev. **184**, 383 (1969).

[112] M. Hughes, *What Is DC Sputtering?*, https://www.semicore.com/news/94-what-is-dc-sputtering.

[113] M. Hughes, *What Is RF Sputtering?*, https://www.semicore.com/news/92-what-is-rf-sputtering.

[114] P. D. Davidse, *Theory and Practice of RF Sputtering*, Vacuum **17**, 139 (1967).

[115] G. F. Harrington and J. Santiso, *Back-to-Basics Tutorial: X-Ray Diffraction of Thin Films*, J Electroceram **47**, 141 (2021).

[116] M. Yasaka, *X-Ray Thin-FIlm Measurement Techniques*, (2010).

[117] K. Inaba, *X-Ray Thin-FIlm Measurement Techniques*, (2008).

[118] W. H. Bragg and W. L. Bragg, *The Reflection of X-Rays by Crystals*, Proceedings of the Royal Society of London. Series A, Containing Papers of a Mathematical and Physical Character **88**, 428 (1997).

[119] *SmartLab | Rigaku Global Website*, https://www.rigaku.com/products/xrd/smartlab.

[120] Y. Fujii, *Recent Developments in the X-Ray Reflectivity Analysis for Rough Surfaces and Interfaces of Multilayered Thin Film Materials*, Journal of Materials **2013**, 1 (2013).

[121] T. P. Russell, *X-Ray and Neutron Reflectivity for the Investigation of Polymers*, Materials Science Reports **5**, 171 (1990).

[122] M. Björck and G. Andersson, *GenX: An Extensible X-Ray Reflectivity Refinement Program Utilizing Differential Evolution*, J Appl Cryst **40**, 1174 (2007).

[123] A. Glavic and M. Björck, *GenX 3: The Latest Generation of an Established Tool*, J Appl Cryst **55**, 1063 (2022).

[124] I. W. Hamley and J. S. Pedersen, *Analysis of Neutron and X-Ray Reflectivity Data. I. Theory*, Journal of Applied Crystallography **27**, 29 (1994).

[125] D. B. Williams and C. B. Carter, *The Transmission Electron Microscope*, in *Transmission Electron Microscopy: A Textbook for Materials Science*, edited by D. B. Williams and C. B. Carter (Springer US, Boston, MA, 1996), pp. 3–17.

[126] M. A. (Eric) Hayat, *Basic Techniques For Transmission Electron Microscopy* (Elsevier, 2012).

[127] A. K. Petford-Long and A. N. Chiaramonti, *Transmission Electron Microscopy of Multilayer Thin Films**, Annual Review of Materials Research **38**, 559 (2008).

[128] B. J. Inkson, *Scanning Electron Microscopy (SEM) and Transmission Electron Microscopy (TEM) for Materials Characterization*, in *Materials Characterization Using Nondestructive Evaluation (NDE) Methods* (Elsevier, 2016), pp. 17–43.

[129] J. C. Bravman and R. Sinclair, *The Preparation of Cross-Section Specimens for Transmission Electron Microscopy*, Journal of Electron Microscopy Technique **1**, 53 (1984).

[130] S. Mohanty, M. Sharma, A. K. Moharana, B. Ojha, E. Pandey, B. B. Singh, and S. Bedanta, *Magnetization Reversal and Domain Structures in Perpendicular Synthetic Antiferromagnets Prepared on Rigid and Flexible Substrates*, JOM **74**, 2319 (2022).

[131] D. A. Allwood, G. Xiong, M. D. Cooke, and R. P. Cowburn, *Magneto-Optical Kerr Effect Analysis of Magnetic Nanostructures*, J. Phys. D: Appl. Phys. **36**, 2175 (2003).

[132] J. McCord, *Progress in Magnetic Domain Observation by Advanced Magneto-Optical Microscopy*, J. Phys. D: Appl. Phys. **48**, 333001 (2015).

[133] Z. Q. Qiu and S. D. Bader, *Surface Magneto-Optic Kerr Effect*, Review of Scientific Instruments **71**, 1243 (2000).

[134] J. K. LL.D, *XLIII. On Rotation of the Plane of Polarization by Reflection from the Pole of a Magnet*, The London, Edinburgh, and Dublin Philosophical Magazine and Journal of Science (1877).

[135] J. K. LL.D, *XXIV. On Reflection of Polarized Light from the Equatorial Surface of a Magnet*, The London, Edinburgh, and Dublin Philosophical Magazine and Journal of Science (1878).

[136] R. Schäfer, *Investigation of Domains and Dynamics of Domain Walls by the Magneto-Optical Kerr-Effect*, in *Handbook of Magnetism and Advanced Magnetic Materials* (John Wiley & Sons, Ltd, 2007).

[137] T. Haider, *A Review of Magneto-Optic Effects and Its Application*, Int. J. Electromagn. Appl **7**, 17 (2017).

[138] I. V. Soldatov and R. Schäfer, *Selective Sensitivity in Kerr Microscopy*, Review of Scientific Instruments **88**, 073701 (2017).

[139] S. Foner, *Versatile and Sensitive Vibrating-Sample Magnetometer*, Review of Scientific Instruments **30**, 548 (1959).

[140] R. L. Fagaly, *Superconducting Quantum Interference Device Instruments and Applications*, Review of Scientific Instruments **77**, 101101 (2006).

[141] *Quantum Design India - Products - SQUID Magnetometer – Quantum Design MPMS®3*, https://www.qd-india.com/products/mpms3.html.

[142] P. Grütter, H. J. Mamin, and D. Rugar, *Magnetic Force Microscopy (MFM)*, in *Scanning Tunneling Microscopy II: Further Applications and Related Scanning Techniques*, edited by R. Wiesendanger and H.-J. Güntherodt (Springer, Berlin, Heidelberg, 1992), pp. 151–207.

[143] H. J. Hug et al., *Quantitative Magnetic Force Microscopy on Perpendicularly Magnetized Samples*, Journal of Applied Physics **83**, 5609 (1998).

[144] H. H.-T. Corporation, *Magnetic Force Microscope (MFM)*, https://www.hitachi-hightech.com/global/en/knowledge/microscopes/spm-afm/descriptions/mfm.html.

[145] M. R. Koblischka and U. Hartmann, *Recent Advances in Magnetic Force Microscopy*, Ultramicroscopy **97**, 103 (2003).

[146] D. W. F. James and R. G. Jones, *On the Four-Probe Method of Resistivity Measurement*, J. Sci. Instrum. **42**, 283 (1965).

[147] A. A. Ramadan, R. D. Gould, and A. Ashour, *On the Van Der Pauw Method of Resistivity Measurements*, Thin Solid Films **239**, 272 (1994).

[148] P. M. Hemenger, *Measurement of High Resistivity Semiconductors Using the van Der Pauw Method*, Review of Scientific Instruments **44**, 698 (1973).

[149] J. H. Scofield, *Ac Method for Measuring Low-frequency Resistance Fluctuation Spectra*, Review of Scientific Instruments **58**, 985 (1987).

[150] I. S. Maksymov and M. Kostylev, *Broadband Stripline Ferromagnetic Resonance Spectroscopy of Ferromagnetic Films, Multilayers and Nanostructures*, Physica E: Low-Dimensional Systems and Nanostructures **69**, 253 (2015).

[151] G. Woltersdorf, *SPIN-PUMPING AND TWO-MAGNON SCATTERING IN MAGNETIC MULTILAYERS*, (n.d.).

[152] S. Bandiera, R. C. Sousa, Y. Dahmane, C. Ducruet, C. Portemont, V. Baltz, S. Auffret, I. L. Prejbeanu, and B. Dieny, *Comparison of Synthetic Antiferromagnets and Hard Ferromagnets as Reference Layer in Magnetic Tunnel Junctions With Perpendicular Magnetic Anisotropy*, IEEE Magnetics Letters **1**, 3000204 (2010).

[153] R. A. Duine, K.-J. Lee, S. S. P. Parkin, and M. D. Stiles, *Synthetic Antiferromagnetic Spintronics*, Nature Physics **14**, 217 (2018).

[154] S. S. P. Parkin, N. More, and K. P. Roche, *Oscillations in Exchange Coupling and Magnetoresistance in Metallic Superlattice Structures: Co/Ru, Co/Cr, and Fe/Cr*, Physical Review Letters **64**, 2304 (1990).

[155] S. S. P. Parkin, *Systematic Variation of the Strength and Oscillation Period of Indirect Magnetic Exchange Coupling through the 3d, 4d, and 5d Transition Metals*, Physical Review Letters **67**, 3598 (1991).

[156] M. D. Stiles, *Exchange Coupling in Magnetic Heterostructures*, Physical Review B **48**, 7238 (1993).

[157] M. D. Stiles, *Interlayer Exchange Coupling*, Journal of Magnetism and Magnetic Materials **200**, 322 (1999).

[158] P. Bruno and C. Chappert, *Oscillatory Coupling between Ferromagnetic Layers Separated by a Nonmagnetic Metal Spacer*, Physical Review Letters **67**, 1602 (1991).

[159] P. Bruno and C. Chappert, *Ruderman-Kittel Theory of Oscillatory Interlayer Exchange Coupling*, Physical Review B **46**, 261 (1992).

[160] P. Bruno, *Theory of Interlayer Magnetic Coupling*, Physical Review B **52**, 411 (1995).

[161] K. Wang, V. Bheemarasetty, and G. Xiao, *Spin Textures in Synthetic Antiferromagnets: Challenges, Opportunities, and Future Directions*, APL Materials **11**, 070902 (2023).

[162] S. Ikeda, K. Miura, H. Yamamoto, K. Mizunuma, H. D. Gan, M. Endo, S. Kanai, J. Hayakawa, F. Matsukura, and H. Ohno, *A Perpendicular-Anisotropy CoFeB–MgO Magnetic Tunnel Junction*, Nature Mater **9**, 721 (2010).

[163] S. Ikeda, J. Hayakawa, Y. M. Lee, F. Matsukura, Y. Ohno, T. Hanyu, and H. Ohno, *Magnetic Tunnel Junctions for Spintronic Memories and Beyond*, IEEE Transactions on Electron Devices **54**, 991 (2007).

[164] L. C. Sampaio, M. P. de Albuquerque, and F. S. de Menezes, *Magnetic Relaxation and Formation of Magnetic Domains in Ultrathin Films with Perpendicular Anisotropy*, Phys. Rev. B **54**, 6465 (1996).

[165] K.-S. Lee, S.-W. Lee, B.-C. Min, and K.-J. Lee, *Thermally Activated Switching of Perpendicular Magnet by Spin-Orbit Spin Torque*, Applied Physics Letters **104**, 072413 (2014).

[166] C.-L. Yang and C.-H. Lai, *High Thermal Durability of Ru-Based Synthetic Antiferromagnet by Interfacial Engineering with Re Insertion*, Sci Rep **11**, 15214 (2021).

[167] K. Yakushiji, H. Kubota, A. Fukushima, and S. Yuasa, *Perpendicular Magnetic Tunnel Junctions with Strong Antiferromagnetic Interlayer Exchange Coupling at First Oscillation Peak*, Applied Physics Express **8**, 083003 (2015).

[168] J.-H. Park, C. Park, T. Jeong, M. T. Moneck, N. T. Nufer, and J.-G. Zhu, *Co/Pt Multilayer Based Magnetic Tunnel Junctions Using Perpendicular Magnetic Anisotropy*, Journal of Applied Physics **103**, 07A917 (2008).

[169] Z. R. Tadisina, A. Natarajarathinam, and S. Gupta, *Magnetic Tunnel Junctions with Co-Based Perpendicular Magnetic Anisotropy Multilayers*, J. Vac. Sci. Technol. A **28**, 973 (2010).

[170] M. Wang, Y. Zhang, X. Zhao, and W. Zhao, *Tunnel Junction with Perpendicular Magnetic Anisotropy: Status and Challenges*, Micromachines **6**, 8 (2015).

[171] J. Chatterjee, S. Auffret, R. Sousa, P. Coelho, I.-L. Prejbeanu, and B. Dieny, *Novel Multifunctional RKKY Coupling Layer for Ultrathin Perpendicular Synthetic Antiferromagnet*, Sci Rep **8**, 11724 (2018).

[172] G. Chen, *Skyrmion Hall Effect*, Nature Physics **13**, 112 (2017).

[173] T. Dohi, S. DuttaGupta, S. Fukami, and H. Ohno, *Formation and Current-Induced Motion of Synthetic Antiferromagnetic Skyrmion Bubbles*, Nature Communications **10**, 5153 (2019).

[174] S. Zhou, C. Wang, C. Zheng, and Y. Liu, *Manipulating Skyrmions in Synthetic Antiferromagnetic Nanowires by Magnetic Field Gradients*, Journal of Magnetism and Magnetic Materials **493**, 165740 (2020).

[175] J. L. Leal and M. H. Kryder, *Spin Valves Exchange Biased by Co/Ru/Co Synthetic Antiferromagnets*, Journal of Applied Physics **83**, 3720 (1998).

[176] T. Nakano, M. Oogane, T. Furuichi, and Y. Ando, *Magnetic Tunnel Junctions Using Perpendicularly Magnetized Synthetic Antiferromagnetic Reference Layer for Wide-Dynamic-Range Magnetic Sensors*, Applied Physics Letters **110**, 012401 (2017).

[177] T. Nakano, M. Oogane, and Y. Ando, *Annealing Effect on Interlayer Exchange Coupling in Perpendicularly Magnetized Synthetic Antiferromagnetic Structure Based on Co/Pd Multilayers with Ultrathin Ru Spacer*, Jpn. J. Appl. Phys. **57**, 073001 (2018).

[178] Q. Yang et al., *Ionic Liquid Gating Control of RKKY Interaction in FeCoB/Ru/FeCoB and (Pt/Co)2/Ru/(Co/Pt)2 Multilayers*, Nat Commun **9**, 991 (2018).

[179] M. S. Gabor, T. Petrisor, R. B. Mos, M. Nasui, C. Tiusan, and T. Petrisor, *Interlayer Exchange Coupling in Perpendicularly Magnetized Pt/Co/Ir/Co/Pt Structures*, Journal of Physics D: Applied Physics **50**, 465004 (2017).

[180] Z. Zhang, L. Zhou, P. E. Wigen, and K. Ounadjela, *Angular Dependence of Ferromagnetic Resonance in Exchange-Coupled Co/Ru/Co Trilayer Structures*, Phys. Rev. B **50**, 6094 (1994).

[181] I. Dzyaloshinsky, *A Thermodynamic Theory of "Weak" Ferromagnetism of Antiferromagnetics*, Journal of Physics and Chemistry of Solids **4**, 241 (1958).

[182] T. Moriya, *Anisotropic Superexchange Interaction and Weak Ferromagnetism*, Physical Review **120**, 91 (1960).

[183] K. Yakushiji, A. Sugihara, A. Fukushima, H. Kubota, and S. Yuasa, *Very Strong Antiferromagnetic Interlayer Exchange Coupling with Iridium Spacer Layer for Perpendicular Magnetic Tunnel Junctions*, Applied Physics Letters **110**, 092406 (2017).

[184] A. Fukushima, T. Taniguchi, A. Sugihara, K. Yakushiji, H. Kubota, and S. Yuasa, *Giant Magnetoresistance in Perpendicularly Magnetized Synthetic Antiferromagnetic Coupling with Ir Spacer*, AIP Advances **8**, 055925 (2018).

[185] M. Caseiro, R. Macedo, P. D. R. Araujo, S. Cardoso, M. Erkovan, and P. P. Freitas, *Temperature Stability of Co/Pt and Co/Pd Synthetic Antiferromagnets Using an Ir Spacer*, J Mater Sci: Mater Electron **34**, 1671 (2023).

[186] R. Takashima, T. Tsukagoshi, T. Ishihara, and T. Kai, *Ab Initio Calculation of Interlayer Exchange Coupling in Co-Based Synthetic Antiferromagnet with Alloy Spacer*, AIP Advances **10**, 015324 (2020).

[187] Y. Liu, J. Yu, and H. Zhong, *Strong Antiferromagnetic Interlayer Exchange Coupling in [Co/Pt]6/Ru/[Co/Pt]4 Structures with Perpendicular Magnetic Anisotropy*, Journal of Magnetism and Magnetic Materials **473**, 381 (2019).

[188] J. Yun et al., *Tuning the Spin-Flop Transition in Perpendicularly Magnetized Synthetic Antiferromagnets by Swift Heavy Fe Ions Irradiation*, Phys. Rev. B **104**, 134416 (2021).

[189] A. Talantsev, Y. Lu, T. Fache, M. Lavanant, A. Hamadeh, A. Aristov, O. Koplak, R. Morgunov, and S. Mangin, *Relaxation Dynamics of Magnetization Transitions in Synthetic Antiferromagnet with Perpendicular Anisotropy*, J. Phys.: Condens. Matter **30**, 135804 (2018).

[190] Y. Fu, S. Ishio, T. Wang, W. Pei, T. Hasegawa, H. Yamane, and H. Saito, *Tuning Interlayer Coupling and Domain Structure in [Co/Pd]nCo/Ru[Co/Pd(x)]m Multilayer by Controlling the Thickness x of the Weak-Ferromagnetic Pd Layers in the Lower Co/Pd Multilayer*, Journal of Applied Physics **105**, 07C307 (2009).

[191] A. N. Bogdanov and D. A. Yablonskii, *Thermodynamicallystable "Vortices" in Magneticallyordered Crystals.The Mixed State of Magnets*, (n.d.).

[192] A. Bogdanov and A. Hubert, *Thermodynamically Stable Magnetic Vortex States in Magnetic Crystals*, Journal of Magnetism and Magnetic Materials **138**, 255 (1994).

[193] A. N. Bogdanov and C. Panagopoulos, *Physical Foundations and Basic Properties of Magnetic Skyrmions*, Nature Reviews Physics **2**, 492 (2020).

[194] S. Mühlbauer, B. Binz, F. Jonietz, C. Pfleiderer, A. Rosch, A. Neubauer, R. Georgii, and P. Böni, *Skyrmion Lattice in a Chiral Magnet*, Science **323**, 915 (2009).

[195] A. O. Leonov, T. L. Monchesky, N. Romming, A. Kubetzka, A. N. Bogdanov, and R. Wiesendanger, *The Properties of Isolated Chiral Skyrmions in Thin Magnetic Films*, New Journal of Physics **18**, 065003 (2016).

[196] S. Luo, M. Song, X. Li, Y. Zhang, J. Hong, X. Yang, X. Zou, N. Xu, and L. You, *Reconfigurable Skyrmion Logic Gates*, Nano Letters **18**, 1180 (2018).

[197] A. Dash, B. Ojha, S. Mohanty, A. K. Moharana, and S. Bedanta, *Device Geometry Dependent Deterministic Skyrmion Generation from a Skyrmionium*, Nanotechnology **34**, 185001 (2023).

[198] X. Zhang, M. Ezawa, and Y. Zhou, *Magnetic Skyrmion Logic Gates: Conversion, Duplication and Merging of Skyrmions*, Scientific Reports **5**, 9400 (2015).

[199] O. Boulle et al., *Room-Temperature Chiral Magnetic Skyrmions in Ultrathin Magnetic Nanostructures*, Nature Nanotechnology **11**, 449 (2016).

[200] S. Rohart and A. Thiaville, *Skyrmion Confinement in Ultrathin Film Nanostructures in the Presence of Dzyaloshinskii-Moriya Interaction*, Physical Review B **88**, 184422 (2013).

[201] S. von Malottki, B. Dupé, P. F. Bessarab, A. Delin, and S. Heinze, *Enhanced Skyrmion Stability Due to Exchange Frustration*, Scientific Reports **7**, 12299 (2017).

[202] M. Ezawa, *Giant Skyrmions Stabilized by Dipole-Dipole Interactions in Thin Ferromagnetic Films*, Physical Review Letters **105**, 197202 (2010).

[203] A. Fert, V. Cros, and J. Sampaio, *Skyrmions on the Track*, Nature Nanotechnology **8**, 152 (2013).

[204] A. Fert, N. Reyren, and V. Cros, *Magnetic Skyrmions: Advances in Physics and Potential Applications*, Nature Reviews Materials **2**, 1 (2017).

[205] N. Nagaosa and Y. Tokura, *Topological Properties and Dynamics of Magnetic Skyrmions*, Nature Nanotechnology **8**, 899 (2013).

[206] J. Sampaio, V. Cros, S. Rohart, A. Thiaville, and A. Fert, *Nucleation, Stability and Current-Induced Motion of Isolated Magnetic Skyrmions in Nanostructures*, Nature Nanotechnology **8**, 839 (2013).

[207] B. Ojha, S. Mallick, S. Panigrahy, M. Sharma, A. Thiaville, S. Rohart, and S. Bedanta, *Driving Skyrmions with Low Threshold Current Density in Pt/CoFeB Thin Film*, Physica Scripta **98**, 035819 (2023).

[208] R. Chen, Q. Cui, L. Han, X. Xue, J. Liang, H. Bai, Y. Zhou, F. Pan, H. Yang, and C. Song, *Controllable Generation of Antiferromagnetic Skyrmions in Synthetic Antiferromagnets with Thermal Effect*, Advanced Functional Materials **32**, 2111906 (2022).

[209] W. Legrand, D. Maccariello, F. Ajejas, S. Collin, A. Vecchiola, K. Bouzehouane, N. Reyren, V. Cros, and A. Fert, *Room-Temperature Stabilization of Antiferromagnetic Skyrmions in Synthetic Antiferromagnets*, Nature Materials **19**, 34 (2020).

[210] S. Brinker, M. dos Santos Dias, and S. Lounis, *Prospecting Chiral Multisite Interactions in Prototypical Magnetic Systems*, Phys. Rev. Res. **2**, 033240 (2020).

[211] T. Okubo, S. Chung, and H. Kawamura, *Multiple-q States and the Skyrmion Lattice of the Triangular-Lattice Heisenberg Antiferromagnet under Magnetic Fields*, Phys. Rev. Lett. **108**, 017206 (2012).

[212] M. Mohylna, F. A. Gómez Albarracín, M. Žukovič, and H. D. Rosales, *Spontaneous Antiferromagnetic Skyrmion/Antiskyrmion Lattice and Spiral Spin-Liquid States in the Frustrated Triangular Lattice*, Phys. Rev. B **106**, 224406 (2022).

[213] D. Amoroso, P. Barone, and S. Picozzi, *Spontaneous Skyrmionic Lattice from Anisotropic Symmetric Exchange in a Ni-Halide Monolayer*, Nat Commun **11**, 5784 (2020).

[214] S. Hayami and Y. Motome, *N\'eel- and Bloch-Type Magnetic Vortices in Rashba Metals*, Phys. Rev. Lett. **121**, 137202 (2018).

[215] S. Gao et al., *Fractional Antiferromagnetic Skyrmion Lattice Induced by Anisotropic Couplings*, Nature **586**, 37 (2020).

[216] R. Salikhov, F. Samad, S. S. P. K. Arekapudi, R. Ehrler, J. Lindner, N. S. Kiselev, and O. Hellwig, *Control and Tunability of Magnetic Bubble States in Multilayers with Strong Perpendicular Magnetic Anisotropy at Ambient Conditions*, Phys. Rev. B **106**, 054404 (2022).

[217] M. Raju et al., *Colossal Topological Hall Effect at the Transition between Isolated and Lattice-Phase Interfacial Skyrmions*, Nature Communications **12**, 2758 (2021).

[218] T. Nakajima, H. Oike, A. Kikkawa, E. P. Gilbert, N. Booth, K. Kakurai, Y. Taguchi, Y. Tokura, F. Kagawa, and T. Arima, *Skyrmion Lattice Structural Transition in MnSi*, Science Advances **3**, e1602562 (2017).

[219] H. D. Rosales, F. A. G. Albarracín, P. Pujol, and L. D. C. Jaubert, *Skyrmion Fluid and Bimeron Glass Protected by a Chiral Spin Liquid on a Kagome Lattice*, Phys. Rev. Lett. **130**, 106703 (2023).

[220] F. A. Gómez Albarracín, H. D. Rosales, M. Udagawa, P. Pujol, and L. D. C. Jaubert, *From Chiral Spin Liquids to Skyrmion Fluids and Crystals, and Their Interplay with Itinerant Electrons*, Phys. Rev. B **109**, 064426 (2024).

[221] A. Soumyanarayanan et al., *Tunable Room-Temperature Magnetic Skyrmions in Ir/Fe/Co/Pt Multilayers*, Nature Materials **16**, 898 (2017).

[222] R. Y. Chen, R. Q. Zhang, Y. J. Zhou, H. Bai, F. Pan, and C. Song, *Magnetic Field Direction Dependence of Topological Hall Effect like Features in Synthetic Ferromagnetic and Antiferromagnetic Multilayers*, Applied Physics Letters **116**, 242403 (2020).

[223] P. K. Sivakumar et al., *Topological Hall Signatures of Two Chiral Spin Textures Hosted in a Single Tetragonal Inverse Heusler Thin Film*, ACS Nano **14**, 13463 (2020).

[224] G. Kimbell, C. Kim, W. Wu, M. Cuoco, and J. W. A. Robinson, *Challenges in Identifying Chiral Spin Textures via the Topological Hall Effect*, Communications Materials **3**, 19 (2022).

[225] P. Swekis, A. Markou, D. Kriegner, J. Gayles, R. Schlitz, W. Schnelle, S. T. B. Goennenwein, and C. Felser, *Topological Hall Effect in Thin Films of Mn 1.5 PtSn*, Physical Review Materials **3**, 013001 (2019).

[226] L. Tai et al., *Distinguishing the Two-Component Anomalous Hall Effect from the Topological Hall Effect*, ACS Nano **16**, 17336 (2022).

[227] K. Wang, V. Bheemarasetty, J. Duan, S. Zhou, and G. Xiao, *Fundamental Physics and Applications of Skyrmions: A Review*, Journal of Magnetism and Magnetic Materials **563**, 169905 (2022).

[228] F. Jonietz et al., *Spin Transfer Torques in MnSi at Ultralow Current Densities*, Science **330**, 1648 (2010).

[229] T. Schulz, R. Ritz, A. Bauer, M. Halder, M. Wagner, C. Franz, C. Pfleiderer, K. Everschor, M. Garst, and A. Rosch, *Emergent Electrodynamics of Skyrmions in a Chiral Magnet*, Nature Phys **8**, 301 (2012).

[230] J. Iwasaki, M. Mochizuki, and N. Nagaosa, *Universal Current-Velocity Relation of Skyrmion Motion in Chiral Magnets*, Nat Commun **4**, 1463 (2013).

[231] M. He et al., *Realization of Zero-Field Skyrmions with High-Density via Electromagnetic Manipulation in Pt/Co/Ta Multilayers*, Applied Physics Letters **111**, 202403 (2017).

[232] T. Lin et al., *Observation of Room-Temperature Magnetic Skyrmions in Pt/Co/W Structures with a Large Spin-Orbit Coupling*, Phys. Rev. B **98**, 174425 (2018).

[233] S. Cheng et al., *Room-Temperature Magnetic Skyrmions in Pt/Co/Cu Multilayers*, Phys. Rev. B **108**, 174433 (2023).

[234] S. Woo et al., *Observation of Room-Temperature Magnetic Skyrmions and Their Current-Driven Dynamics in Ultrathin Metallic Ferromagnets*, Nature Mater **15**, 501 (2016).

[235] I. Lemesh and G. S. D. Beach, *Twisted Domain Walls and Skyrmions in Perpendicularly Magnetized Multilayers*, Phys. Rev. B **98**, 104402 (2018).

[236] M. Hervé, B. Dupé, R. Lopes, M. Böttcher, M. D. Martins, T. Balashov, L. Gerhard, J. Sinova, and W. Wulfhekel, *Stabilizing Spin Spirals and Isolated Skyrmions at Low Magnetic Field Exploiting Vanishing Magnetic Anisotropy*, Nat Commun **9**, 1015 (2018).

[237] W. Jiang et al., *Blowing Magnetic Skyrmion Bubbles*, Science **349**, 283 (2015).

[238] R. Tolley, S. A. Montoya, and E. E. Fullerton, *Room-Temperature Observation and Current Control of Skyrmions in Pt/Co/Os/Pt Thin Films*, Phys. Rev. Materials **2**, 044404 (2018).

[239] N. Nagaosa, J. Sinova, S. Onoda, A. H. MacDonald, and N. P. Ong, *Anomalous Hall Effect*, Rev. Mod. Phys. **82**, 1539 (2010).

[240] A. Neubauer, C. Pfleiderer, B. Binz, A. Rosch, R. Ritz, P. G. Niklowitz, and P. Böni, *Topological Hall Effect in the A Phase of MnSi*, Phys. Rev. Lett. **102**, 186602 (2009).

[241] N. Kanazawa, Y. Onose, T. Arima, D. Okuyama, K. Ohoyama, S. Wakimoto, K. Kakurai, S. Ishiwata, and Y. Tokura, *Large Topological Hall Effect in a Short-Period Helimagnet MnGe*, Physical Review Letters **106**, 156603 (2011).

[242] Y. Li, N. Kanazawa, X. Z. Yu, A. Tsukazaki, M. Kawasaki, M. Ichikawa, X. F. Jin, F. Kagawa, and Y. Tokura, *Robust Formation of Skyrmions and Topological Hall Effect Anomaly in Epitaxial Thin Films of MnSi*, Physical Review Letters **110**, 117202 (2013).

[243] A. Mourkas, A. Markou, P. Swekis, and I. Panagiotopoulos, *Topological Hall Effect in Pt/Co/W Multilayers with Different Anisotropies*, Journal of Magnetism and Magnetic Materials **530**, 167937 (2021).

[244] D. Maccariello, W. Legrand, N. Reyren, K. Garcia, K. Bouzehouane, S. Collin, V. Cros, and A. Fert, *Electrical Detection of Single Magnetic Skyrmions in Metallic Multilayers at Room Temperature*, Nature Nanotech **13**, 233 (2018).

[245] J. Faure-Vincent, C. Tiusan, C. Bellouard, E. Popova, M. Hehn, F. Montaigne, and A. Schuhl, *Interlayer Magnetic Coupling Interactions of Two Ferromagnetic Layers by Spin Polarized Tunneling*, Physical Review Letters **89**, 107206 (2002).

[246] Y.-J. Chang, A. Canizo-Cabrera, V. Garcia-Vazquez, Y.-H. Chang, and T. Wu, *Perpendicular Magnetic Tunnel Junctions with Synthetic Antiferromagnetic Pinned Layers Based on [Co/Pd] Multilayers*, Journal of Applied Physics **113**, 17B909 (2013).

[247] L. Cuchet, B. Rodmacq, S. Auffret, R. C. Sousa, I. L. Prejbeanu, and B. Dieny, *Perpendicular Magnetic Tunnel Junctions with a Synthetic Storage or Reference Layer: A New Route towards Pt- and Pd-Free Junctions*, Sci Rep **6**, 21246 (2016).

[248] A. V. Chumak, A. A. Serga, and B. Hillebrands, *Magnon Transistor for All-Magnon Data Processing*, Nat Commun **5**, 4700 (2014).

[249] A. Khitun, M. Bao, and K. L. Wang, *Magnonic Logic Circuits*, J. Phys. D: Appl. Phys. **43**, 264005 (2010).

[250] Y. Li et al., *Coherent Spin Pumping in a Strongly Coupled Magnon-Magnon Hybrid System*, Phys. Rev. Lett. **124**, 117202 (2020).

[251] D. Lachance-Quirion, S. P. Wolski, Y. Tabuchi, S. Kono, K. Usami, and Y. Nakamura, *Entanglement-Based Single-Shot Detection of a Single Magnon with a Superconducting Qubit*, Science **367**, 425 (2020).

[252] A. V. Chumak, V. I. Vasyuchka, A. A. Serga, and B. Hillebrands, *Magnon Spintronics*, Nature Physics **11**, 453 (2015).

[253] B. A. Kalinikos and A. N. Slavin, *Theory of Dipole-Exchange Spin Wave Spectrum for Ferromagnetic Films with Mixed Exchange Boundary Conditions*, J. Phys. C: Solid State Phys. **19**, 7013 (1986).

[254] P. Grünberg, *Light Scattering from Spin Waves in Thin Films and Layered Magnetic Structures*, in *Light Scattering in Solids V: Superlattices and Other Microstructures*, edited by M. Cardona and G. Güntherodt (Springer, Berlin, Heidelberg, 1989), pp. 303–335.

[255] L. Liensberger, A. Kamra, H. Maier-Flaig, S. Geprägs, A. Erb, S. T. B. Goennenwein, R. Gross, W. Belzig, H. Huebl, and M. Weiler, *Exchange-Enhanced Ultrastrong Magnon-Magnon Coupling in a Compensated Ferrimagnet*, Phys. Rev. Lett. **123**, 117204 (2019).

[256] D. MacNeill, J. T. Hou, D. R. Klein, P. Zhang, P. Jarillo-Herrero, and L. Liu, *Gigahertz Frequency Antiferromagnetic Resonance and Strong Magnon-Magnon Coupling in the Layered Crystal ${\mathrm{CrCl}}_{3}$*, Phys. Rev. Lett. **123**, 047204 (2019).

[257] J. Chen, C. Liu, T. Liu, Y. Xiao, K. Xia, G. E. W. Bauer, M. Wu, and H. Yu, *Strong Interlayer Magnon-Magnon Coupling in Magnetic Metal-Insulator Hybrid Nanostructures*, Phys. Rev. Lett. **120**, 217202 (2018).

[258] S. Klingler et al., *Spin-Torque Excitation of Perpendicular Standing Spin Waves in Coupled YIG/Co Heterostructures*, Phys. Rev. Lett. **120**, 127201 (2018).

[259] C. Dai and F. Ma, *Strong Magnon–Magnon Coupling in Synthetic Antiferromagnets*, Applied Physics Letters **118**, 112405 (2021).

[260] Y. Shiota, T. Taniguchi, M. Ishibashi, T. Moriyama, and T. Ono, *Tunable Magnon-Magnon Coupling Mediated by Dynamic Dipolar Interaction in Synthetic Antiferromagnets*, Physical Review Letters **125**, 017203 (2020).

[261] W. He et al., *Anisotropic Magnon–Magnon Coupling in Synthetic Antiferromagnets*, Chinese Physics Letters **38**, 057502 (2021).

[262] M. Li, J. Lu, and W. He, *Symmetry Breaking Induced Magnon-Magnon Coupling in Synthetic Antiferromagnets*, Physical Review B **103**, 064429 (2021).

[263] C. Kittel, *On the Theory of Ferromagnetic Resonance Absorption*, Phys. Rev. **73**, 155 (1948).

[264] A. Sud, C. W. Zollitsch, A. Kamimaki, T. Dion, S. Khan, S. Iihama, S. Mizukami, and H. Kurebayashi, *Tunable Magnon-Magnon Coupling in Synthetic Antiferromagnets*, Physical Review B **102**, 100403 (2020).

[265] Y. Wang et al., *Ultrastrong to Nearly Deep-Strong Magnon-Magnon Coupling with a High Degree of Freedom in Synthetic Antiferromagnets - Nature Communications*, Nature Communications **15**, 2077 (2024).

[266] X. Chen, C. Zheng, S. Zhou, Y. Liu, and Z. Zhang, *Manipulation of Time- and Frequency-Domain Dynamics by Magnon-Magnon Coupling in Synthetic Antiferromagnets*, Magnetochemistry **8**, 7 (2021).

[267] B. Hu and W. He, *Tunable Magnon-Magnon Coupling Mediated by in-Plane Magnetic Anisotropy in Synthetic Antiferromagnets*, Journal of Magnetism and Magnetic Materials **565**, 170283 (2023).